Towards In Vivo MRI Axon Radius Mapping: Insights from MRI-Scale Histology and Experimental Validation

Vom Promotionsausschuss der
Technischen Universität Hamburg
zur Erlangung des akademischen Grades

Doktor der Naturwissenschaften (Dr. rer. nat.)

genehmigte Dissertation (Monografie)

von
Laurin Mordhorst

aus
Kiel

2026

Vorsitzender des Prüfungsausschusses:
Prof. Dr.-Ing. Gerhard Bauch

Gutachter:
Prof. Dr. rer. nat. Marko Lindner
Prof. Dr. rer. medic. Siawoosh Natho-Mohammadi
Dr. sc. Jelle Veraart

Tag der mündlichen Prüfung:
19. Dezember 2025

Creative Commons Lizenzvertrag:
Der Text steht, soweit nicht anders gekennzeichnet, unter der Creative-Commons-Lizenz Namensnennung 4.0 (CC BY 4.0). Das bedeutet, dass er vervielfältigt, verbreitet und öffentlich zugänglich gemacht werden darf, auch kommerziell, sofern dabei stets der Urheber, die Quelle des Textes und o. g. Lizenz genannt werden. Die genaue Formulierung der Lizenz kann unter https://creativecommons.org/licenses/by/4.0/legalcode.de aufgerufen werden.

DOI:
https://doi.org/10.15480/882.16420

ORCID von Laurin Mordhorst:
https://orcid.org/0000-0001-9870-3916

Summary

Axons are micrometer-thin cables that carry signals across the brain, with their size determining how quickly those signals travel. Because axon size can be altered in neurological disorders such as autism spectrum disorder and Alzheimer's disease, it represents a promising clinical biomarker candidate.

Diffusion-weighted magnetic resonance imaging (MRI) provides a non-invasive way of probing axon size in vivo via the effective axon radius r_{eff}, a scalar approximation of all axon radii within an MRI voxel. However, r_{eff} appears to be measurable only on specialized research scanners and lacks quantitative experimental validation, as available histology is sparse and restricted mainly to qualitative assessments, especially in humans.

This thesis addresses these challenges through three steps: (i) creating a densely sampled, MRI-scale histological reference for r_{eff} in the human corpus callosum using deep learning-based segmentation of light microscopy, (ii) validating state-of-the-art in vivo and ex vivo MRI r_{eff} estimation methods against this histological reference, and (iii) using histology-informed simulations to explore clinical feasibility and identify limitations of the current approach.

We first establish our histological reference for r_{eff}, showing improved precision and accuracy compared to existing histology. Using this reference, we demonstrate a significant correlation with in vivo MRI-based r_{eff}, providing the first quantitative evidence that MRI captures anatomical variation of axon size in the human brain. While these results were obtained on a research scanner, simulations suggest that translation to recent clinical scanners may be feasible, albeit requiring substantial gains in signal-to-noise ratio. At the same time, our simulations reveal an inherent sensitivity limitation of the current signal model, preventing experimental validation of r_{eff} under ex vivo conditions.

In conclusion, this thesis establishes a histological framework for validating r_{eff} and provides the first quantitative evidence that MRI can measure axon radii in the human brain. It also highlights the steps required for clinical adoption and identifies key modeling limitations that point the way toward future advances.

Acknowledgments

I would like to express my sincere gratitude to all those who supported and accompanied me during the course of this doctoral work.

First and foremost, I thank my supervisor Siawoosh Natho-Mohammadi for his continuous support, trust, and guidance throughout this project.

I also thank my examiners Marko Lindner and Jelle Veraart for their time, interest in my work, and for serving on my examination committee.

My sincere thanks go to my colleagues in the group — Francisco, Malte, Nina, Tobias, Behnam, Jan, Laura, and Antonia — for many fruitful discussions, their willingness to share expertise, and for creating a supportive and stimulating working environment.

I am also grateful to the running group at work — Francisco, Julia, Mana, Marie, and Ying — for providing a welcome balance to academic life and for many motivating and enjoyable moments outside the office.

Finally, I thank my office mates Alena, Ivana, and Lynn for their companionship, support, and the many everyday conversations that made the working days more pleasant.

Contents

Chapter 1

General introduction

Axons can be thought of as micrometer-thin cables that transmit signals across the brain, with their size influencing signal transmission speed [1–3]. Axon size varies spatially across the brain [4–6] and changes temporally throughout development and aging, making axon size a key feature of brain structure and function. Importantly, axon size can also change during damage or disease, such as in a range of neurological disorders, including neurodevelopmental conditions such as autism spectrum disorder (ASD) [7, 8] and neurodegenerative diseases such as multiple sclerosis [9], Alzheimer's disease [10] and Parkinson's disease [11]. Together, these observations position the axon radius as a potential neuroimaging biomarker for clinical application.

This biomarker may be accessible through diffusion-weighted magnetic resonance imaging (dMRI). Most dMRI signal models for axon radius represent axons as cylindrical structures with varying radii [12–15]. Given that these axons are micrometer-thin, a typical in vivo dMRI voxel—with edge lengths of 1 mm or more—contains millions of them. As a result, the dMRI signal reflects the combined contribution of all axons within a voxel. This aggregate contribution has been proposed to be captured in a scalar metric: the effective axon radius (r_{eff}) [15, 16]. r_{eff} is particularly sensitive to the largest axons, which form the tail of the right-skewed axon radius distribution [17, 18].

Despite theoretical sensitivity to r_{eff}, practical estimation in dMRI experiments remains challenging, and its feasibility has been the subject of longstanding debate in the field. The r_{eff}-related contribution to the dMRI signal is only one among many, with additional signal arising from other tissue compartments [15, 19–22], complex axonal morphology [23–28], axon orientation [29, 30] and noise [31] – making it difficult to isolate the component specific to r_{eff}. Even more critically, the r_{eff}-related signal is inherently weak – so weak that it appears inaccessible to standard clinical scanners. Nonetheless, recent advances in modeling [6, 15, 20, 32–38] and scanner technology [39] have produced promising candidate approaches for r_{eff} mapping. While currently limited to a handful of cutting-edge research scanners worldwide, translation to clinical settings may become feasible with now emerging powerful clinical MRI systems – making this a more timely moment than ever to establish the method.

These technical and modeling advances now shift the burden to experimental

validation. Such validation typically relies on microscopy-based histology of ex vivo tissue [6, 15, 20, 38, 40–43], which offers direct visualization of axons. Yet, while both dMRI and microscopy are sensitive to micrometer-thin axons, the imaging scales are vastly different: dMRI voxels average the signal over millions of axons within millimeter-scale regions, whereas existing microscopy data typically samples only small regions of interest (ROIs) containing a few hundred to a few thousand axons [4, 17, 23, 26, 38, 44, 45]. This mismatch may lead to unreliable r_{eff} [15, 38], since the large axons that dominate r_{eff} are rare and therefore hard to capture in small ROIs. Compounding this issue, existing datasets generally include too few ROIs to support quantitative comparisons across space, leaving validation efforts at a qualitative level.

In this thesis, we move beyond qualitative assessments and provide the first quantitative validation of dMRI-based axon radius mapping in the human brain. We establish a histological reference dataset for dMRI-based axon radius mapping using deep learning-based axon segmentation of light microscopy (LM) images at the scale of in vivo dMRI. We test dMRI-based estimates from both in vivo and ex vivo scans against this reference, and conduct histology-informed simulations to probe limitations and clinical feasibility. Together, these efforts yield the first quantitative evidence that in vivo dMRI captures anatomical variation of axon radii, while also defining the conditions for clinical translation and identifying key limitations of the current modeling approach.

1.1 Outline

The thesis builds on a multimodal dataset of the human corpus callosum, spanning a range of spatial scales from microscopy to dMRI (see Figure 1.1a–d). Each modality contributes to the overall goal of validating and advancing MRI-based axon radius mapping, as outlined below:

- Chapter 2 provides the theoretical and biological background. It introduces the anatomical and functional role of axons and outlines how their radii can be quantified with the modalities used in this thesis. On the histological side, we focus on axon segmentation of microscopy images with deep learning, while on the dMRI side, we review the fundamentals of diffusion MRI and the modeling approaches required to derive the axon-radius related metric r_{eff}.
- Chapter 3 presents a method for generating histological reference data for r_{eff} using deep learning-based segmentation of LM images matched to in vivo dMRI voxel size (see Figure 1.1a,c). We validate this method against manually annotated LM data and higher-resolution electron microscopy (EM) data (see Figure 1.1a-b,e), then apply it to two further corpus callosum samples to build a reference dataset (see Figure 1.1f). The chapter is based on Mordhorst et al. [46, 47].
- Chapter 4 tests the validity of state-of-the-art r_{eff} mapping with dMRI by computing spatial correlations between dMRI-based r_{eff} and the histological

reference established in Chapter 3. In vivo dMRI-based r_{eff} show a significant group-level correlation with histological values (see Figure 1.1a,c,f), providing the first quantitative evidence that dMRI captures spatial axon radius variation. In contrast, ex vivo r_{eff} show no such correlation (see Figure 1.1a,d,f). We also mirror experimental dMRI with simulations anchored in histology, revealing a reduction in sensitivity to large r_{eff} values and a global offset. The chapter is based on Mordhorst et al. [47].

- Chapter 5 investigates the discrepancies identified in Chapter 4. We trace the reduced sensitivity to signal model approximations and highlight anatomical and acquisition factors driving this effect. We also test candidate explanations for the global offset and discuss strategies for mitigating them. The chapter is based on Mordhorst et al. [47].
- Chapter 6 explores the feasibility and clinical potential of r_{eff} mapping. Using histology-informed simulations, we optimize dMRI protocols for clinical scanners and illustrate their potential in a hypothetical application distinguishing individuals with ASD from healthy controls. The chapter is based on Mordhorst et al. [47].
- Chapter 7 synthesizes the main findings of this work, discusses broader implications for dMRI and neuroimaging, and outlines directions for future research.
- Chapter 8 provides the materials and methods underlying the entire thesis. The first sections describe the multimodal dataset of the human corpus callosum in more detail, the acquisition and processing pipelines for each modality, and a framework for histology-based dMRI simulations. These sections apply across Chapters 3 to 6, whereas the final sections detail the analyses specific to each chapter.

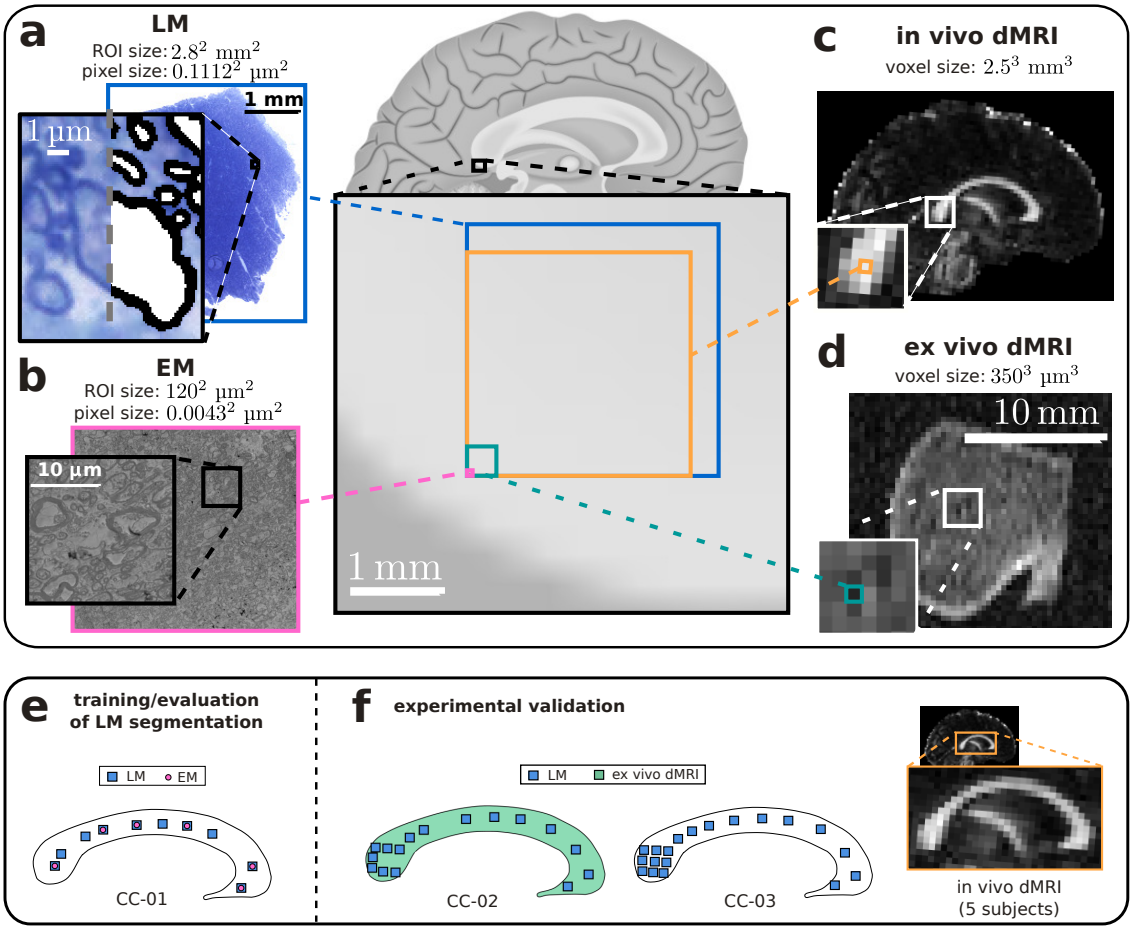

Figure 1.1: A multimodal dataset of the human corpus callosum. **(a–d)** Comparison of imaging scales across modalities. The central illustration shows a mid-sagittal sketch of the human brain with a magnified view of a corpus callosum subregion, highlighting ROI and voxel sizes across: **(a)** light microscopy (LM), with a representative ROI and a magnified view illustrating segmentation of myelin sheath (black) and axonal body (white); **(b)** electron microscopy (EM), with corresponding magnified view; **(c)** in vivo dMRI from this study, shown as a fractional anisotropy (FA) map from one exemplary subject; **(d)** ex vivo dMRI from this study, shown as a diffusion-weighted image. **(e-f)** Overview of the multimodal human corpus callosum dataset and its applications: **(e)** training and evaluation of axon segmentation in LM, using one corpus callosum sample (CC-01) with LM and EM ROIs (see legend); **(f)** experimental validation, using LM and dMRI. Two corpus callosum samples (CC-02 and CC-03) were scanned with LM, CC-02 was additionally scanned with ex vivo dMRI, and five subjects were scanned with in vivo dMRI (image highlights corpus callosum).

Chapter 2

Background

This chapter provides the background for studying axon radii in the human brain. We begin by outlining the biological role of axons and their relevance for neural communication (Section 2.1). We then describe how microscopy and modern image analysis enable axon radii to be quantified at cellular resolution, providing histological benchmarks against which dMRI-based estimates can be validated (Section 2.2). Finally, we introduce how the microscopic motion of water within axons can be exploited with dMRI to non-invasively estimate axon radii at the macroscopic scale (Section 2.3).

2.1 From brain to axon: biological background

This section outlines the hierarchical organization of brain tissue, moving from the whole brain to white matter and finally to the axon, which forms the core focus of this thesis.

The brain can be broadly divided into three tissue types (see Figure 2.1a). Cerebrospinal fluid (CSF) cushions and protects the brain. Gray matter consists mainly of neuronal cell bodies, the information-processing centers of the brain, which are grouped into larger nuclei according to structure and function. White matter is composed primarily of axons – extensions of neurons that enable communication between different brain regions.

White matter

White matter lies in the deeper layers of the brain (see Figure 2.1a) and constitutes about half of its volume. It is mainly formed by bundles of myelinated nerve fibers that connect distant gray matter regions (see Figure 2.1b). Besides axonal bundles, white matter contains glial cells, blood vessels, perivascular cells, and occasional neuronal cell bodies [49]. Among the glia, oligodendrocytes form the myelin sheath that insulates fibers and accelerates conduction, while astrocytes regulate neurotransmitter balance and nutrient uptake from the blood [50]. Through this cellular composition, white matter supports neural signaling, contributes to learning and cognition, and coordinates activity across brain regions [51].

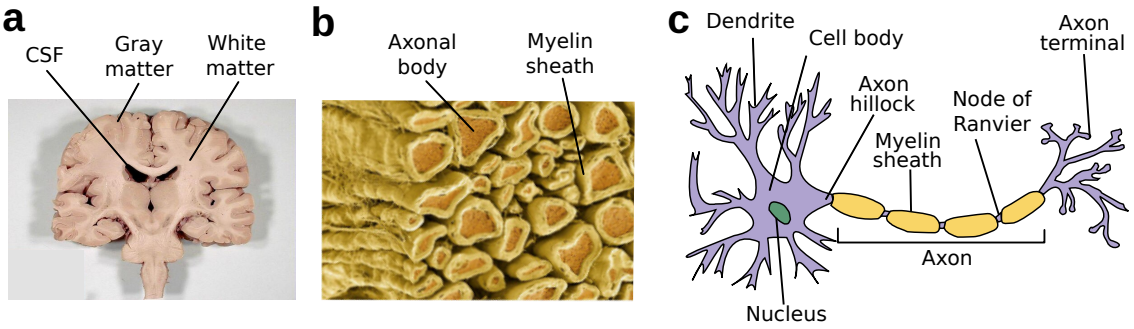

Figure 2.1: From brain to axon. **(a)** Coronal slice of the human brain showing gray matter, white matter, and cerebrospinal fluid (CSF). **(b)** Microstructural phantom of white matter composed of densely packed, myelinated axons. **(c)** Schematic of a neuron, including dendrites, cell body, myelin sheath, nodes of Ranvier, as well as the axon with hillock and terminal.[a,b,c]

[a]Panel (a) adapted from Wikimedia Commons, by Dhp1080, licensed under CC BY-SA 3.0.
[b]Panel (b) reproduced from Novikov et al. [48], with permission from Elsevier. Cropped for clarity.
[c]Panel (c) adapted from Wikimedia Commons, by John A Beal, licensed under CC BY 2.5.

Axons

Neurons communicate via action potentials—brief electrical impulses that travel along cable-like structures called axons (see Figure 2.1c). Each axon originates at the axon hillock, where action potentials are initiated, extends through the axon as the signal propagates, and terminates at axon terminals that transfer the signal to other neurons, muscles, or glands [52, 53]. The conduction speed along the axon depends on its size, with larger axons supporting faster propagation [3, 54]. In mammals, transmission is further accelerated by the myelin sheath, a lipid–protein membrane produced by oligodendrocytes that insulates the axon [55]. Myelin is periodically interrupted by nodes of Ranvier, where the action potential is regenerated, enabling saltatory conduction in which impulses effectively "jump" between nodes. Disruption of axonal structure or myelination impairs action potential propagation and underlies many neurological disorders [56].

Axons vary widely in length—from less than a millimeter to multiple meters [57]—and typically measure between 0.1 and 10 µm in radius [54], depending on their functional role and anatomical location. Large, heavily myelinated axons dominate in motor and sensory pathways that require rapid communication, whereas smaller, lightly myelinated axons prevail in higher-order association areas [5, 17, 54].

2.2 Quantifying axon radii with microscopy

This section introduces the imaging and computational foundations needed to quantify axon radii from microscopy. We first outline the principles of the two-dimensional (2D) microscopy techniques employed in this thesis (Section 2.2.1). We then introduce the general notion of image segmentation (Section 2.2.2). Next, we describe how image segmentation can be approached with convolutional neural

networks (CNNs), including their fundamentals (Section 2.2.3) and their optimization (Section 2.2.4). Finally, we show how axon radii can be approximated from the resulting segmentation (Section 2.2.5).

2.2.1 Microscopy imaging techniques

Microscopy bridges the gap between brain anatomy and cellular microstructure. Light microscopy (LM) surveys large tissue areas at micrometer resolution (Section 2.2.1.1), while electron microscopy (EM) provides nanometer-scale detail of axons, synapses, and myelin (Section 2.2.1.2).

2.2.1.1 Light microscopy

Light microscopy (LM) uses visible light focused through glass lenses to image biological specimens at micrometer resolution. Its resolution is limited by the diffraction of light, typically to 200 nm laterally and 500-700 nm axially [58]. Thus, LM cannot resolve very fine structures such as small axons with radii around 0.1 µm [54]. However, as it is relatively simple and provides a large field-of-view, it is widely used for histological imaging, and often serves as a first localization step before more fine-grained imaging with higher-resolution techniques such as electron microscopy [59].

The basic setup of LM is shown in Figure 2.2 (left side). In LM, a light source is focused through a condenser onto the specimen. Transmitted light is then collected by an objective lens, further magnified by tube optics, and projected onto a camera sensor to form a digital image. In its most common form, brightfield microscopy, contrast arises from differences in absorption or staining of tissue structures, producing dark features on a bright background. A widely used general-purpose stain in histology is hematoxylin and eosin (H&E) [60], which highlights nuclei and cytoplasm. For neurobiological imaging, semi-thin sections of resin-embedded tissue can be stained with toluidine blue, which provides strong contrast of cell bodies, axons, and myelin sheaths [61].

2.2.1.2 Electron microscopy

Electron microscopy (EM) exploits the short wavelength of accelerated electrons to achieve nanometer-scale resolution. Among EM modalities, we focus on transmission electron microscopy (TEM), which passes a high-energy electron beam through an ultra-thin specimen, generating a 2D projection image that reveals internal ultrastructure [62].

The basic setup of TEM is shown in Figure 2.2 (right side). A focused beam of electrons (typically 80–300 kV) is directed onto specimens that are thinner than 100 nm. As electrons traverse the tissue, they are differentially scattered by dense structures such as membranes, organelles, or myelin. The transmitted electrons are collected and magnified by electromagnetic lenses to form an image on a detector.

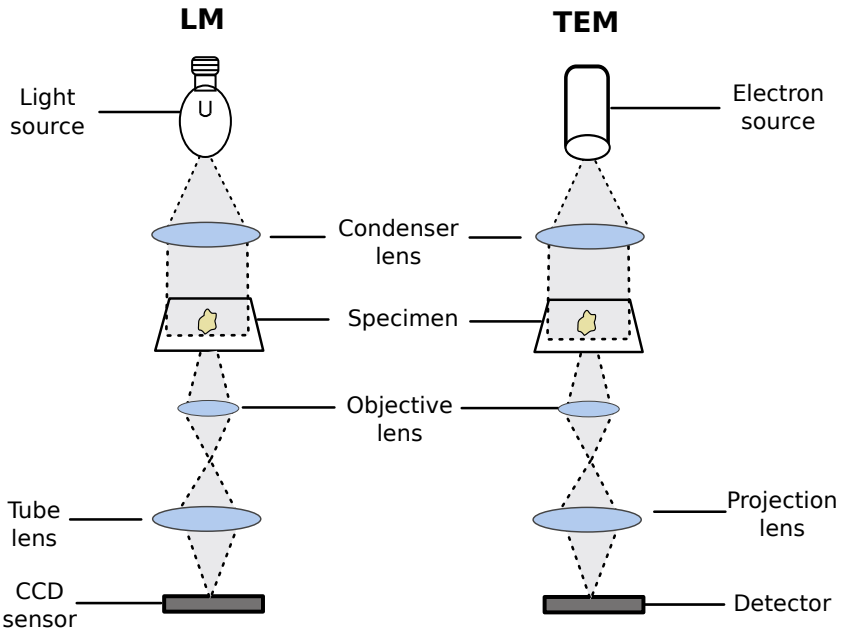

Figure 2.2: Microscopy techniques. Simplified optical paths of light microscopy (LM, left) and transmission electron microscopy (TEM, right). In LM, visible light from a lamp is focused onto the specimen by a condenser, and transmitted light is magnified by glass lenses (objective and tube lens) before being recorded by a charge-coupled device (CCD) camera. In TEM, a high-energy electron beam is shaped by condenser lenses, passes through an ultrathin section, and is magnified by electromagnetic lenses (objective and projection lens) before reaching a fluorescent screen or digital detector.

Regions that scatter more strongly appear darker, while less dense regions appear lighter, producing high-contrast ultrastructural views.

In neurobiology, TEM is commonly combined with heavy-metal stains such as uranyl acetate, lead citrate, and osmium tetroxide to enhance the contrast of biological specimens [61]. This produces relatively uniform contrast across neighboring neuronal processes, enabling the resolution of the smallest axons, dendrites, synapses, and myelin sheaths [17, 45].

2.2.2 Image segmentation

Image segmentation refers to dividing a digital image into distinct regions that share similar characteristics. Conceptually, image segmentation assigns a label to every pixel, such that pixels with the same label belong to the same class or object. The purpose is to transform the raw image into a representation that is easier to interpret and analyze [63]. Among various segmentation paradigms [64], two are most relevant in this work:

- *Semantic segmentation*: each pixel is assigned one of C class labels. Figure 2.3a–b illustrates the segmentation of an EM image into axon, myelin, and background ($C = 3$).
- *Instance segmentation*: in addition to semantic labels, individual objects of the

same class are distinguished. Figure 2.3c illustrates instance segmentation of individual axons. In practice, instance segmentation can be obtained either as a post-processing step applied to semantic segmentation results (e.g., connected component analysis [65] or watershed [66]) or through end-to-end architectures that predict instance-aware masks directly [67, 68].

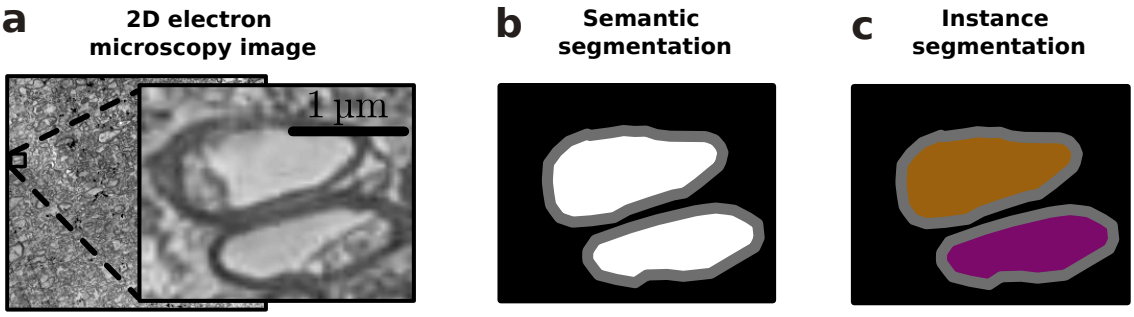

Figure 2.3: Image segmentation. **(a)** Example 2D electron microscopy (EM) image of the human corpus callosum, with a highlighted zoomed region. **(b)** Semantic segmentation. Each pixel is classified as axon (white), myelin sheath (gray), or background (black). **(c)** Instance segmentation. Each axon is assigned a unique label (colors), excluding the myelin sheath.

2.2.3 Semantic segmentation with convolutional neural networks

The semantic segmentation introduced in Section 2.2.2 can be formally defined as a mapping

$$f^\star : \mathbb{R}^{H \times W} \to \{1, \dots, C\}^{H \times W}, \qquad \mathbf{x} \mapsto \mathbf{y}^\star, \tag{2.1}$$

where an input image $\mathbf{x}$ of height H and width W is mapped to a segmentation map $\mathbf{y}^\star$ that assigns each pixel one of C class labels, such as axon, myelin and background in Figure 2.3b.

Today, the unknown target function $f^\star$ is often approximated by a neural network f_θ with parameters θ. In this section, we outline the foundations of feedforward neural networks (Section 2.2.3.1) and their extension to convolutional neural networks (Section 2.2.3.2), which represent a popular approach to semantic segmentation [64].

2.2.3.1 Feedforward neural networks

Feedforward neural networks (FNNs) are the basic models of deep learning [69], building on the early ideas of artificial neurons [70, 71]. An FNN consists of multiple layers of neurons, where each neuron is connected to all neurons of the previous and subsequent layers (see Figure 2.4a). Formally, an FNN with L layers can be described by the concatenation of its layer functions $f^{(l)}_{\theta^{(l)}}$ parameterized by $\theta^{(l)}$:

$$f_\theta(\mathbf{x}) = f^{(L)}_{\theta^{(L)}}\Big(f^{(L-1)}_{\theta^{(L-1)}}(\dots f^{(1)}_{\theta^{(1)}}(\mathbf{x})\dots)\Big), \tag{2.2}$$

where $\theta = \{\theta^{(1)}, \dots, \theta^{(L)}\}$ denotes the set of all network parameters. Each layer corresponds to an affine transformation followed by a nonlinear activation function. Specifically, for neuron j in layer l, the output is

$$z_j^{(l)} = h\left(\sum_{i=1}^{n^{(l-1)}} w_{ji}^{(l)} z_i^{(l-1)} + b_j^{(l)}\right) = h\big(\mathbf{W}^{(l)}\mathbf{z}^{(l-1)} + \mathbf{b}^{(l)}\big)\,, \tag{2.3}$$

where $\mathbf{W}^{(l)} \in \mathbb{R}^{n^{(l)} \times n^{(l-1)}}$ is the weight matrix, $\mathbf{b}^{(l)} \in \mathbb{R}^{n^{(l)}}$ the bias vector, and $h(\cdot)$ a nonlinear activation function applied element-wise (see Figure 2.4b). In practice, $h(\cdot)$ is most often implemented as a rectified linear unit (ReLU) [72],

$$h_{\text{ReLU}}(\alpha) = \max(0, \alpha), \tag{2.4}$$

which keeps positive activations and zeroes out negatives. As alternatives to ReLU, earlier networks frequently used sigmoid or hyperbolic tangent activations.

The first layer is called the input layer, the last layer is the output layer, and all intermediate layers are referred to as hidden layers. The number of neurons in layer l, denoted as $n^{(l)}$, is referred to as the width of the layer. In contrast, the number of layers is called the depth of the network, motivating the term deep learning [69].

While FNNs are conceptually fundamental, they are not well-suited for image segmentation. A naive application in semantic segmentation would require flattening the image into a one-dimensional vector and connecting every pixel to every neuron. Because of this full connectivity, the number of parameters would grow prohibitively large, making FNN-based image segmentation infeasible for anything but very small images.

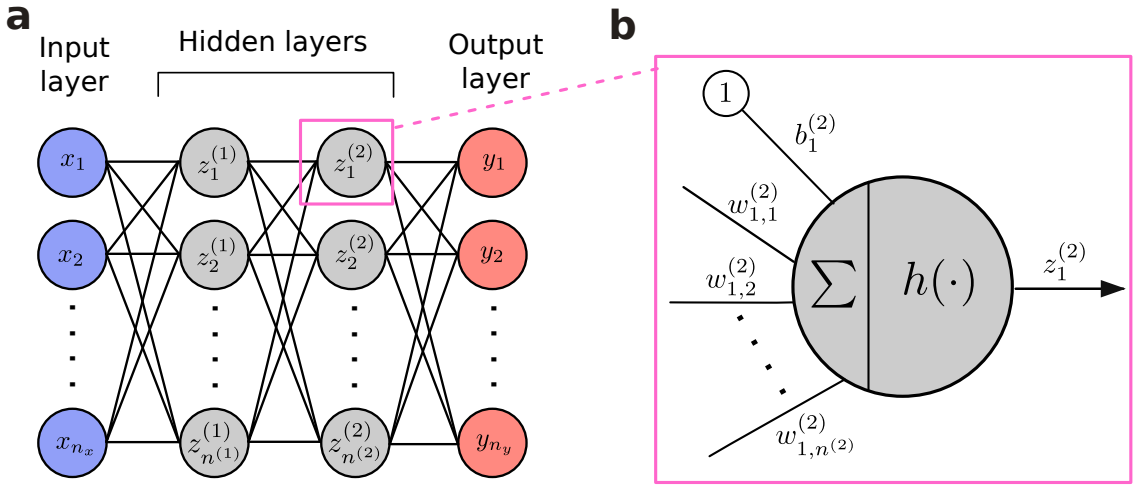

Figure 2.4: Feedforward neural network. **(a)** Illustration of a feedforward neural network (FNN) with an input layer, two hidden layers, and an output layer. Each neuron is fully connected to all neurons in the preceding and subsequent layers. **(b)** Zoom on a single neuron. The inputs are linearly combined using weights and a bias term, followed by the application of a nonlinear activation function $h(\cdot)$ to produce the neuron output.

2.2.3.2 Convolutional neural networks

Convolutional neural networks (CNNs) [73, 74] overcome the full connectivity constraints of FNNs by efficiently exploiting the spatial structure of image data. Rather than connecting every input pixel to every neuron, CNNs employ small convolutional kernels, drastically reducing the number of parameters while preserving local spatial relationships.

Convolution operation

In CNNs, the dense affine transformation of Equation (2.3) is replaced by a convolution. For a 2D image $\mathbf{I} \in \mathbb{R}^{H \times W}$ and convolutional kernel $\mathbf{K} \in \mathbb{R}^{M_H \times M_W}$, the discrete convolution is defined as

$$(\mathbf{I} * \mathbf{K})(x, y) = \sum_{i=1}^{M_H} \sum_{j=1}^{M_W} \mathbf{I}(x + i,\, y + j)\, \mathbf{K}(i, j). \tag{2.5}$$

This operation is technically cross-correlation, because the kernel is applied directly without flipping it as in the mathematical definition of convolution. Nevertheless, it is conventionally referred to as convolution in the deep learning literature [69]. The resulting output is typically referred to as a feature map. This definition extends naturally to higher dimensions, such as three-dimensional (3D) volumes or two-dimensional (2D) images with multiple channels. Compared to the dense connections in FNNs, convolutions offer two main advantages:

- *Weight sharing*: the same kernel is applied across the entire input (see Figure 2.5a). To extract different features, multiple kernels are used in parallel. Note that weight sharing also leads to translational equivariance, i.e., a shifted input leads to a shifted feature map with the same pattern [69].
- *Sparse connectivity*: each output neuron depends only on a local neighborhood in the input, defined by the kernel size (typically 3–7 pixels per dimension), rather than on all input values. Stacking multiple convolution layers enlarges the effective receptive field, enabling deeper layers to integrate information from progressively larger input regions (see Figure 2.5b).

CNN architectures

While convolutions form the central building block of CNNs, practical segmentation networks combine them with other types of layers. A widely used example is the U-Net architecture [75], shown in Figure 2.6. Although U-Net is a specific design, it illustrates several general concepts common to CNNs for segmentation [76].

Within each layer, multiple convolutional filters are typically applied in parallel to extract different features from the input (see numbers annotated on top of layers in Figure 2.6). In addition, convolutions are stacked sequentially (see purple arrows in Figure 2.6), enabling deeper layers to build increasingly abstract representations from earlier ones.

Besides convolutional layers, CNNs typically use pooling layers to aggregate local neighborhoods [77, 78], which reduces the spatial resolution of feature maps (see red

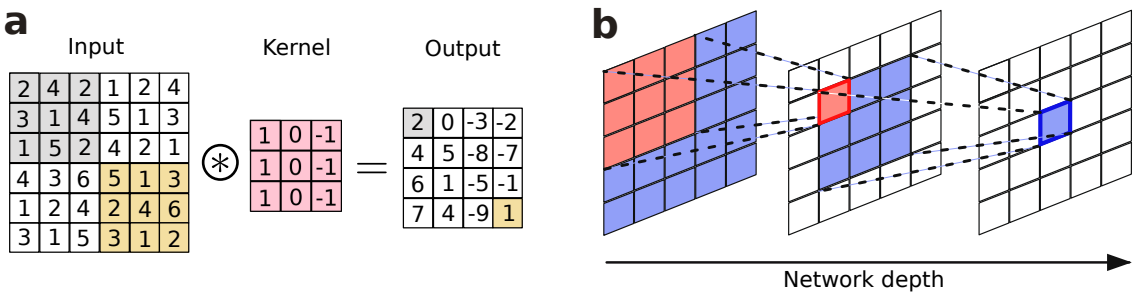

Figure 2.5: Convolution and receptive field. **(a)** Example of a 2D convolution with a 3×3 kernel. The highlighted input regions and corresponding output values illustrate how the kernel aggregates local information. **(b)** Growth of the receptive field with increasing network depth. Although each convolutional layer is locally connected, stacking layers expands the effective receptive field, allowing deeper features to integrate information from larger input regions. The highlighted output unit on the right depends on all pixels of the leftmost feature map after stacking convolutional layers.

arrows in Figure 2.6). For instance, max pooling [77] with a 2×2 window halves the feature map size in each spatial dimension, lowering computational complexity and introducing local translational invariance. Since the goal of semantic segmentation is to produce an output $\mathbf{y}$ with the same spatial dimensions as the input image $\mathbf{x}$, these pooling steps must later be reversed by upsampling operations (see green arrows in Figure 2.6). This structure, with several pooling layers followed by corresponding upsampling layers, is characteristic of many CNNs and is often referred to as an encoder–decoder architecture.

The final 1×1 convolution (see turquoise arrow in Figure 2.6) reduces the feature maps to per-pixel class scores, also called logits, from which per-class probabilities can be approximated via softmax (for multi-class segmentation) or sigmoid (for binary segmentation) operations.

A further element of U-Net are the skip connections (see gray arrows in Figure 2.6), which transfer high-resolution features from the encoder to the decoder. These connections preserve fine-grained details and are crucial for accurate delineation of segmentation boundaries.

2.2.4 Optimizing neural networks

The successful application of neural networks depends not only on their architecture, but also on how well their weights θ are optimized. Here, we introduce the supervised learning paradigm (Section 2.2.4.1) and the iterative optimization scheme used for training (Section 2.2.4.2).

2.2.4.1 Supervised learning

The process of optimizing the weights θ of neural networks f_θ introduced in Section 2.2.3 is typically referred to as training. In this work, we focus on the supervised learning paradigm, where the network is trained using a dataset of input–target

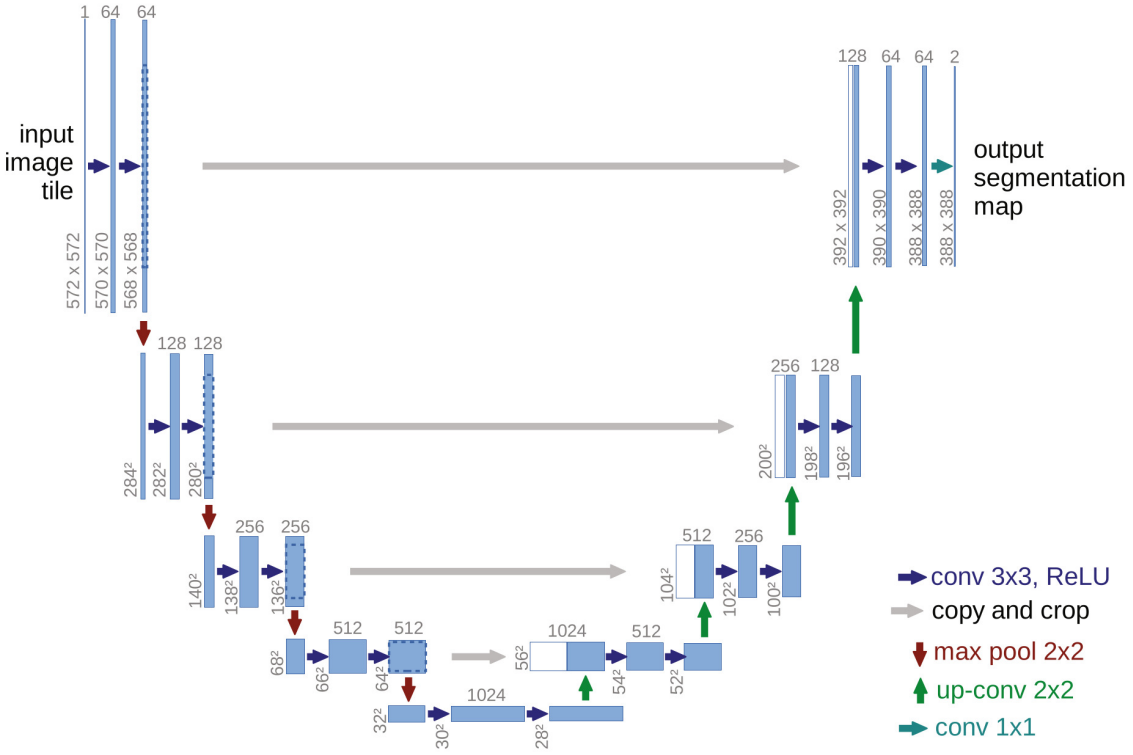

Figure 2.6: The U-Net architecture. Each blue box represents a multi-channel feature map. The number of channels is shown above the box, and the spatial resolution (x–y size) is indicated at its lower left corner. White boxes denote feature maps that are copied and passed forward through skip connections. The arrows correspond to the main operations: purple arrows indicate convolutions, red arrows indicate pooling, green arrows indicate upsampling, turquoise arrows indicate the final 1×1 convolution, and gray arrows denote skip connections between encoder and decoder.[a]

[a]Reproduced from Ronneberger et al. [75] with permission from Springer.

pairs:

$$\mathcal{D} = \{(\mathbf{x}^{(1)}, \mathbf{y}^{(1)}), (\mathbf{x}^{(2)}, \mathbf{y}^{(2)}), \ldots, (\mathbf{x}^{(m)}, \mathbf{y}^{(m)})\}, \tag{2.6}$$

Here, each target $\mathbf{y}^{(i)}$ provides pixelwise expert annotations for the corresponding input image $\mathbf{x}^{(i)}$.

The goal is not to achieve perfect performance on $\mathcal{D}$ but to train f_θ so that it generalizes well to unseen data. This emphasis on generalization is crucial: a network that simply memorizes $\mathcal{D}$ will fail to provide useful predictions in practice. To assess and promote generalization, $\mathcal{D}$ is typically partitioned into three disjoint subsets:

- *Training set* $\mathcal{D}_{\text{train}}$: used to optimize the network parameters θ.
- *Validation set* $\mathcal{D}_{\text{val}}$: used to monitor generalization performance during training and to tune hyperparameters, i.e., parameters not learned during training such as optimizer settings (e.g., learning rate) or architectural choices (e.g., network depth).
- *Test set* $\mathcal{D}_{\text{test}}$: reserved for the final evaluation of the network on unseen data.

2.2.4.2 Training loop

Training typically proceeds in an iterative loop. In each iteration, the network processes a *mini-batch*, i.e., a randomly sampled subset of $\mathcal{D}_{\text{train}}$, rather than the entire training set at once. The sequence of steps in one iteration is as follows:

1. *Forward pass:* compute predictions $f_\theta(\mathbf{x})$ for the mini-batch.
2. *Loss evaluation:* compare predictions with ground-truth labels using a differentiable loss function.
3. *Backward pass:* compute gradients of the loss with respect to the network weights θ.
4. *Parameter update:* update θ based on these gradients.

This iteration is repeated over successive mini-batches; one complete pass over $\mathcal{D}_{\text{train}}$ is an epoch. Throughout training, performance is evaluated on $\mathcal{D}_{\text{val}}$ to monitor generalization, and training is typically stopped when validation performance no longer improves, indicating the onset of overfitting to $\mathcal{D}_{\text{train}}$. In practice, validation can also be performed within a cross-validation framework, where training and validation sets are repeatedly re-partitioned to make the training procedure less dependent on a single partitioning of the data. Finally, the generalization of the trained network is assessed on $\mathcal{D}_{\text{test}}$ using evaluation metrics.

The following paragraphs introduce in more detail the main components of this procedure: data preparation, loss functions, gradient-based optimization, regularization strategies, and evaluation metrics.

Data preparation

In addition to dataset splitting, input data are often standardized prior to training. Standardization refers to rescaling the input features (e.g., image intensities) to a common range or distribution, such as zero mean and unit variance, in order to stabilize and accelerate optimization.

Another common strategy is data augmentation, where new training examples are generated from existing data by applying label-preserving transformations such as rotations, reflections, or random crops in the case of images. Data augmentation improves the robustness of the learned model and can be interpreted as an implicit form of regularization, as it enlarges the effective training distribution and reduces overfitting.

Loss function

Training proceeds by minimizing a loss function that quantifies the discrepancy between the predicted segmentation and the ground-truth labels. For segmentation, the loss is typically defined at the pixel level. For multi-class segmentation, a common choice is the cross-entropy loss:

$$L_{\text{CE}}(\hat{y}, y) = -\frac{1}{MN} \sum_{i=1}^{M} \sum_{j=1}^{N} \sum_{c=1}^{C} \mathbb{1}\{y_j^{(i)} = c\} \log \hat{p}_{j,c}^{(i)}, \tag{2.7}$$

where M is the number of training examples, N is the number of pixels per example, C is the number of classes, $y_j^{(i)}$ is the ground-truth class label of pixel j in example i, $\hat{p}_{j,c}^{(i)}$ is the predicted probability of class c for that pixel, and $\mathbb{1}\{\cdot\}$ is the indicator function that equals 1 if its argument is true and 0 otherwise.

Gradient-based optimization

The loss function is minimized with respect to the network parameters θ using gradient-based optimization. The key idea is to compute the gradient of the loss $L(\theta)$ (e.g., L_{CE} from Equation (2.7)) with respect to all parameters, $\nabla_\theta L(\theta)$, and to update the parameters in the direction of steepest descent:

$$\theta \leftarrow \theta - \eta \nabla_\theta L(\theta), \tag{2.8}$$

where $\eta > 0$ is the learning rate that controls the step size.

Gradients are computed efficiently using the backpropagation algorithm, which applies the chain rule of calculus across the network layers. In practice, optimization is performed on random subsets of the data (mini-batches), leading to stochastic gradient descent (SGD). This reduces memory requirements and introduces randomness that often improves generalization. There are several other optimizers, which enable adaptive learning rates [79] or accelerated updates using momentum [80].

Regularization

While optimization minimizes the loss on the training data, the ultimate goal is good performance on unseen data. To reduce overfitting and improve generalization, various regularization strategies are commonly applied.

- *Weight decay* (or ℓ_2 regularization) penalizes large parameter values by adding a quadratic term $\lambda\|\theta\|_2^2$ to the loss.
- *Dropout* randomly sets activations to zero during training, forcing the network to rely on multiple redundant pathways and thereby preventing co-adaptation of neurons [81].
- *Data augmentation* (see above) can also be interpreted as a form of regularization, since it enlarges the effective training distribution and reduces variance.

Evaluation metrics

While differentiable losses such as cross-entropy are required for training, segmentation performance is often assessed with more interpretable evaluation metrics. For binary pixel-wise segmentation, common metrics include balanced accuracy, recall, precision, and Dice score:

$$\text{Balanced accuracy} = \tfrac{1}{2}\left(\tfrac{|\text{TP}|}{|\text{TP}|+|\text{FN}|} + \tfrac{|\text{TN}|}{|\text{TN}|+|\text{FP}|}\right), \tag{2.9}$$

$$\text{Recall} = \tfrac{|\text{TP}|}{|\text{TP}|+|\text{FN}|}, \tag{2.10}$$

$$\text{Precision} = \tfrac{|\text{TP}|}{|\text{TP}|+|\text{FP}|}, \tag{2.11}$$

$$\text{Dice} = \tfrac{2\cdot|\text{TP}|}{2\cdot|\text{TP}|+|\text{FP}|+|\text{FN}|}, \tag{2.12}$$

where |TP|, |TN|, |FP|, and |FN| denote the number of true positive, true negative, false positive, and false negative pixels, respectively. In contrast to the training loss, which operates on predicted probabilities, these metrics are usually computed from hard predictions, where each pixel is assigned to a single class (e.g., by thresholding in the binary case or by taking the argmax in the multi-class case). The metrics can be extended to multi-class segmentation by, for example, computing per-class metrics and averaging across classes.

2.2.5 From semantic segmentation to axon radii

A common way to extract morphological information of axons, such as their radius, is to first identify axons in microscopy images and then derive radius estimates from the resulting masks. To quantify axon radii from segmented instances in microscopy images, each axon mask must be reduced to a single radius value. In 2D microscopy, sections are typically cut orthogonal to the axonal orientation, but axon cross-sections are rarely perfect circles (see Figure 2.7a). There are several geometric approximations to estimate the axon radius r:

- *Circular equivalent radius*: the radius of a circle with the same cross-sectional area as the segmented axon (see Figure 2.7b). This measure is robust to irregular shapes but can be biased by axons cut at oblique angles. It is frequently used in histological studies [26, 82, 83].
- *Elliptical minor axis*: half of the short axis of a fitted ellipse (see Figure 2.7c). This corresponds to the true radius if the axon is a perfect cylinder cut at an oblique angle, and is frequently used in histological studies [4, 17, 38, 45].
- *Elliptical major axis*: half of the long axis of a fitted ellipse (see Figure 2.7d). This tends to overestimate the radius for oblique sections or elongated axons, and is therefore rarely used [15].

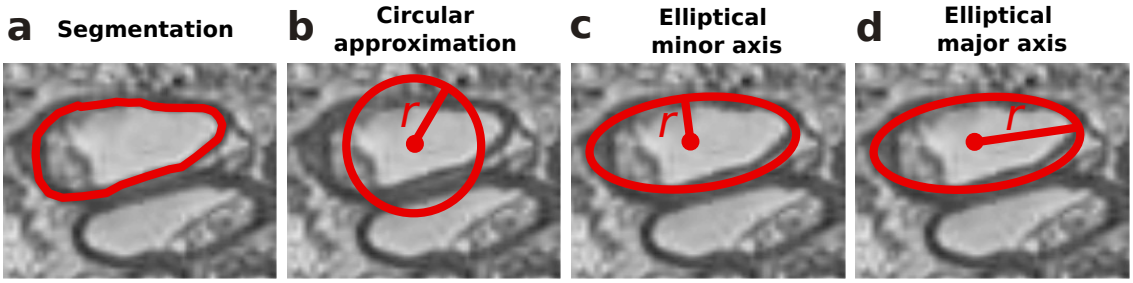

Figure 2.7: Axon radius approximations. **(a)** Segmentation of an axon from a 2D electron microscopy (EM) image (myelin outlined). **(b)** Circular equivalent radius: r is defined as the radius of a circle with the same cross-sectional area as the segmented axon. **(c)** Elliptical minor axis: r corresponds to half of the fitted ellipse's short axis. **(d)** Elliptical major axis: r corresponds to half of the fitted ellipse's long axis.

2.3 Quantifying axon radii with diffusion MRI

This section introduces the physical and methodological foundations needed to understand how MRI can be used to infer axon radii. We begin with the basic principles of MRI and the mechanisms by which nuclear spins generate measurable signals (Section 2.3.1). These concepts are then extended to diffusion-weighted MRI (dMRI), where the random motion of water molecules encodes information about tissue microstructure (Section 2.3.2). We next describe the practical aspects of acquiring dMRI data (Section 2.3.3) and discuss common acquisition imperfections (Section 2.3.4). Finally, we present signal modeling in dMRI, progressing from general mathematical representations (Section 2.3.5) to biophysical models of white matter (Section 2.3.6), culminating in approaches that relate the measured signal to axon radii.

2.3.1 Fundamentals of MRI

Magnetic resonance imaging (MRI) is a non-invasive imaging method that detects signals from atomic nuclei, most commonly hydrogen protons, in a strong magnetic field. In essence, MRI works by exciting these nuclei and then "listening" to the subtle signals they emit as they relax, in a way that allows spatial mapping to form detailed images with diverse contrasts.

Nuclear magnetic resonance

MRI relies on the physical phenomenon of nuclear magnetic resonance (NMR) [84–86]. NMR arises from the interaction between the intrinsic angular momentum of atomic nuclei, known as spin, and an external magnetic field $\mathbf{B}_0 \in \mathbb{R}^3$ generated by the MRI scanner. Nuclei with nonzero spin respond to this field by aligning with or against its direction, typically along the z-axis of the scanner coordinate system.

Despite this alignment, each individual magnetic moment continues to precess around the axis of $\mathbf{B}_0$. This precession occurs at a characteristic frequency, the so-called Larmor frequency:

$$\omega_0 = \gamma B_0, \tag{2.13}$$

where γ is the gyromagnetic ratio of the nucleus in units of rad/s/T, and $B_0 = |\mathbf{B}_0|$ is the static magnetic field strength. For protons, $\gamma \approx 2.675 \times 10^8\,\mathrm{rad/(s\,T)}$, corresponding to $\gamma/2\pi \approx 42.58\,\mathrm{MHz/T}$. Thus, the precession frequency increases linearly with field strength, e.g., $\omega_0/2\pi \approx 64\,\mathrm{MHz}$ at $B_0 = 1.5\,\mathrm{T}$ and $\omega_0/2\pi \approx 300\,\mathrm{MHz}$ at $B_0 = 7\,\mathrm{T}$, spanning the range of typical in vivo field strengths.

At thermal equilibrium, spins are distributed between the parallel (low-energy) and anti-parallel (high-energy) states relative to $\mathbf{B}_0$. Because the lower-energy state is slightly more populated, this imbalance gives rise to a small net macroscopic magnetization $\mathbf{M}_0$ parallel to $\mathbf{B}_0$. Its magnitude is given by

$$M_0 = \frac{N\gamma^2\hbar^2 B_0}{4kT}, \tag{2.14}$$

where N is the number of spins per unit volume, $\hbar = 1.054\,571\,817 \times 10^{-34}\,\mathrm{J\,s}$ is the reduced Planck constant, $k = 1.380\,649 \times 10^{-23}\,\mathrm{J/K}$ is Boltzmann's constant, and T is the absolute temperature. As this equation shows, M_0 increases with stronger magnetic fields and higher spin density, and decreases with temperature. Because the spin population imbalance is very small at physiological temperatures compared to absolute zero, a large number of spins is required to generate a detectable signal. This is why MRI predominantly detects the signal from hydrogen nuclei (^{1}H), which are highly sensitive to magnetic resonance and abundant in biological tissue [87].

Excitation and relaxation

The static equilibrium magnetization M_0 in Equation (2.14) does not generate a measurable signal, because at the macroscopic level it is constant in time and produces no oscillating magnetic field. To generate a detectable signal, an oscillating (time-dependent) radiofrequency (RF) magnetic field $\mathbf{B}_1(t)$ is applied in the transverse (xy) plane at the Larmor frequency ω_0. This field tips the net magnetization away from the z-axis into the transverse plane and synchronizes the spin phases, creating a coherent transverse component M_{xy} that induces a measurable voltage in the surrounding RF coil by electromagnetic induction. The total magnetic field during excitation is then

$$\mathbf{B}(t) = \mathbf{B}_0 + \mathbf{B}_1(t). \tag{2.15}$$

This process is called excitation, and the amount of tipping is the flip angle.

Once the RF pulse is turned off, the magnetization does not remain tipped in the transverse plane. Instead, it gradually returns to its equilibrium configuration – a process known as relaxation. The dynamics of excitation and relaxation are described by the Bloch equations [86]:

$$\frac{d\mathbf{M}}{dt} = \gamma\,\mathbf{M} \times \mathbf{B}(t) - \begin{bmatrix} M_x/T_2 \\ M_y/T_2 \\ (M_z - M_0)/T_1 \end{bmatrix}, \tag{2.16}$$

where $\mathbf{M} = (M_x, M_y, M_z)$ is the net magnetization vector, and T_1 and T_2 are the longitudinal and transverse relaxation time constants.

In the special case of free precession in the static field $\mathbf{B}_0$ after the RF pulse is turned off, and in the absence of applied gradients, the magnetization decays over time. When focusing on the slowly varying signal envelope (i.e., in the so-called rotating frame, which ignores the rapid Larmor precession at frequency ω_0), there are two distinct magnetization components:

- *Longitudinal relaxation* (spin–lattice relaxation) describes recovery of the longitudinal (z-)component due to spins returning to thermal equilibrium:

$$M_z(t) = M_0\left(1 - e^{-t/T_1}\right).$$

- *Transverse relaxation* (spin–spin relaxation) describes decay of the transverse

(xy-)component due to spins dephasing:

$$M_{xy}(t) = M_{xy}(0)e^{-t/T_2}.$$

Tissue-dependent variations in T_1 and T_2 influence the amplitude and decay of the MR signal, and thus underpin the contrast mechanisms in conventional MRI.

Spatial encoding and image reconstruction

The MRI signal arises from the transverse magnetization of the entire object. To obtain spatially resolved images, additional linear magnetic field gradients $\mathbf{G}_{\text{enc}}(t) = \big(G_x(t), G_y(t), G_z(t)\big)^\top$ are superimposed onto the main static field $\mathbf{B}_0$, thereby modulating the local resonance frequency ω_0 (see Equation (2.13)). The resonance frequency thus becomes spatially dependent:

$$\omega(\mathbf{r}, t) = \omega_0 + \gamma\, \mathbf{G}_{\text{enc}}(t) \cdot \mathbf{r}, \tag{2.17}$$

where $\mathbf{r} = (x, y, z)^\top$ is the spatial position.

In standard imaging sequences, spatial information is encoded along three approximately orthogonal directions. The corresponding gradients are applied in distinct ways, leading to three conceptually different encoding mechanisms [88]:

- *Slice selection:* A gradient is applied during RF excitation (often along z), so that only spins within a narrow frequency band $\Delta\omega$—corresponding to a physical slice—are excited. Because the resonance frequency varies linearly with position along z, this frequency band corresponds to a slice thickness $\Delta z = \Delta\omega/(\gamma G_z)$.
- *Frequency encoding (readout):* A gradient is applied during signal acquisition (often along x), so that spins at different x positions precess at different frequencies $\omega(x) = \omega_0 + \gamma G_x x$.
- *Phase encoding:* A gradient (e.g., along y) is applied briefly before readout, imparting position-dependent phase shifts $\Delta\phi(y) = \gamma G_y\, \tau_{\text{PE}}\, y$, where τ_{PE} is the gradient duration. Because the phase is 2π-periodic, a single measurement cannot uniquely distinguish different positions along y. The ambiguity is resolved by repeating the sequence with a series of incremented G_y values, each filling a different line of k-space (see below).

For a single slice z, the combination of frequency and phase encoding leads to a spatial Fourier relation between the object $I(x, y)$ and the measured signal:

$$S(t) \;=\; \iint I(x, y)\; e^{-i\,2\pi\,[\,k_x(t)\,x\,+\,k_y(t)\,y\,]}\; dx\, dy, \tag{2.18}$$

where the k-space coordinates are defined by

$$\mathbf{k}(t) = \frac{\gamma}{2\pi} \int_0^t \mathbf{G}(t')\, dt', \tag{2.19}$$

with $\mathbf{k}(t) = (k_x(t), k_y(t), k_z(t))^\top$. Sampling multiple $\mathbf{k}(t)$ points traces a trajectory

in k-space, from which the image is reconstructed via inverse Fourier transform. In conventional sequences, $k_x(t)$ varies continuously during the readout of a single line, while k_y is incremented stepwise across successive repetitions to disentangle the phase information.

2.3.2 From MRI to diffusion MRI

While conventional MRI contrasts arise from differences in relaxation properties, diffusion-weighted MRI (dMRI) is sensitive to the random motion of water molecules. This motion during a dMRI experiment occurs on the micrometer scale, thereby providing access to tissue microstructure far smaller than the typical millimeter-scale image resolution of dMRI.

Basic principles of diffusion

The physical basis of diffusion MRI lies in the Brownian motion of water molecules. This motion can be described by the diffusion propagator $P(\mathbf{u}, t)$, i.e., the probability density that a spin undergoes a net displacement $\mathbf{u} \in \mathbb{R}^3$ during the diffusion time t [89]. In a homogeneous medium with constant, isotropic diffusivity D, the motion of water molecules is governed by Fick's second law [90].

$$\frac{\partial P(\mathbf{u}, t)}{\partial t} = D\nabla^2 P(\mathbf{u}, t), \tag{2.20}$$

whose fundamental solution is a 3D Gaussian:

$$P(\mathbf{u}, t) = \frac{1}{(4\pi Dt)^{3/2}} \exp\left(-\frac{|\mathbf{u}|^2}{4Dt}\right), \tag{2.21}$$

from which the mean squared displacement follows as

$$\langle |\mathbf{u}|^2 \rangle = 6Dt, \tag{2.22}$$

also known as Einstein's relation for Brownian motion [91].

The signal in diffusion MRI

The MRI signal can be sensitized to molecular diffusion by applying time-dependent magnetic field gradients $\mathbf{G}(t)$, typically referred to as diffusion gradients. Spins that move during or between these gradients accumulate different phases, which reduces phase coherence and attenuates the measured signal. Formally, this effect is captured by augmenting the Bloch equations (see Equation (2.16)) with a diffusion term, yielding the Bloch–Torrey equations [92].

In the narrow-pulse approximation, where gradient pulses are considered infinitely short, the diffusion-weighted signal can be expressed as the Fourier transform of the diffusion propagator $P(\mathbf{u}, t)$ [89]:

$$\frac{S}{S_0}(t) = \int P(\mathbf{u}, t) \exp\left(-i\gamma \int_0^T \mathbf{G}(t')dt' \cdot \mathbf{u}\right) d\mathbf{u}, \tag{2.23}$$

where S denotes the diffusion-weighted signal and S_0 the reference signal without diffusion weighting, and $\mathbf{u} \in \mathbb{R}^3$ the net spin displacement.

More generally, the signal can be expressed in terms of the accumulated spin phase ϕ along each trajectory:

$$\frac{S}{S_0} = \langle e^{-i\phi} \rangle, \qquad \phi = \gamma \int_0^T \mathbf{G}(t) \cdot \mathbf{u}(t)\, dt, \tag{2.24}$$

where T denotes the duration of the diffusion-sensitizing gradient waveform. This formulation emphasizes that diffusion weighting arises from incoherent phase accumulation across spin trajectories.

Cumulant expansion and Gaussian phase approximation

Since Equation (2.24) is the characteristic function of the phase distribution, the logarithm of the signal can be expanded in cumulants [93]:

$$\ln \frac{S}{S_0} = \sum_{n=1}^{\infty} \frac{(-i)^n}{n!} \langle \phi^n \rangle_c. \tag{2.25}$$

Because the phase distribution is symmetric around zero, all odd cumulants vanish. In addition, the signal can be further simplified under the widely used Gaussian phase approximation (GPA), which assumes that the accumulated phase ϕ is Gaussian-distributed. Since a Gaussian random variable is fully determined by its mean and variance, all cumulants beyond the second vanish, and the signal reduces to

$$\frac{S}{S_0} = \exp\left(-\tfrac{1}{2} \langle \phi^2 \rangle_c\right). \tag{2.26}$$

The GPA is exact in the extreme limits of diffusion time [94, 95]. At short diffusion times, water molecules move almost freely because restrictive boundaries are rarely encountered, while at long diffusion times, repeated interactions with restrictions average out to Gaussian behavior. At intermediate diffusion times, the approximation is not exact, but it remains sufficiently accurate for many applications [93, 96, 97].

Free diffusion signal

In the simplest case of free Gaussian diffusion, the signal reduces to a mono-exponential decay:

$$\frac{S}{S_0} = \exp(-bD), \tag{2.27}$$

where b summarizes the diffusion weighting. The explicit form of b depends on the gradient waveform, which will be detailed in the next section.

2.3.3 Practical diffusion MRI measurements

In practice, dMRI combines diffusion gradients with RF pulses and imaging readouts to encode molecular motion and reconstruct spatially resolved images. This section introduces commonly used acquisition schemes.

Pulsed gradient spin echo sequence

The pulsed gradient spin echo (PGSE) sequence [98] is the basic sequence underlying most diffusion MRI experiments. It combines RF pulses for excitation and refocusing with diffusion gradient pulses to encode molecular motion (see Figure 2.8a). A 90° RF pulse first excites the spins, followed by a pair of monopolar diffusion gradients placed symmetrically around a 180° RF refocusing pulse. The refocusing pulse restores dephasing from static field inhomogeneities, while the gradient pair encodes sensitivity to molecular displacement.

For stationary spins (see Figure 2.8b, top row), the phase shift induced by the first diffusion gradient is exactly cancelled by the second. This yields a full echo at the echo time (TE), with the same amplitude as the reference signal without diffusion weighting, $S = S_0$. For diffusing spins (see Figure 2.8b, bottom row), random displacements through diffusive motion between the two gradient pulses prevent perfect rephasing. The resulting spread of individual spin phases reduces the net transverse magnetization (black arrow), leading to an attenuated signal $S = S_0 e^{-bD}$.

The degree to which the sequence attenuates the signal from diffusing spins is quantified by the diffusion weighting [99]:

$$b = \gamma^2 g^2 \delta^2 (\Delta - \delta/3), \tag{2.28}$$

where $g = |\mathbf{G}|$ is the amplitude of the diffusion gradient, δ is the gradient duration, and Δ the separation between the two gradient pulses (see Figure 2.8a). This expression for b follows from integrating the squared accumulated gradient moment $q(t) = \gamma \int_0^t G(t')dt'$, which determines the phase variance of the accumulated spin phase ϕ. The term $\Delta - \frac{\delta}{3}$ can be interpreted as the effective diffusion time t_{eff}, which represents the experimental counterpart of the characteristic diffusion time t introduced in basic diffusion theory (see Section 2.3.2). Here, the correction term $-\delta/3$ reflects that dephasing during a finite gradient pulse is partly self-cancelled, so that in the idealized limit of infinitely short pulses t_{eff} simplifies to Δ.

The b-values used in practical applications depend on the microstructural features of interest. According to Equation (2.28), higher b can be achieved by increasing g, which is limited by the scanner's maximum achievable g, denoted as $g_{\max}$ throughout this thesis. The alternative way to increase b—via larger δ and Δ—incurs a penalty in signal-to-noise ratio (SNR), because these parameters prolong TE. A longer TE increases the time over which T_2 relaxation acts, reducing signal amplitude and thus SNR. The repetition time (TR) is another important timing parameter: it defines the interval between two successive excitation pulses in a repeating sequence of pulses and echoes (not annotated in Figure 2.8) and thereby determines, together with the number of repetitions, the total measurement time.

Echo planar imaging

In principle, diffusion weighting could be applied to a single spatial location by combining PGSE diffusion-encoding gradients with RF pulses for excitation and

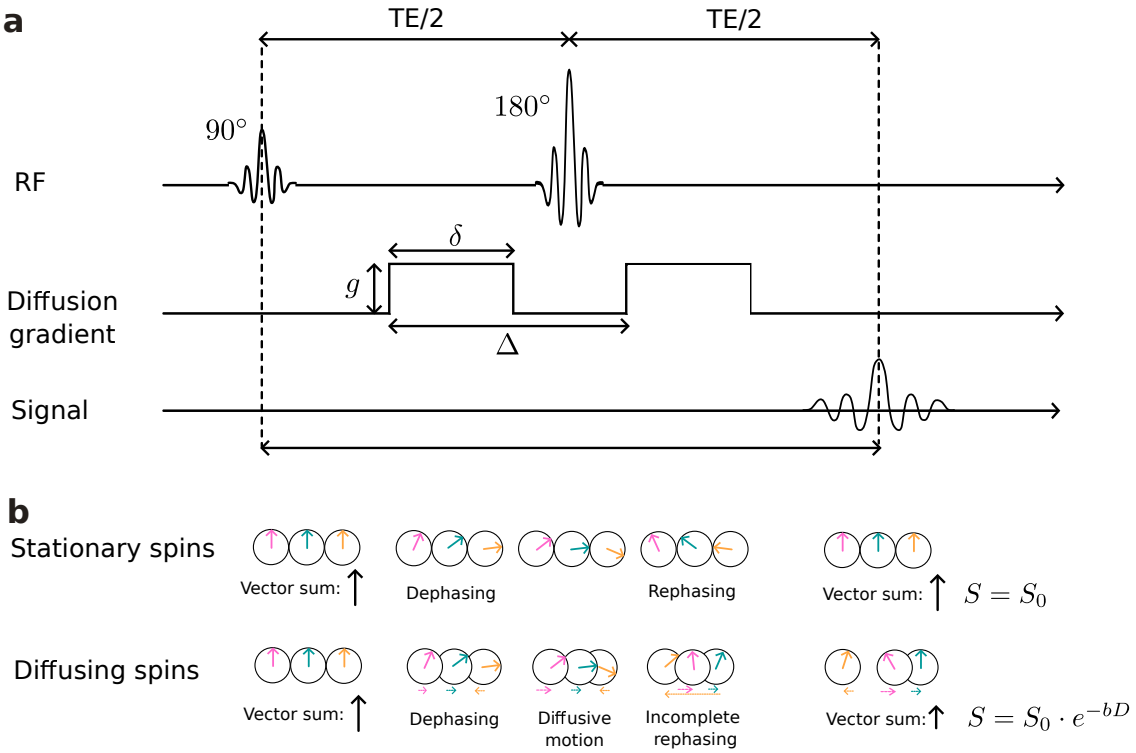

Figure 2.8: Pulsed gradient spin echo (PGSE) sequence. **(a)** Sequence timing diagram with a 90° RF pulse, two monopolar diffusion gradients (amplitude g, duration δ, separation Δ), and a 180° refocusing pulse. The signal is read out at the echo time (TE). **(b)** Illustration of spin phase evolution. Black arrows denote the net transverse magnetization, and colored arrows represent individual spin phases. For stationary spins (top row), the phase accrued during the first gradient is flipped by the 180° pulse and exactly refocused by the second gradient, yielding $S = S_0$. For diffusing spins (bottom row), motion during the interval Δ causes incomplete rephasing, leading to phase dispersion. As a consequence, the net transverse magnetization (black arrow) and signal $S = S_0 e^{-bD}$ are attenuated.[a].

[a]Panel (b) based on Dietrich et al. [100]

refocusing. In practice, dMRI requires imaging a whole object, which is achieved by combining diffusion encoding with additional gradients for spatial localization. A common approach is echo planar imaging (EPI) [101], where the entire set of k-space lines for a 2D image is traversed in a rapid echo train after the refocusing pulse, centered around the spin echo (TE). In single-shot EPI, all lines are acquired in a single echo train, enabling fast imaging with high motion robustness but at the cost of pronounced geometric distortions [102, 103]. In multi-shot EPI, k-space is segmented across multiple echo trains, which reduces distortion and can improve spatial resolution, but is prone to subject motion artifacts between shots [102].

2.3.4 Imperfections in diffusion MRI measurements

Diffusion MRI measurements are affected by various deviations from the true underlying signal. These deviations arise from a combination of physical, hardware,

and subject-related factors, and are typically addressed during the so-called preprocessing stage of data analysis. They can be broadly grouped into random noise and systematic artifacts, the latter including effects from image sampling, magnetic field inhomogeneities, gradient imperfections, and subject motion.

Noise in diffusion MRI

The raw dMRI signal is inherently complex-valued, with independent real and imaginary channels (see Equation (2.24)). Thermal noise from the receiver coil and the conductive tissue of the subject is well described by a zero-mean Gaussian distribution with equal variance σ^2 in the real and imaginary channels, where σ denotes the noise level. However, dMRI is conventionally reconstructed as magnitude images, obtained by taking the absolute value of the complex signal. This operation transforms the Gaussian noise distribution into a Rician distribution [31]. At low SNR, the Rician distribution is positively biased, leading to a nonzero noise floor. This bias affects quantitative analysis, particularly at high b-values, where the true signal is strongly decayed and therefore approaches the noise level. While post-hoc correction via Rician noise modeling provides one approach for mitigation [32, 33], there are also methods that attempt to restore the original Gaussian-distributed complex signal before magnitude reconstruction [104–106].

Partial volume effects

In dMRI, each voxel covers a relatively large region of tissue, typically 1 mm to 3 mm isotropic in vivo. As a result, a single voxel can contain a mixture of different tissue types, for example, gray matter, white matter, and CSF (see Section 2.1). The measured signal is therefore a weighted sum of the contributions from all tissues within the voxel [107]. This phenomenon is known as the partial volume effect. It can blur tissue boundaries and obscure microstructural differences. Mitigation approaches include higher-resolution acquisitions or explicitly modeling multiple tissue contributions [108].

Gibbs ringing

Gibbs ringing is caused by truncation of high spatial frequencies in the finite k-space sampling of MRI [109, 110]. In dMRI, it manifests as oscillatory intensity patterns near sharp edges, especially at the brain–CSF interface. These oscillations vary with image orientation and b-value. Mitigation strategies include smoothing of k-space data with a window function in k-space [111] or post-processing methods such as sub-voxel shift averaging [112].

Susceptibility-induced distortions

EPI, the dominant acquisition in dMRI, is sensitive to static magnetic field inhomogeneities. These arise at tissue–air interfaces (e.g., near sinuses and ear canals), causing local variations in the effective encoding gradient. The resulting susceptibility-induced distortions appear as geometric stretching or compression along the phase-encoding (PE) direction [103]. They can be modeled and corrected based on reversed-PE acquisitions [113].

Eddy current distortions
Rapid switching of strong diffusion-encoding gradients induces eddy currents in the conducting structures of the MR scanner. These eddy currents create transient magnetic fields that act as additional gradients, leading to spatial shifts, scaling, or shearing of images [114]. The effect depends both on the magnitude and the direction of $\mathbf{G}$. It can be mitigated through dedicated eddy current distortion correction tools [115, 116].

Subject motion
Even small head motions during dMRI acquisitions can cause severe artifacts, because the diffusion weighting is both direction- and b-value–dependent. Motion between volumes leads to misalignment across diffusion directions, while motion during the acquisition of a single volume can cause local signal dropout, i.e., a severe reduction of signal intensity. Inter-volume misalignment can be corrected with rigid-body registration, and in practice, this correction is often combined with eddy current distortion correction [115, 116]. Intra-volume motion is more challenging to correct and requires dedicated slice-to-volume or model-based correction methods [117].

Gradient nonlinearity
The gradients induced by the coil deviate from perfect linearity away from the isocenter, causing spatially varying deviations in the intended gradients. Gradient nonlinearity has two main effects. First, it alters the spatial encoding relation between k-space and image space, leading to geometric distortions in the reconstructed images (objects appear stretched or compressed away from isocenter), which can be mitigated with scanner-specific corrections [118, 119]. Second, it changes the actual diffusion encoding, causing location-dependent deviations in gradient amplitudes and directions, which can bias diffusion metrics. Correction requires scanner-specific calibration and adjustment of the gradient table during processing [120].

2.3.5 Signal representations of diffusion

dMRI signals can be modeled using well-defined physical descriptors, e.g., the scalar diffusion coefficient D or the diffusion kurtosis. Such models, sometimes referred to as signal representations [121], are useful for characterizing tissue contrast but are not designed to provide direct estimates of specific microstructural features such as the axon radius.

Apparent diffusion coefficient
In the idealized case of free isotropic diffusion (see Equation (2.27)), the signal is independent of the gradient direction $\mathbf{G}$. In this situation, a single dMRI measurement suffices to estimate the diffusion coefficient D, which in biological tissue is typically referred to as the apparent diffusion coefficient (ADC).

Diffusion tensor imaging
In biological tissue, diffusion is influenced by microstructural barriers, leading to directional dependence (anisotropy). Diffusion tensor imaging (DTI) [122] applies

the GPA under the additional assumption that diffusion is Gaussian but anisotropic. This replaces the scalar diffusivity D in the free isotropic model with a symmetric second-rank tensor

$$\mathbf{D} = \begin{bmatrix} D_{xx} & D_{xy} & D_{xz} \\ D_{xy} & D_{yy} & D_{yz} \\ D_{xz} & D_{yz} & D_{zz} \end{bmatrix}, \tag{2.29}$$

where the diagonal terms represent diffusivities along the principal axes and the off-diagonal terms capture correlations between directions. Accordingly, the signal equation becomes

$$S(b, \mathbf{g}) = S_0 \exp\left(-b\, \mathbf{g}^\top \mathbf{D} \mathbf{g}\right), \tag{2.30}$$

where $\mathbf{g} = \mathbf{G}/|\mathbf{G}|$ is the unit vector along the applied gradient direction.

From $\mathbf{D}$, scalar metrics can be derived that summarize diffusion properties. By decomposing $\mathbf{D}$ into its eigenvalues $(\lambda_1, \lambda_2, \lambda_3)$ and corresponding eigenvectors, one can obtain the mean diffusivity (MD), which measures the average of the eigenvalues:

$$\mathrm{MD} = \frac{1}{3}(\lambda_1 + \lambda_2 + \lambda_3) \quad [\mu\mathrm{m}^2/\mathrm{ms}]. \tag{2.31}$$

Note that MD is essentially a rotationally invariant version of the ADC, with the eigenvalues representing the apparent diffusivities along the principal axes of $\mathbf{D}$.

The fractional anisotropy (FA) quantifies the degree of diffusion anisotropy:

$$\mathrm{FA} = \sqrt{\frac{3}{2}} \cdot \frac{\sqrt{(\lambda_1 - \mathrm{MD})^2 + (\lambda_2 - \mathrm{MD})^2 + (\lambda_3 - \mathrm{MD})^2}}{\sqrt{\lambda_1^2 + \lambda_2^2 + \lambda_3^2}}, \tag{2.32}$$

where FA values range from 0 (isotropic diffusion) to 1 (completely anisotropic). Figure 2.9 illustrates MD and FA alongside the images used for their derivation.

To estimate $\mathbf{D}$ from experimental data, one acquires a set of diffusion-weighted measurements acquired along different gradient directions. In theory, six non-collinear directions suffice to determine the six unique elements of $\mathbf{D}$. In practice, 20–30 directions are typically acquired at a common b-value (commonly $600\,\mathrm{s/mm}^2$ to $1200\,\mathrm{s/mm}^2$), along with non-diffusion-weighted ($b = 0$) images, to improve noise robustness and rotational invariance [123, 124].

Diffusion kurtosis imaging

Diffusion kurtosis imaging (DKI) [125] extends DTI to situations where diffusion deviates moderately from the GPA, i.e., beyond the second-order truncation of the cumulant expansion in Equation (2.25). Specifically, DKI retains the $\langle \phi^4 \rangle_c$ term, which captures excess kurtosis of the displacement distribution, leading to the following signal expression [93, 125]:

$$S(b, \mathbf{g}) \approx S_0 \exp[-b\,(\mathbf{g}^\top \mathbf{D}\, \mathbf{g}) + \tfrac{1}{6}\, b^2\, (\mathbf{g}^\top \mathbf{D}\, \mathbf{g})^2\, K(\mathbf{g})], \tag{2.33}$$

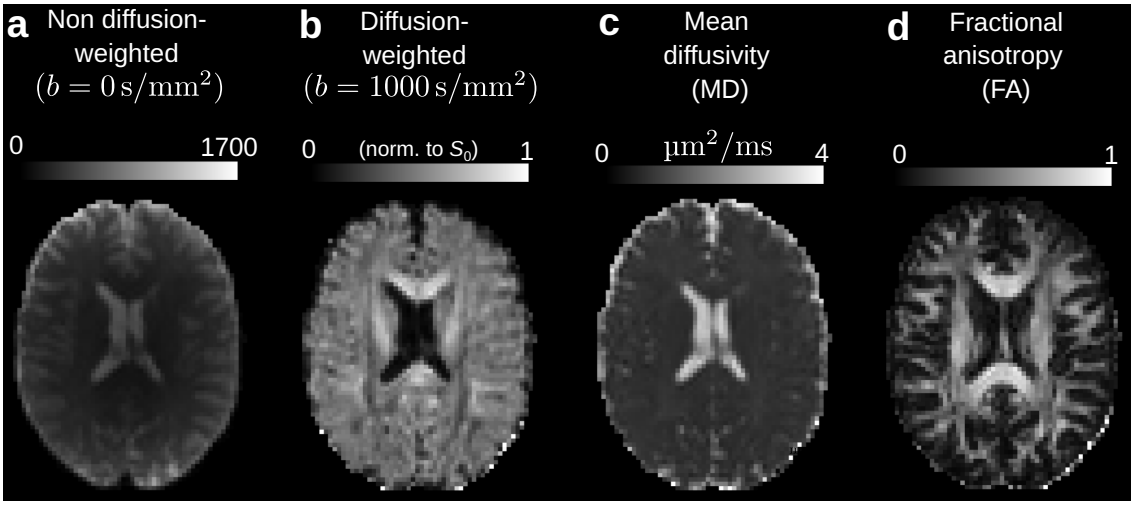

Figure 2.9: Diffusion tensor imaging. **(a-b)** Exemplary MRI images without **(a)** and with **(b)** diffusion-weighting. **(c-d)** Derived metrics from DTI: **(c)** mean diffusivity (MD) and **(d)** fractional anisotropy (FA). Metrics were computed over 30 diffusion-weighted images as in (a). All images show axial views of the brain.

where $K(\mathbf{g})$ is the apparent kurtosis along direction $\mathbf{g}$. Formally, it can be obtained by contracting the kurtosis tensor $\mathbf{W}$ with four copies of $\mathbf{g}$:

$$K(\mathbf{g}) = \sum_{i,j,k,l=1}^{3} W_{ijkl}\, g_i g_j g_k g_l, \tag{2.34}$$

where $\mathbf{W}$ is a fully symmetric rank-4 tensor with 15 independent elements [125].

In practice, DKI acquisitions typically combine two or more b-values, including $b \approx 2000\,\mathrm{s/mm^2}$ in addition to standard DTI values ($b \approx 1000\,\mathrm{s/mm^2}$), and more diffusion gradient directions $\mathbf{g}$ (commonly 30–60 in total) [126] to improve sensitivity to non-Gaussian diffusion and ensure robust fitting. In this thesis, we use DKI primarily to improve estimation of $\mathbf{D}$ and its derived metrics (see Equations (2.31) and (2.32)).

2.3.6 Modeling white matter and axons

The models in Section 2.3.5 describe diffusion signals without explicit assumptions about tissue structure. In contrast, biophysical models represent microstructure directly, thereby promising the estimation of biologically interpretable quantities. Here, we focus on biophysical models of white matter and one of their central components: axons. Unless otherwise noted, all signal expressions in this section refer to the normalized signal S/S_0, i.e., the diffusion-weighted signal relative to the non-diffusion-weighted reference signal.

2.3.6.1 Tissue models of white matter and axons

White matter is predominantly composed of fiber bundles, consisting of coherently oriented axons, which can be idealized as long, straight cylinders (see Figure 2.10a-

b). Water inside these axons (the intra-axonal space) is separated from the extra-axonal space by the axonal membrane and, in white matter, additionally by the myelin sheath; these compartments exhibit distinct diffusion characteristics (see Figure 2.10b). Because most white-matter axons are myelinated, water exchange between the intra- and extra-axonal compartments is negligible on typical diffusion time scales, so the diffusion-weighted signal can be written as a sum of non-exchanging intra-axonal (S_a) and extra-axonal (S_e) contributions [127]:

$$S(b, \mathbf{g}) = f_\mathrm{a}\, S_\mathrm{a}(b, \mathbf{g}) + f_\mathrm{e}\, S_\mathrm{e}(b, \mathbf{g}), \qquad f_\mathrm{a} + f_\mathrm{e} = 1, \tag{2.35}$$

where f_a and f_e are the T_2-weighted signal fractions of the intra-axonal and extra-axonal compartments. Assuming a distribution of fiber bundles (see Figure 2.10c-d) with fiber orientation distribution function (ODF) $\Psi(\mathbf{n})$ normalized to $\int_{|\mathbf{n}|=1} \Psi(\mathbf{n})\, d\mathbf{n} = 1$, the compartment signals are given by

$$S_i(b, \mathbf{g}) = \int_{|\mathbf{n}|=1} \Psi(\mathbf{n})\, e^{-b\left(D_\mathrm{i}^{\parallel}(\mathbf{g}\cdot\mathbf{n})^2 + D_\mathrm{i}^{\perp}(1-(\mathbf{g}\cdot\mathbf{n})^2)\right)}\, d\mathbf{n}, \qquad i \in \{\mathrm{a}, \mathrm{e}\}, \tag{2.36}$$

where the integration is over the unit sphere of fiber orientations $\mathbf{n}$. This expression assumes axially symmetric Gaussian diffusion within each compartment. In typical in vivo measurements, the parallel diffusivities $D_\mathrm{a}^{\parallel}$ and $D_\mathrm{e}^{\parallel}$ are close to free diffusion and lie around $2\,\mu\mathrm{m}^2/\mathrm{ms}$ in white matter [128]. Perpendicular diffusivities ($D_\mathrm{a}^{\perp}$ and $D_\mathrm{e}^{\perp}$) are smaller: $D_\mathrm{e}^{\perp} \approx 0.5\,\mu\mathrm{m}^2/\mathrm{ms}$ [128] and $D_\mathrm{a}^{\perp} \approx 0.02\,\mu\mathrm{m}^2/\mathrm{ms}$ [15]. In fact, $D_\mathrm{a}^{\perp}$ is so small at b-values achievable on widespread clinical scanners that it is not reliably detectable and set to zero in the standard white matter model. This approximation, commonly referred to as the axonal stick assumption [127], has been supported by experimental observations [129, 130].

2.3.6.2 Axon radius modeling

This section extends the standard model (see Section 2.3.6.1) by relaxing the axonal stick assumption $D_\mathrm{a}^{\perp} = 0$, which becomes relevant at sufficiently high b-values. In this regime, the intra-axonal perpendicular diffusivity $D_\mathrm{a}^{\perp}$ can be probed, thereby promising sensitivity to axon radius [15]. At the same time, the extra-axonal signal $S_\mathrm{e}(b, \mathbf{g})$ decays more rapidly with b than the intra-axonal contribution $S_\mathrm{a}(b, \mathbf{g})$ and can often be neglected ($b \gtrsim 6\,\mathrm{ms}/\mu\mathrm{m}^2$ in vivo [15, 19], $b \gtrsim 20\,\mathrm{ms}/\mu\mathrm{m}^2$ ex vivo [15]). To isolate the signal component sensitive to axon radius, we first remove orientation dispersion through powder-averaging, then introduce signal models for individual axons, extend these to ensembles representative of a dMRI voxel, and finally outline practical estimation approaches.

Powder-average signal at high b

To remove orientation dependence, we employ the orientation-invariant powder-averaged signal, defined as the average over all gradient directions $\mathbf{g}$ distributed on

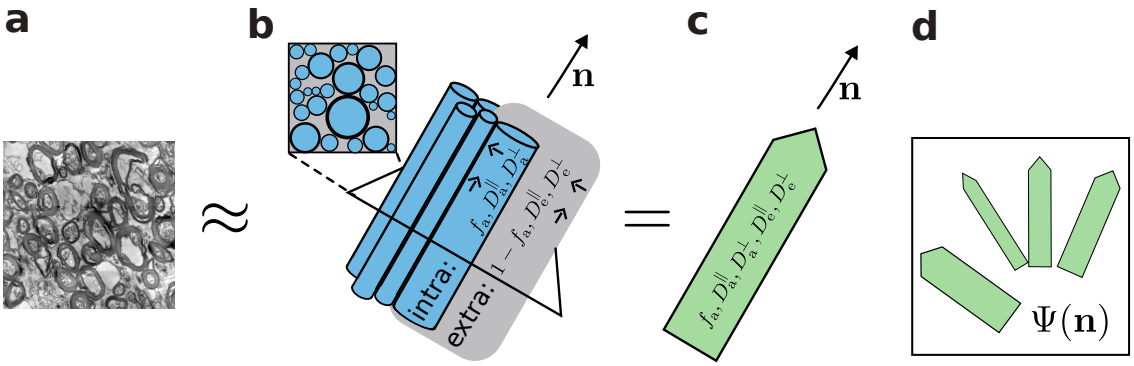

Figure 2.10: White matter tissue model. **(a)** 2D Electron microscopy (EM) image of white matter tissue, with fibers cut orthogonally to the image plane. **(b)** 3D schematic of compartmental signal contributors within a fascicle, with the inset (top left) illustrating a cross-section orthogonal to the fiber fascicle. The signal depends on the T_2-weighted intra-axonal signal fraction f_a as well as on diffusivities along ($D_\mathrm{a}^{\parallel}$, $D_\mathrm{e}^{\parallel}$) and perpendicular to ($D_\mathrm{a}^{\perp}$, $D_\mathrm{e}^{\perp}$) the fiber orientation $\mathbf{n}$. Note that we write the T_2-weighted extra-axonal signal fraction f_e as $1 - f_\mathrm{a}$ to make explicit that f_e is fixed by f_a via $f_\mathrm{a} + f_\mathrm{e} = 1$ (see Equation (2.35)). **(c)** Illustration of a fiber fascicle model alongside its parameters. **(d)** Illustration of a dMRI voxel containing multiple fiber fascicles with varying orientations $\mathbf{n}$, characterized by the fiber orientation distribution function (ODF) $\Psi(\mathbf{n})$.[a]

[a]The figure is based on Novikov et al. [48].

the unit sphere [35–37, 131]:

$$S^\circ(b) = \frac{1}{4\pi} \int_{|\mathbf{g}|=1} S(b, \mathbf{g})\, d\mathbf{g}, \tag{2.37}$$

In practice, powder-averaging can be performed by extracting the zeroth-order spherical harmonic coefficient of the signal. In the high-b regime introduced above, the intra-axonal compartment dominates the powder-averaged signal, yielding the approximation [19]:

$$S^\circ(b) \approx S_\mathrm{a}^\circ(b) \approx \underbrace{\frac{\beta}{\sqrt{b}}}_{S_\mathrm{a}^{\circ,\parallel}(b)} \cdot \underbrace{e^{-bD_\mathrm{a}^{\perp} + \mathcal{O}(b^2)}}_{S_\mathrm{a}^{\circ,\perp}(b)}, \qquad \beta = \sqrt{\frac{\pi}{4D_\mathrm{a}^{\parallel}}}\, f_\mathrm{a}, \tag{2.38}$$

where $S_\mathrm{a}^{\circ,\parallel}(b)$ and $S_\mathrm{a}^{\circ,\perp}(b)$ denote the parallel and perpendicular contributions, respectively. For $S_\mathrm{a}^{\circ,\perp}(b)$, the linear-in-$b$ term defines an apparent perpendicular diffusivity $D_\mathrm{a}^{\perp}$, consistent with the Gaussian diffusion case in Equation (2.36). In contrast, the $\mathcal{O}(b^2)$ terms capture non-Gaussian corrections arising from restricted diffusion in bounded geometries such as axons.

Perpendicular signal inside a single axon

As an illustration, we first consider the simplified case of a single cylindrical axon with radius r (see Figure 2.11a). The signal perpendicular to this cylinder ($\mathbf{g} \cdot \mathbf{n} = 0$)

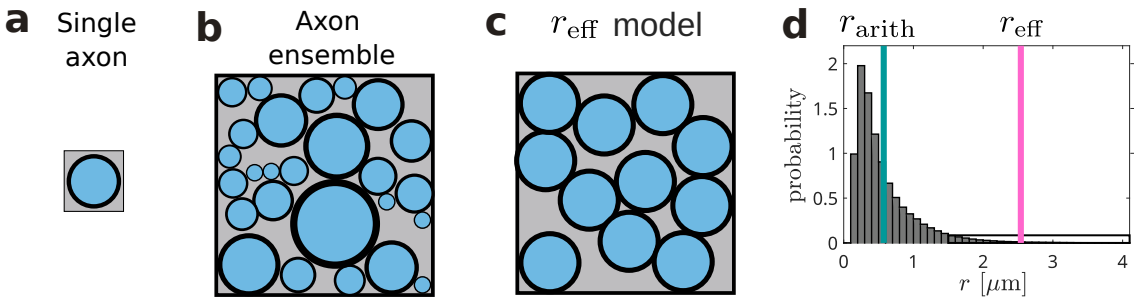

Figure 2.11: Axon radius modeling with diffusion MRI. (a–c) Illustration of tissue configurations modeled with different axon radius models: **(a)** single axon, **(b)** ensemble of axons with realistic size variation, **(c)** r_{eff} model, representing an ensemble of axons with common radius r_{eff}. **(d)** Exemplary axon radius histogram from a light microscopy (LM) section, with the effective radius r_{eff} (magenta, see Equation (2.47)) and arithmetic mean radius r_{arith} (green, see Equation (2.48)) indicated.

can be expressed as:

$$\ln S_{\text{a}}^{\circ,\perp}(b) = \ln S_{\text{cyl}}^{\perp}(b, r) = \ln S_{\text{cyl}}(b, \mathbf{g}, \mathbf{n}, r)\big|_{\mathbf{g}\cdot\mathbf{n}=0}, \tag{2.39}$$

where

$$\ln S_{\text{cyl}}(b, \mathbf{g}, \mathbf{n}, r) = -(1 - (\mathbf{g}\cdot\mathbf{n})^2)\, b\, D_{\text{a}}^{\perp}(r) + \mathcal{O}(b^2). \tag{2.40}$$

The higher-order $\mathcal{O}(b^2)$ terms lack a closed-form solution for finite δ. Furthermore, $D_{\text{a}}^{\perp}(r)$ is in general time-dependent [24], since the restricted diffusion depends on the diffusion encoding timings (δ, Δ). Here, we assume fixed (δ, Δ), so that $D_{\text{a}}^{\perp}(r)$ can be treated as constant. Practical approximations to Equation (2.40) are usually based on the GPA, for which Van Gelderen et al. [97] derived

$$\begin{aligned}\ln S_{\text{cyl,GPA}}^{\perp}(b, r) &= -\, bD_{\text{a}}^{\perp}(r) \\ &\approx -\frac{2\gamma^2 g^2 r^4}{D_0} \sum_{m=1}^{\infty} \frac{t_c}{\alpha_m^6(\alpha_m^2 - 1)} \\ &\quad \cdot \left[2\alpha_m^2 \frac{\delta}{t_c} - 2 + 2e^{-\alpha_m^2 \frac{\delta}{t_c}} + 2e^{-\alpha_m^2 \frac{\Delta}{t_c}} - e^{-2\alpha_m^2 \frac{\Delta-\delta}{t_c}} - e^{-2\alpha_m^2 \frac{\Delta+\delta}{t_c}}\right],\end{aligned} \tag{2.41}$$

where the b-dependence is captured implicitly through g, δ, and Δ; $t_c = r^2/D_0$ is the correlation time; D_0 is the intrinsic axoplasmic diffusivity; and α_m is the m-th root of $\mathrm{d}J_1(\alpha)/\mathrm{d}\alpha = 0$, with J_1 the Bessel function of the first kind.

In the wide-pulse approximation (WPA), $\Delta > \delta \gg t_c$ [95], the expression in Equation (2.41) simplifies because the dependence on Δ can be neglected. In this regime, the signal reduces to

$$\ln S_{\text{cyl,WPA}}^{\perp}(b, r) = -\kappa\, r^4, \qquad \kappa = \frac{7}{48}\frac{g^2\gamma^2\delta}{D_0}. \tag{2.42}$$

Perpendicular signal of an axon ensemble

In a dMRI voxel, the signal reflects an ensemble of many axons with radii distributed according to $H(r)$ (see Figure 2.11b). Accounting for the contribution of all axons, the perpendicular signal can be expressed as a volume-weighted average [132]:

$$S_{\mathrm{a}}^{\circ,\perp}(b) = \frac{\int_0^\infty H(r)\, r^2\, S_{\mathrm{cyl}}^{\perp}(b,r)\, dr}{\int_0^\infty H(r)\, r^2\, dr}. \tag{2.43}$$

Note that the expression assumes a common cylinder length L across axons; under this assumption, π and L cancel, so that the r^2 term encodes the volume weighting.

Effective axon radius

Equation (2.43) can be further reduced to a single scalar metric related to $H(r)$ by substituting the WPA signal Equation (2.42) and expanding in a Taylor series:

$$S_{\mathrm{a}}^{\circ,\perp}(b) \approx \frac{\int_0^\infty H(r) r^2 e^{-\kappa r^4}\ dr}{\int_0^\infty H(r) r^2\ dr} \tag{2.44}$$

$$\approx 1 - \kappa\, \frac{\langle r^6 \rangle}{\langle r^2 \rangle} \tag{2.45}$$

$$\approx e^{-\kappa r_{\mathrm{eff}}^4}, \tag{2.46}$$

where

$$r_{\mathrm{eff}} = \sqrt[4]{\frac{\langle r^6 \rangle}{\langle r^2 \rangle}} \tag{2.47}$$

is referred to as the effective axon radius. Conceptually, r_{eff} is the radius of a hypothetical ensemble of axons with identical radii producing the same dMRI signal as the actual heterogeneous axon population with radius distribution $H(r)$ (see Figure 2.11c). Importantly, r_{eff} is dominated by contributions from the largest axons—the tail of the right-skewed radius distribution $H(r)$—in contrast to the arithmetic mean radius

$$r_{\mathrm{arith}} = \langle r \rangle, \tag{2.48}$$

which is more sensitive to the bulk of $H(r)$ (see Figure 2.11d).

Practical estimation

Equating $e^{-bD_{\mathrm{a}}^{\perp}} \approx e^{-\kappa r_{\mathrm{eff}}^4}$ from Equations (2.38) and (2.46), one can express r_{eff} in terms of dMRI protocol parameters and diffusivities:

$$r_{\mathrm{eff}} \approx \sqrt[4]{\frac{48}{7}\, \delta\Big(\Delta - \frac{\delta}{3}\Big)\, D_{\mathrm{a}}^{\perp} D_0}. \tag{2.49}$$

In practice, given multi-b measurements of $S^{\circ}(b)$, one can jointly estimate r_{eff} and β via non-linear fitting [133]. For an acquisition with two b-values (b_{min} and b_{max}),

$D_{\mathrm{a}}^{\perp}$ can be obtained directly as

$$D_{\mathrm{a}}^{\perp} = \frac{\log\left(\frac{S^{\circ}(b_{\min})}{S^{\circ}(b_{\max})}\sqrt{\frac{b_{\min}}{b_{\max}}}\right)}{b_{\max} - b_{\min}}, \tag{2.50}$$

and subsequently used to compute r_{eff} [20].

2.3.6.3 Immobile water in ex vivo tissue

In ex vivo tissue, fixation often leads to an additional signal contribution from water trapped in compartments with extremely restricted mobility [13, 22]. This signal fraction, referred to as the immobile water fraction f_{im}, is effectively independent of b and gradient direction $\mathbf{g}$.

In the standard white matter signal model Equation (2.35), the presence of immobile water can be accounted for by adding a constant term to the total signal:

$$S(b, \mathbf{g}) = f_{\mathrm{a}}\, S_{\mathrm{a}}(b, \mathbf{g}) + f_{\mathrm{e}}\, S_{\mathrm{e}}(b, \mathbf{g}) + f_{\mathrm{im}}, \qquad f_{\mathrm{a}} + f_{\mathrm{e}} + f_{\mathrm{im}} = 1. \tag{2.51}$$

Because f_{im} is independent of b and $\mathbf{g}$, its presence biases model fitting if unaccounted for, particularly in the high-b regime of r_{eff} measurements where other compartments are strongly attenuated [15].

Chapter 3

A histological reference for MRI-based axon radius mapping

This chapter is primarily based on Mordhorst et al. [46], with additional material from Mordhorst et al. [47].

3.1 Introduction

To ensure that dMRI-based microstructure models – such as those used to estimate r_{eff} – accurately reflect tissue properties, they must be validated against a reference from ex vivo tissue, typically generated using microscopy imaging [12–15, 37, 41, 134–141]. Unlike dMRI, which infers microstructure indirectly from signal patterns at the millimeter scale, microscopy provides direct visualization of individual micrometer-thin axons, making it a natural reference for studying the axon radius distribution and its derivatives, such as r_{eff}. For r_{eff} specifically, the disproportionate contribution of large axons implies that a suitable histological reference must robustly capture the tail of the axon radius distribution [15, 17, 18, 38]. This tail, which reflects the statistically rare occurrence of large axons, can only be reliably sampled in large ROIs – ideally matching the size of dMRI voxels. Moreover, to evaluate whether dMRI captures meaningful anatomical variation in microstructure, histological validation must include broad spatial sampling across anatomically diverse ROIs.

Across species, the majority of validation efforts comparing dMRI-based axon radius estimates against histological values [12, 13, 15, 20, 38–42, 105, 142–146] have relied on 2D histology [4, 5, 12, 15, 17, 38, 40, 44, 45, 142, 145, 147], attempting to sample the local axon radius distribution from a single 2D cross-section orthogonal to the presumed orientation of the axon bundle. This design assumes perfectly cylindrical, parallel axons – a condition most closely satisfied in the corpus callosum, making it a prototypical white matter region for validating dMRI-based axon radius models and studying axon radius distributions. However, in humans, existing 2D datasets [4, 17, 38, 44, 45] typically include only on the order of 1,000 axons – unlikely to be representative of human in vivo dMRI voxels [12, 15, 38, 40], which contain roughly three orders of magnitude more axons. As a result, estimates of

r_{eff} from such data are prone to strong statistical fluctuations [15, 38]. In addition, they typically sample only a handful of ROIs—at most 11 in total [38]—limiting the ability to assess whether dMRI truly reflects underlying microstructure, e.g., through quantitative spatial correlations.

Recently, 3D histology has emerged as a complementary approach to 2D techniques, revealing complex axonal morphology such as undulations, branching, and radius variations [23, 26, 148, 149]. While 3D histology uniquely enables sampling along individual axons, it does not address the sampling limitations of 2D datasets across axons. In fact, existing 3D datasets typically include fewer ROIs and often capture fewer axons overall [23, 26], with the notable exception of a dataset comprising 100,000 axons—but sampled within a single ROI of superficial white matter, not the corpus callosum [148, 149]. As a result, these datasets have so far been used primarily to study the effects of morphological complexity on dMRI signal formation in Monte Carlo simulations [25–28, 38, 150], rather than for experimental validation via direct dMRI-histology comparison.

One promising candidate to address the sampling limitations across axons is to use large-scale 2D light microscopy (LM). While LM cannot resolve the smallest axons (minimum-resolvable radius $\sim 0.3\,\mu\text{m}$) as accurately as 2D electron microscopy (EM) [17, 44, 45], it enables imaging of much larger ROIs. This could enable a more robust representation of the large-axon tail of the axon radius distribution—critical for r_{eff}—than existing histology data [4, 17, 38, 44, 45]. Moreover, LM allows acquisition of a larger number of ROIs because it is significantly faster, cheaper, and technically less demanding than both 2D EM [17, 44, 45] and 3D histology [23, 26, 148, 149]. However, unlike traditional 2D EM datasets—where axon segmentation was performed manually on a manageable number of axons [17, 44, 45]—the data volume generated by LM necessitates automated segmentation, now commonly addressed via deep learning approaches in both 2D and 3D histology workflows [25, 67, 83, 149, 151–156].

In this chapter, we establish and apply a deep learning-based method for segmenting LM data to generate a histological reference for r_{eff}. We first train and test the method using LM and EM data from four human white matter tissue samples. We show that the method reliably segments the majority of axons and, importantly, enables more accurate and precise reference data for r_{eff} than existing histological datasets. We also evaluate its suitability for estimating the arithmetic mean radius (r_{arith}, see Equation (2.48) and Figure 2.11), a more intuitive measure of the axon radius distribution, and find that r_{arith} is more susceptible to LM resolution limits and staining-related intensity variation. Finally, we apply the method to two additional human corpus callosum samples with dense spatial sampling to generate a candidate histological reference dataset suitable for validating r_{eff} in dMRI.

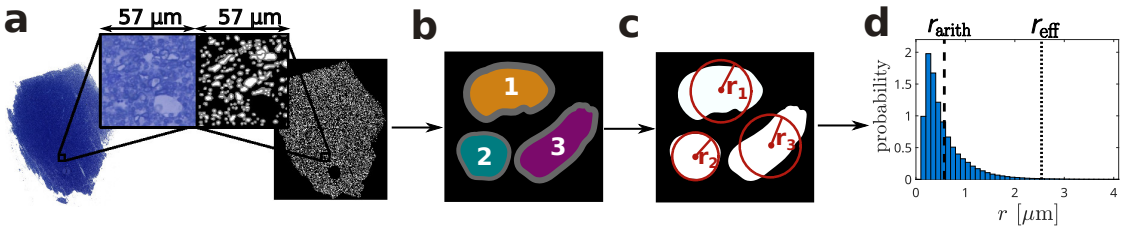

Figure 3.1: Axon radius estimation pipeline. **(a)** Pixel-wise classifications of light microscopy (LM) images as axon (white), myelin (gray), or background (black), obtained using a convolutional neural network (CNN) for semantic segmentation. The CNN was applied in a sliding window manner with patches spanning 57 µm × 57 µm. **(b)** Identified axon instances, one per color. **(c)** Radii of axon instances, estimated as radii of circles with equivalent area. **(d)** Resulting axon radius distribution, with r_{eff} and r_{arith} annotated.

3.2 Results

We implemented and evaluated a pipeline to extract axon radius distributions and their summary statistics, r_{eff} and r_{arith}, from LM images (see Figure 3.1). The pipeline combines a convolutional neural network (CNN)-based segmentation model [75] (see Figure 3.1a) with post-processing steps for axon instance identification and radius estimation (see Figure 3.1b–d). While the training procedure is described in Section 8.3, this section focuses on evaluating the optimized pipeline.

3.2.1 Segmentation performance

We first evaluated segmentation performance on 30 small LM subsections, using manual annotations as a reference (see Figure 8.4 in *Materials and methods* for an illustration). To this end, we assessed both image-level metrics, which reflect pixel-wise agreement across the full field-of-view, and per-axon metrics, which evaluate the detection and segmentation of individual axon instances.

Segmentation metrics are consistent with previous methods
At the image level (see Table 3.1), metrics are comparable to those reported by Zaimi et al. [151], who also perform axon segmentation on 2D histological sections. However, a direct comparison is complicated by differences in tissue type, staining protocol, imaging modality, and resolution between datasets.

Small axons appear hard to detect and segment
The lower recall relative to precision (see Table 3.1) indicates a tendency to miss axon pixels, which may lead to underestimation of axon radii and, consequently, of r_{eff} and r_{arith}. This bias is also evident at the per-axon level (Figure 3.2a), where false negatives outnumber false positives, particularly among small axons ($r \lesssim 1\,\mu\text{m}$). The resulting underrepresentation of small axons may further contribute to underestimation of r_{eff} and r_{arith}. Even when detected, small axons are segmented less accurately, as reflected by lower Dice scores (see Figure 3.2b), likely because axons represented by few pixels are more sensitive to pixel errors.

Table 3.1: Image-level segmentation metrics. The table presents segmentation metrics (see Equations (2.9) to (2.12)), evaluated by comparing outputs from our pipeline against manual annotations on 30 small LM subsections (see Figure 8.4 in *Materials and methods* for an illustration).

Metric	Value
Balanced accuracy	0.85
Dice	0.77
Precision	0.82
Recall	0.74

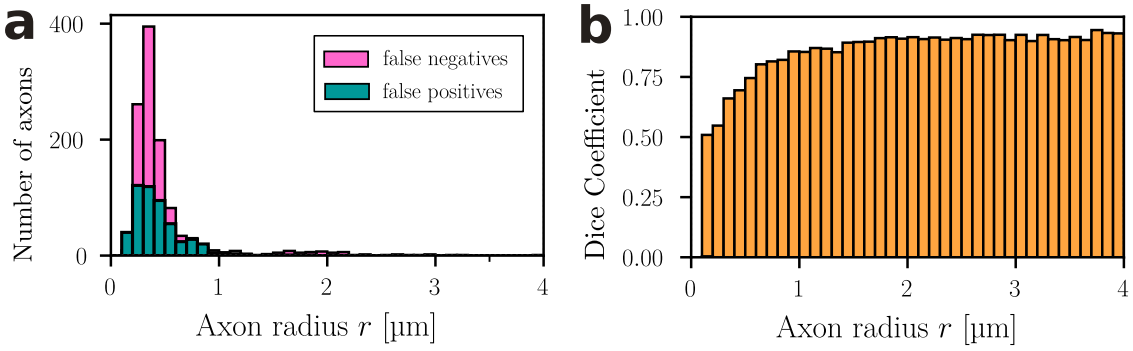

Figure 3.2: Per-axon segmentation metrics. **(a)** Number of false negative and false positive axons as a function of axon radius. **(b)** Dice coefficient as a function of axon radius. All bars show mean values per axon radius bin (bin width: 0.1 µm). Metrics were evaluated by comparing outputs from our pipeline against manual annotations on 30 small light microscopy (LM) subsections (see Figure 8.4 in *Materials and methods* for an illustration).

3.2.2 Axon radius estimates at MRI scale

To assess the ability of our method to represent r_{eff} and r_{arith} at a scale relevant for dMRI, we evaluated both metrics in LM subsections spanning the spatial scale of ex vivo dMRI voxels used in this thesis (field-of-view: 350 µm × 350 µm). We derived reference values by evaluating axon radius distributions obtained via manual axon annotation in the LM subsections and spatially matched EM sections. For r_{arith}, we used the EM-derived distribution alone. For r_{eff}, we constructed a hybrid reference by combining the EM-based bulk of the distribution (defined as $r < 1.6\,\mu\text{m}$) with the tail sampled from LM (defined as $r \geq 1.6\,\mu\text{m}$). See Figure 8.5 in *Materials and methods* for an illustration of the evaluation approach. Figure 3.3a–b shows the resulting comparisons of LM-based estimates against these reference values.

An accurate reference for r_{eff}

For r_{eff} (see Figure 3.3a), LM-based estimates remain close to the line of unity, indicating good agreement with reference values. This visual alignment is supported by quantitative measures, with low bias and a low coefficient of variation confirming high accuracy and precision.

Reduced accuracy and precision of r_{arith}

The estimates of r_{arith} (see Figure 3.3b) exhibit only moderate agreement with reference values, showing both systematic overestimation and substantial variability. The overestimation likely reflects the resolution limit of LM, which impairs the detection of small axons. The observed variability may partly stem from slight spatial mismatches between the LM subsections evaluated and the corresponding EM subsections used as reference.

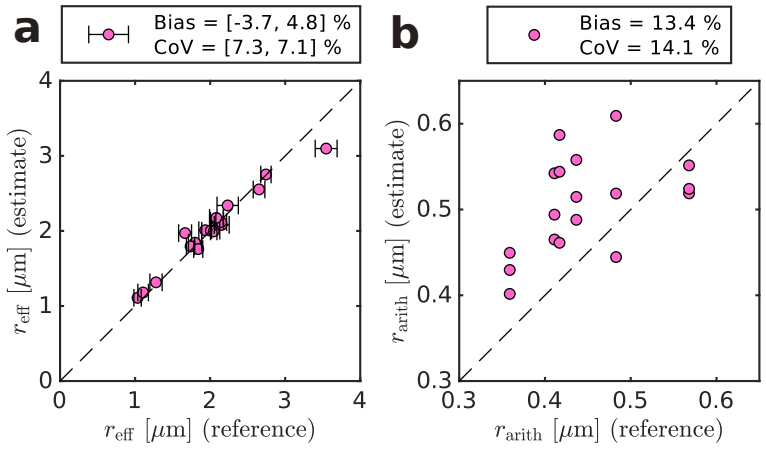

Figure 3.3: Validation of r_{eff} and r_{arith} estimates at MRI scale. (a) Comparison of light microscopy (LM)-based r_{eff} estimates against reference values from manual annotations. Each marker represents one LM subsection, while the dashed line indicates theoretical perfect agreement. Reference values are shown as a bounded range, reflecting uncertainty in combining EM-based estimates for small axons ($r < 1.6\,\mu\text{m}$) and LM-based estimates for large axons ($r \geq 1.6\,\mu\text{m}$). See Figure 8.5 in *Materials and methods* for an illustration of the evaluation approach. The legend reports bias (see Equation (8.3)), and coefficient of variation (CoV, see Equation (8.4)), each calculated for the lower and upper bounds of the reference. **(b)** Comparison of LM-based r_{arith} estimates against EM-derived reference values for the same subsections, using the same metrics and definitions as in (a), but with fixed reference values.

3.2.3 Staining as a confounder

We assessed the impact of local image intensity variation, e.g., due to staining heterogeneity, on r_{eff} and r_{arith}. To this end, we evaluated both metrics across entire LM ROIs and computed spatial correlations with image intensity, resampled on a 350 µm grid. Figure 3.4a-c show spatial maps of image intensity, r_{eff} and r_{arith} for an exemplary ROI, whereas Figure 3.4d–e display spatial correlations between image intensity and the estimated values of r_{eff} and r_{arith} across multiple ROIs.

r_{eff} shows robustness to image intensity variation

r_{eff} does not visibly follow the spatial pattern of image intensity in most regions (Figure 3.4a-b). This observation is supported by quantitative analysis (Figure 3.4d), which reveals no significant correlation between r_{eff} and image intensity.

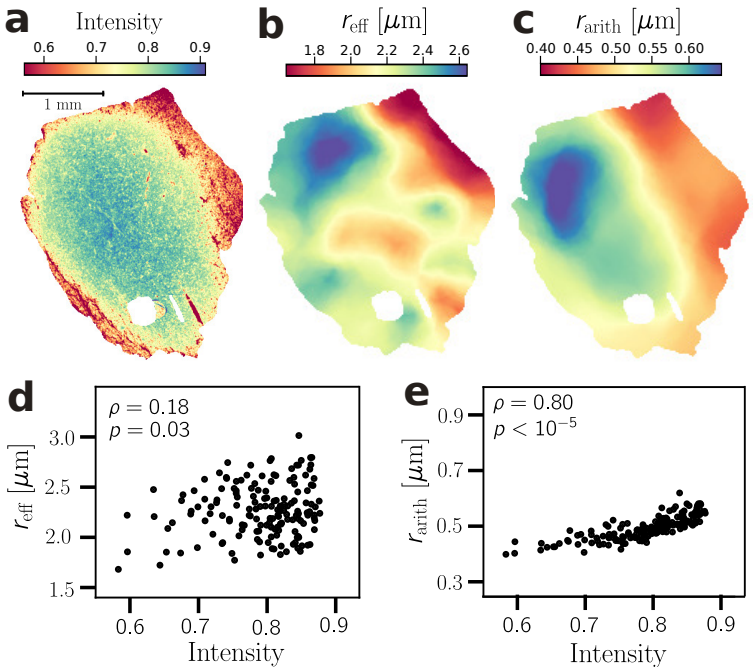

Figure 3.4: Impact of image intensity variation on r_{eff} and r_{arith}. **(a-c)** Parameter maps for an exemplary light microscopy (LM) ROI: **(a)** image intensity, **(b)** r_{eff} and **(c)** r_{arith}. Maps in (b-c) were spatially smoothed for visualization. **(d)** Correlation between r_{eff} and image intensity. Each marker represents a 350 µm × 350 µm subsection (see scale bar in (a) for reference), sampled across four histology ROIs selected to have similar r_{eff} magnitudes. **(e)** Correlation between r_{arith} and image intensity, following the definitions in (d).

r_{arith} appears sensitive to staining intensity

In contrast, r_{arith} closely mirrors spatial variation in image intensity (Figure 3.4a,c). In the quantitative analysis (Figure 3.4e), this trend is confirmed by a strong and significant correlation. In a visual inspection of the LM images and segmentation masks, we found that elevated image intensity hinders the detection of small axons, effectively modulating the resolution limit and thereby introducing a dependence of r_{arith} on image intensity.

3.2.4 Establishing a reference for MRI validation

With the proposed method validated, we applied it to two additional human corpus callosum tissue samples with denser spatial sampling, comprising 35 ROIs (see CC-02 and CC-03 in Figure 1.1f). For each ROI, we acquired one LM image, extracted empirical axon radius distributions, and computed both r_{eff} and r_{arith}. In the following, we compare the sampling statistics of our dataset to existing 2D histology datasets of the human corpus callosum [4, 17, 38, 45], and quantify the resulting improvements in the accuracy and precision of r_{eff} and r_{arith}.

Improved spatial coverage and axon sampling over existing datasets

Figure 3.5 presents a comparison of sampling characteristics between our dataset and previously published histological datasets of the human corpus callosum [4, 17, 38,

45]. Compared to prior work, our dataset offers denser spatial coverage by including a larger number of ROIs (see Figure 3.5a), as well as more extensive sampling within each ROI, capturing axon ensembles that span areas comparable to in vivo dMRI voxel cross-sections used in this thesis (see Figure 3.5b).

Tail sampling affects r_{eff} more strongly than r_{arith}

Figure 3.6a-b illustrates that LM ROI sizes enable smoother sampling of the tail of the axon radius distribution than ROI sizes used by Aboitiz et al. [17], which would result in occasional spikes. While the axon radius distributions exhibit strongly different r_{eff} values, r_{arith} seems largely unaffected, suggesting that r_{eff} is more sensitive to ROI size than r_{arith}.

dMRI-scale ROIs enable improved bias and precision in r_{eff}

The influence of ROI size on r_{eff} is illustrated in Figure 3.6c, which shows how r_{eff} values vary with repeated subsampling at different ROI sizes. Smaller ROIs tend to underestimate r_{eff} and show a greater chance of outlier overestimations (as illustrated in Figure 3.6b), reflecting reduced accuracy and precision. This trend is quantified across all ROIs in Figure 3.6d-e. As ROI size increases, both accuracy (in terms of bias) and precision (as coefficient of variation) improve, though accuracy improves more steeply. For ROI sizes used in prior histology datasets [4, 17, 38, 45], the expected bias ranges from 4 to 12 %, while the coefficient of variation ranges from 14 to 21 %.

r_{arith} has lower sample size requirements than r_{eff}

Applying the same subsampling analysis to r_{arith} (Figure 3.6f-h) reveals a striking difference from r_{eff}. Unlike r_{eff}, r_{arith} remains largely unbiased across all ROI sizes, and its precision is consistently higher. Even at ROI sizes typical of existing histology datasets [4, 17, 38, 45], the coefficient of variation (CoV) remains below 5 %, suggesting that these datasets provide reliable reference values for r_{arith}.

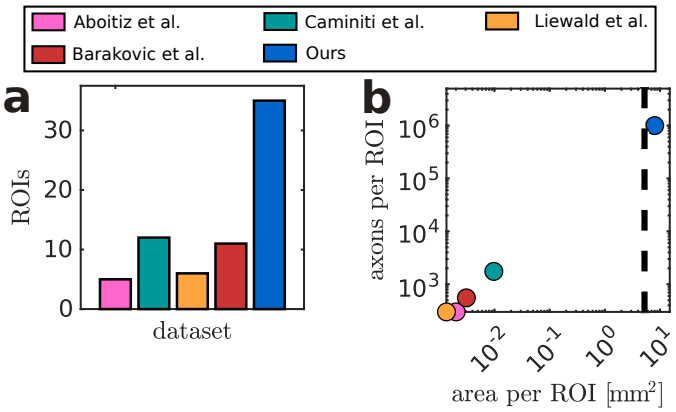

Figure 3.5: Comparison of human corpus callosum histology datasets. **(a)** Total number of ROIs per dataset [4, 17, 38, 45] **(b)** Mean sampling area and axon count per ROI (double-logarithmic scale; area for Barakovic et al. [38] estimated via linear fit of reported axon counts versus area from remaining datasets [4, 17, 45]). The dashed line indicates the cross-sectional area of the in vivo dMRI voxels (2.5 mm × 2.5 mm) used in this thesis. The ROIs referenced here for our dataset include all histological ROIs in Figure 1.1f.

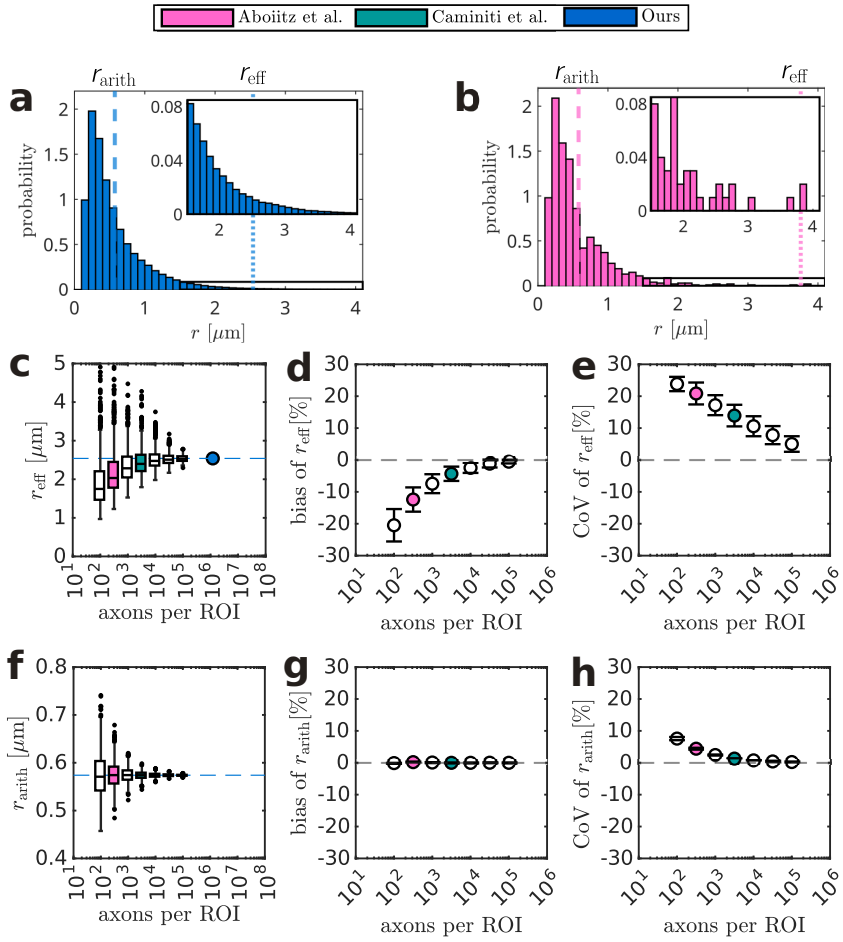

Figure 3.6: Accuracy and precision gains through MRI-scale samples. **(a-b)** Axon radius distribution for **(a)** a light microscopy (LM) ROI and **(b)** a random subsample of the distribution in (a), including 10^3 axons, mimicking a ROI as presented by Aboitiz et al. [17]. Vertical dotted lines denote r_{eff}, whereas dashed lines denote r_{arith}; insets highlight tails of axon radius distributions. **(c)** Sampling distribution of r_{eff} as a function of ROI size (axon count) for the ROI in (a). The blue marker and dashed line represent r_{eff} computed from all axons within the ROI, while boxplots show simulated sampling distributions for smaller ROI sizes, indicating the median (line), interquartile range (IQR, box), whiskers (1.5 IQR), and outliers (dots). Box colors reflect datasets, categorized by ROI size (see legend). **(d-e)** Bias (see Equation (8.3)) and coefficient of variation (CoV, see Equation (8.4)) as a function of the ROI size based on sampling distributions as shown in (c). Markers show mean ± standard deviation across ROIs. **(f-h)** Sampling distribution, bias, and CoV for r_{arith} as a function of ROI size, replicating the analysis for r_{eff} in (c-e).

3.3 Discussion

We investigated the potential of deep learning-based segmentation on large-scale 2D light microscopy (LM) data to generate reference data for r_{eff} in the human brain. Our method yields estimates of r_{eff} with high accuracy and precision – achieving levels that are inherently difficult to achieve with the smaller ROI sizes of existing datasets. We applied this approach to two human corpus callosum specimens, generating a candidate reference dataset for future validation studies of r_{eff}, with dense spatial coverage enabling assessment of meaningful microstructural variation. However, the method is less suitable for estimating r_{arith}, as values are both biased and imprecise due to the limited resolution of LM and the confounding influence of staining-related image intensity.

A suitable reference for r_{eff}

Our method demonstrates strong agreement in r_{eff} with reference values derived from manual annotations, as quantified by precision (coefficient of variation: 8 %) and bias (underestimation of 5 %) on our test dataset. While we cannot directly assess these metrics in existing human corpus callosum datasets [4, 17, 38, 45], our subsampling analysis suggests that their limited ROI sizes inherently introduce at least similar bias (4 to 12 %) and lower precision (coefficient of variation: 14 to 21 %). This effect is likely underestimated in our subsampling analysis, which does not account for spatial heterogeneity. Notably, the underestimation in existing histology data also has broader implications: r_{eff} in the human brain may be systematically larger than previously assumed, suggesting that dMRI-based r_{eff} mapping may be less constrained by the resolution limit of dMRI for small axons [157] than previously thought.

Towards more comprehensive dMRI validation of r_{eff}

Our dataset enables validation strategies that were previously infeasible due to limited histological sampling. Its dense spatial coverage across ROIs allows for quantitative spatial correlation analyses, moving beyond the qualitative comparisons that have dominated the literature [12, 13, 15, 20, 38–42, 105, 142–145] due to restricted histological data [4, 5, 12, 15, 17, 23, 26, 38, 40, 44, 45, 142, 145, 147–149], particularly in humans [4, 17, 38, 44, 45, 148, 149].

In addition, the dMRI-scale axon ensembles captured in our dataset open new opportunities for simulation studies. Just as recent work has highlighted the influence of realistic 3D axonal morphology [23–28, 38, 150], simulations based on our data may reveal how large-scale across-axon radius distributions shape the dMRI signal.

Our framework can also be used to validate alternative dMRI-based axon radius metrics. The definition of r_{eff} used here relies on assumptions about the dMRI protocol, namely the wide-pulse approximation (WPA, see Equation (2.42)), which assumes long diffusion gradient pulses [14–16]. An alternative definition applies in the narrow-pulse limit with very short diffusion gradient pulses: $r_{\text{eff,narrow-pulse}} = \sqrt{\langle r^4 \rangle / \langle r^2 \rangle}$ [14, 16]. As shown in Figure B.1, estimates of $r_{\text{eff,narrow-pulse}}$ from our pipeline achieve accuracy and precision comparable to those of r_{eff} under the WPA.

Light microscopy is unsuitable for estimating r_{arith}

Our results show that LM is unsuitable for representing r_{arith}, yielding estimates that are both biased and imprecise. The bias arises from LM's limited resolution, which prevents detection of small axons – a critical component for accurately computing r_{arith}. The imprecision likely reflects staining-driven image intensity variation across LM images, which effectively modulates the resolution limit and distorts estimated r_{arith} values, risking that imaging artifacts are mistaken for true microstructural differences. However, using LM to reference r_{arith} would also be unnecessary, as typical EM ROI sizes ($\sim$ 1000 axons [4, 17, 38, 45]) appear sufficient to estimate r_{arith} with negligible bias and reasonable precision – at least when spatial variation is factored out, as in our subsampling analysis.

Limitations and future directions

While we demonstrated the applicability of our method to the human corpus callosum, its generalizability to other brain regions remains to be evaluated in future work.

We did not benchmark existing 2D axon segmentation pipelines [151] on our data. While such comparisons may be informative, they are unlikely to affect our main conclusions. These conclusions are driven by dataset properties—namely, ROI size, imaging resolution, and staining variability—rather than the specific segmentation method applied.

Measuring axon radii from 2D histology can introduce bias when axons intersect the imaging plane obliquely [23, 26, 158]. The circular equivalent method used here may overestimate radii in such cases, whereas an alternative based on the minor axis of a fitted ellipse may underestimate true radii by ignoring genuine eccentricity. While we do not attempt to resolve this methodological debate, our method yields similar r_{eff} accuracy and precision when using the elliptical minor axis approximation (see Figure B.2).

More critically, 2D histology cannot capture along-axon morphological features revealed by 3D histology [23, 26, 148, 149], such as undulations and radius fluctuations. However, 3D histology insights also suggest that ensemble-level axon radius distributions appear relatively stable within local fiber populations [26], indicating that 2D histology may provide representative sampling of axon radius distributions. Still, 3D-informed simulations have shown that such complex axonal morphology can also affect the dMRI signal [25–28, 150]. Ultimately, the sensitivity of dMRI to r_{eff} despite these effects—and the adequacy of 2D histology as a reference—has to be tested through experimental validation.

Beyond the scope of dMRI, our data could support the development and validation of parametric models of axon radius distributions [12, 18, 159, 160]. Moreover, once validated beyond the corpus callosum, our method could facilitate the construction of a whole-brain atlas of large axons.

Conclusion

We demonstrated that deep learning-based segmentation of 2D light microscopy data provides a viable approach for generating accurate and precise reference data for r_{eff} in the human corpus callosum. Applied to two specimens with dense spatial sampling,

our method yields a reference dataset specifically suited for future validation of dMRI-based r_{eff} mapping. In the following chapters, this dataset is used both for quantitative spatial correlation analyses between dMRI and histology (see Chapter 4) and for histologically informed simulations of dMRI signals, leveraging realistic axon radius distributions from large axon ensembles at the scale relevant for dMRI resolution (see Chapters 5 and 6).

Chapter 4

Experimental validation of MRI-based axon radius mapping

This chapter is based on Mordhorst et al. [47], with adaptations and extensions for this thesis.

4.1 Introduction

Measuring axon radii with dMRI has been a longstanding goal in the field. Yet, despite decades of modeling efforts [12, 13, 15, 16, 20, 38, 43, 161, 162], robust measurement has remained challenging. Robust measurement, particularly in the presence of noise, is fundamentally limited by the inherently low sensitivity of dMRI to micrometer-thin axons [14, 15, 42, 157]. In vivo, this sensitivity appears achievable only on advanced research scanners with ultra-strong diffusion gradient amplitudes of 300 mT/m [6, 15, 20, 39, 105, 146, 163].

Even when sensitivity is sufficient, achieving specificity remains challenging due to competing signal contributions that can obscure axon radius effects. These include effects of unmodeled intra-axonal features [23–28] such as along-axon radius variation and undulations [23, 26, 148, 149] – deviations from the perfect cylinder assumption underlying dMRI-based axon radius models, including the model used for r_{eff}. Additional confounds arise from axonal dispersion [29, 30], exchange between intra- and extra-axonal compartments [19, 164, 165], axonal surface relaxation effects [38], Rician noise bias [31], and signal contributions from non-axonal tissue compartments such as extra-axonal water [15, 19, 20], somas [21], and immobile water [22]. While advances in modeling [20, 32–38] and experimental design [6, 15] have been proposed to mitigate these effects, it remains unclear whether sensitivity to axon radii persists under experimental conditions.

These challenges have also shaped the scope of histological validation. For much of the field's history, dMRI-based axon radius estimates were severely overestimated, and histology primarily served to resolve the debate over whether dMRI is sensitive to axon radii in the biologically plausible range. Despite these challenges, some consistent results have been established over the years. In particular, the corpus

callosum has often served as a prototypical structure for such investigations, with spatial patterns in axon radii commonly reported along its anterior–posterior axis. In rodents, a relatively consistent low–high–low profile has emerged and shows correspondence with histology [15, 40]. Related patterns have also been described in humans [4, 6, 17, 20, 38, 41–43] and nonhuman primates [4, 147], although differences in anatomical definitions, ROI placement, and analysis methods complicate direct comparisons between these studies. Still, this qualitative evidence suggests that axon radius distributions are spatially organized and that dMRI may be sensitive to these anatomical variations. However, quantitative validation of such spatial patterns—particularly in humans—remains lacking, largely due to the limited spatial coverage of existing histological datasets, as outlined in Chapter 3.

In this chapter, we assess the validity of dMRI-based axon radius estimation—specifically r_{eff}—using state-of-the-art in vivo and ex vivo protocols [6, 15]. Building on the densely sampled light microscopy (LM) dataset introduced in Chapter 3, we perform the first direct experimental test of whether dMRI-derived r_{eff} captures meaningful anatomical variation in the human brain. At the group level, in vivo r_{eff} estimates show significant spatial correlations with histology, providing the first quantitative evidence of dMRI sensitivity to r_{eff}. In contrast, no such correlation is observed in ex vivo dMRI acquired from the same tissue used for histological analysis. By mirroring these experiments with simulations grounded in our histology data, we show that the lack of correlation ex vivo is explained by a model-inherent reduction in sensitivity, which appears less pronounced in vivo.

4.2 Results

4.2.1 Spatial patterns in histology

To enable spatial comparison across modalities, we mapped the histology-based r_{eff} values from the dataset generated in Chapter 3 to the Montreal Neurological Institute (MNI) space [166], a standard anatomical reference frame in MRI. Figure 4.1 shows the spatial patterns of histological r_{eff} across the mid-sagittal plane of the corpus callosum. Both samples exhibit a consistent, coarse inter-regional trend, following an alternating low–high pattern across the anterior midbody, midbody, posterior midbody, and splenium (see also Figure B.3). Notably, there is substantial intra-region variability within the splenium, which also appears inconsistent across tissue samples. In other subregions, intra-region variability cannot be reliably assessed due to sparser sampling.

4.2.2 In vivo MRI validation

To assess the experimental validity of r_{eff}, we acquired in vivo dMRI magnitude data from five healthy subjects using a Siemens Connectom 3 T scanner with a maximum diffusion gradient amplitude of 300 mT/m, following the protocol of Veraart et al. [6]. As an interpretive bridge between histology and dMRI, we additionally conducted

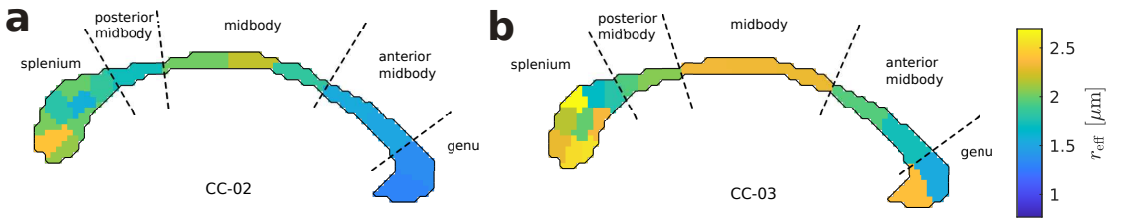

Figure 4.1: Histological patterns of r_{eff}. (a–b) Spatial distribution of histological r_{eff} across the mid-sagittal slice of the corpus callosum in MNI space. Spatial patterns were interpolated using the nearest-neighbor method, evaluated at histological ROI locations in Figure 1.1f. Dashed lines indicate corpus callosum subregions.

histology-based dMRI simulations under two conditions: (i) an experiment-like scenario with Rician noise (SNR = 32), and (ii) an idealized noise-free scenario (SNR = ∞). For comparison between dMRI-derived and histological values—including histology-based simulations—we accounted for shrinkage of ex vivo tissue relative to in vivo conditions by scaling radii in the histological axon radius distributions by a factor of 1.3 [17, 167].

In vivo dMRI captures coarse spatial pattern at the group level

Figure 4.2a–d compare group-average spatial r_{eff} patterns across the corpus callosum between histology, dMRI experiments, and simulations. The experimental dMRI pattern qualitatively resembles histology (see Figure 4.2a-b), showing an alternating low–high trend across anterior midbody, midbody, posterior midbody, and splenium (see also Figure B.4). However, the relatively high values in the genu deviate from the expected histological pattern.

Despite this coarse agreement, r_{eff} patterns from both experiments and simulations exhibit a reduced dynamic range compared to histology, indicating limited sensitivity to microstructural variation. While simulations correctly predict this reduction in sensitivity, they differ from experimental measurements in absolute values: simulations systematically underestimate r_{eff} (see Figure 4.2c–d), whereas experimental estimates show only a mild overestimation (see Figure 4.2b). This discrepancy suggests that additional effects—unaccounted for in the simulations—may influence the experimental signal.

Group-level r_{eff} correlate with histological values

Figure 4.2e shows a direct, ROI-wise comparison of r_{eff} values from dMRI experiments against histological values. The resemblance of the group-average spatial r_{eff} pattern from in vivo dMRI experiments with histology is reflected in a significant correlation. However, this analysis exhibited some variability due to the non-deterministic nature of our in vivo dMRI processing (Figure 4.2e shows a representative iteration; over 10 iterations, we yielded: $R = 0.414 \pm 0.03$, all $p < 0.05$; see Figure B.5).

A model-inherent bias drives sensitivity reduction

Figure 4.2f–g complement the experimental results in Figure 4.2e with dMRI simulations. Experiment-like simulations (see Figure 4.2f) do not predict the significant

correlation ($R = 0.29$, $p = 0.12$) found in the experimental data, likely because they represent single-subject scenarios rather than group-averages. In this setting, the underlying relationship is not strong enough to yield a correlation under noise, given the reduced sensitivity. While reduced sensitivity appears in both simulation scenarios, its persistence in the idealized scenario (see Figure 4.2g) clarifies that it is a model-inherent effect, which we label "model-inherent bias." This bias increases proportionally with r_{eff} and affects absolute agreement, as measured by the normalized root-mean-square error (NRMSE), by shifting values away from the unity line. It also reduces R by limiting the dynamic range on the upper end of r_{eff} values, thereby obscuring correlations under noisy conditions (see Figure 4.2e–f). Finally, noise introduces a mild overestimation of smaller r_{eff} values, which reduces sensitivity at the lower end of the distribution. This reduced sensitivity to small r_{eff} hints at the practical resolution limit, below which r_{eff} values may no longer be reliably distinguished from noise [157].

Lack of consistent subject-level correlations

Figure 4.3a presents per-subject spatial r_{eff} patterns from in vivo dMRI. These maps show considerable variability across subjects, with spatial patterns that only partially resemble their histological counterparts (cf. Figure 4.1). While the alternating low–high trend from anterior midbody to splenium observed at the group level is visible in some subjects, finer structures differ markedly. Additionally, partial volume effects may influence the patterns, as suggested by extreme values near border regions.

Figure 4.3b confirms these qualitative observations in quantitative terms: correlations between subject-level r_{eff} and pooled histological values are mostly weak and not statistically significant. Only one of five subjects shows a significant correlation (Subject 2: $R = 0.52$, $p = 1.4 \cdot 10^{-3}$). This absence of subject-level correlation aligns with our experiment-like simulations (cf. Figure 4.2f), suggesting that individual-level validation remains challenging due to inter-individual differences and limited sensitivity.

4.2.3 Ex vivo MRI validation

To enable direct comparison with histology in the same tissue, we acquired ex vivo dMRI data from the histologically sampled corpus callosum specimen CC-02 (see Figure 1.1f). We performed the acquisition on a Bruker Biospin 9.4 T preclinical scanner with a maximum diffusion gradient amplitude of up to 1500 mT/m, using a protocol similar to the one proposed by Veraart et al. for ex vivo validation in rodents [15].

Ex vivo dMRI fails to capture histological pattern

Figure 4.4a–d compare spatial r_{eff} patterns across histology, ex vivo dMRI experiments, and simulations. In both experiments and simulations, the dMRI patterns show a stronger reduction in sensitivity than in vivo (cf. Figure 4.2a-d), with r_{eff} values markedly underestimated. At this low sensitivity, no distinct spatial

variation in r_{eff} is captured in dMRI experiments and simulations, at least not at the magnitude expected from histology.

Ex vivo dMRI shows no correlation with histology

Figure 4.4e–g show ROI-wise comparisons of r_{eff} from dMRI experiments and simulations against histological values. In experimental data (Figure 4.4e), we find no significant correlation with histology ($R = 0.23$, $p = 0.41$), aligning with the poor agreement observed in spatial patterns. This absence of correlation contrasts with our experiment-like simulations (Figure 4.4f), which predicts a significant correlation ($R = 0.55$, $p < 1 \cdot 10^{-3}$). Part of this discrepancy may result from the lower number of ROIs in the experimental analysis (15) compared to simulations (35). However, the sensitivity appears intrinsically low, even under idealized conditions (see Figure 4.4g), suggesting that achieving meaningful sensitivity in experimental data may be challenging.

The immobile water compartment as an additional confounder

Fixation of ex vivo tissue introduces an immobile water compartment, represented by an additional model parameter (f_{im}), which may confound r_{eff} estimation. Figure 4.5 assesses this possibility by examining the covariation between estimated f_{im} and r_{eff} in experimental data.

Figure 4.5a shows f_{im} and r_{eff} patterns across the corpus callosum, revealing apparent covariation between the parameters. This effect is particularly pronounced in the splenium, which provides the densest sampling. In this region, a direct ROI-wise comparison (Figure 4.5b) shows a near-linear relationship between f_{im} and r_{eff}, indicating that f_{im} likely acts as a confounding factor under the employed estimation approach.

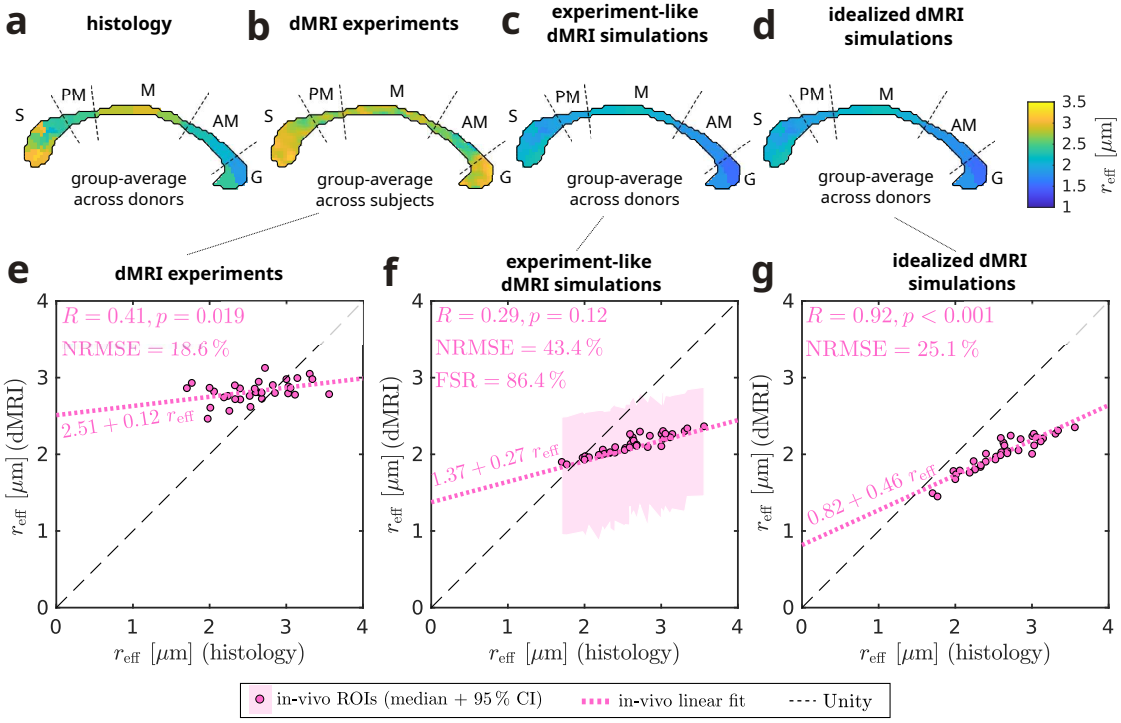

Figure 4.2: Validation of group-level in vivo MRI-based r_{eff}. **(a-d)** Group-level spatial r_{eff} pattern comparison under in vivo conditions: **(a)** histology, **(b)** dMRI experiments, **(c)** experiment-like dMRI simulations (SNR = 32), and **(d)** idealized dMRI simulations (SNR = ∞). Dashed lines indicate corpus callosum subregions: splenium (S), posterior midbody (PM), midbody (M), anterior midbody (AM), and genu (G). The patterns in (a, c-d) are based on histological axon radii scaled by 1.3 to compensate for tissue shrinkage with respect to in vivo conditions [17, 167]. In (c), the pattern reflects the median across 1000 noise realizations. **(e-g)** ROI-wise comparisons of r_{eff} between histological values and dMRI scenarios in (b-d), evaluated in each modality's native space. Markers correspond to histological ROIs in Figure 1.1f. While (e) shows the group-average, panel (f) represents a single-subject scenario, with markers denoting the median across 1000 noise realizations and the shaded area indicating the 95 % confidence interval. Dashed lines illustrate theoretical perfect agreement, whereas dotted lines represent linear regressions. Annotated metrics include Pearson's correlation coefficient (R) and corresponding p-value, normalized root-mean-square error (NRMSE), and the fitting success rate (FSR) (see Section 8.8.1 for metric definitions).

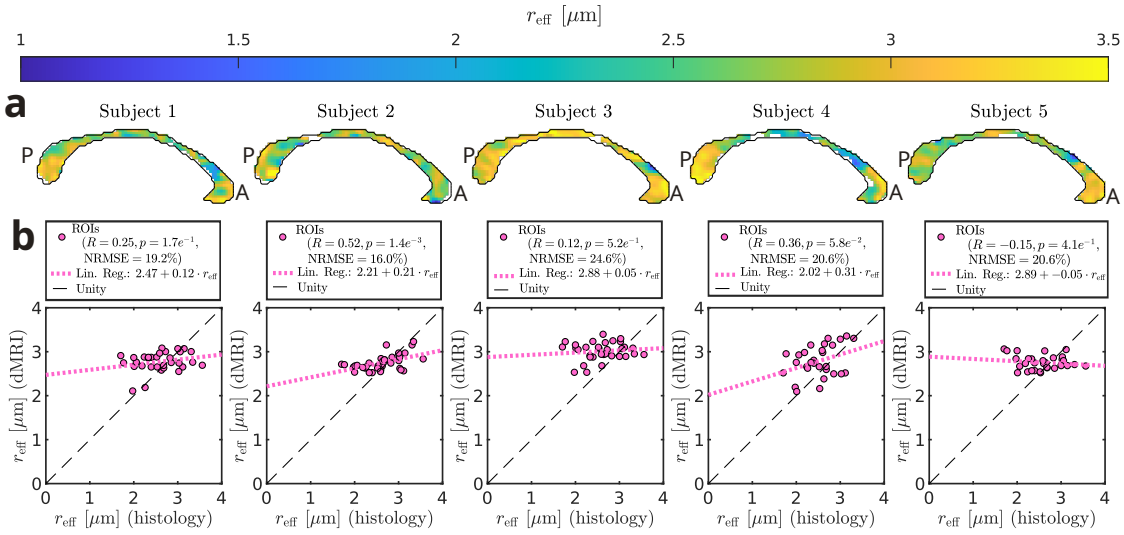

Figure 4.3: Validation of subject-level in vivo MRI-based r_{eff}. **(a)** Subject-level spatial patterns of in vivo dMRI-based r_{eff} across the corpus callosum, shown in mid-sagittal MNI slice. **(b)** ROI-wise correlations between subject-level MRI-based r_{eff} and histological values. Markers correspond to histological ROIs in Figure 1.1f. Dashed lines illustrate theoretical perfect agreement, whereas dotted lines represent linear regressions. Legends report Pearson's correlation coefficient (R), p-value, and normalized root-mean-square error (NRMSE) (see Section 8.8.1 for metric definitions). Histological values in (b) were scaled by 1.3 to compensate for tissue shrinkage [17, 167].

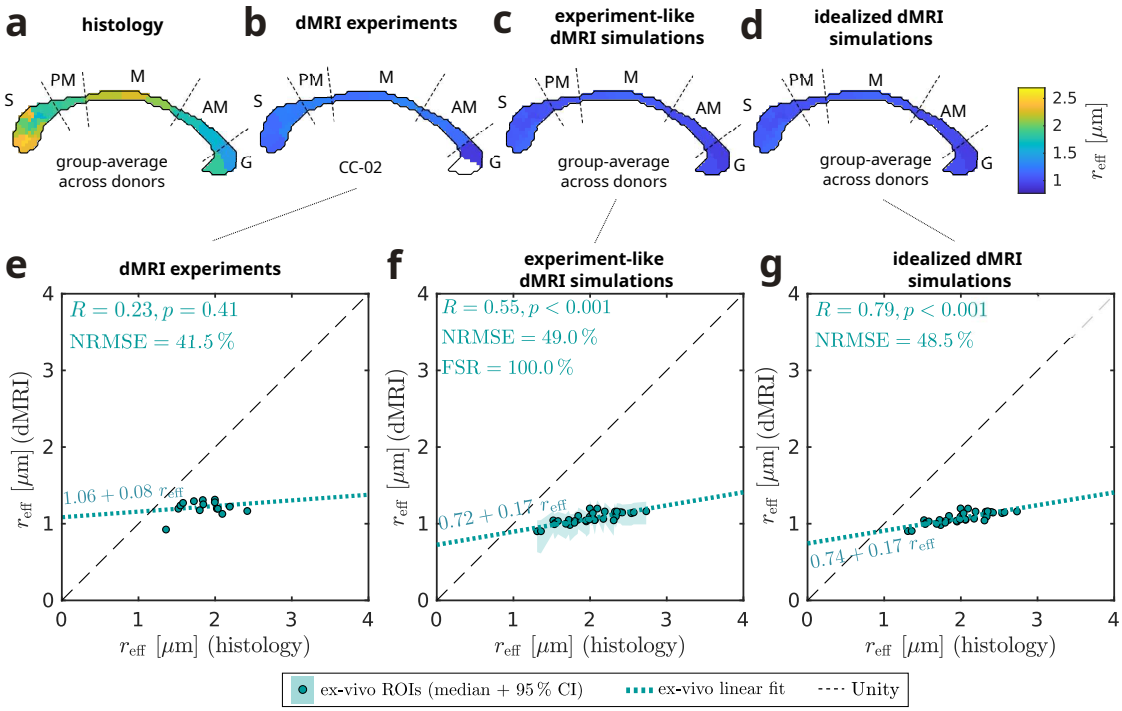

Figure 4.4: Validation of ex vivo MRI-based r_{eff}. **(a-d)** Spatial r_{eff} pattern comparison for ex vivo tissue sample CC-02 (see Figure 1.1f). Modalities include: **(a)** histology, **(b)** dMRI experiments, **(c)** experiment-like MRI simulations (b-dependent SNR = 17 to 51), and **(d)** idealized dMRI simulations (SNR = ∞). Dashed lines indicate corpus callosum subregions: splenium (S), posterior midbody (PM), midbody (M), anterior midbody (AM), and genu (G). The void in (b) denotes an ROI not scanned with ex vivo dMRI. In (c), the pattern reflects the median across 1000 noise realizations. **(e-g)** ROI-wise comparisons of r_{eff} between histological values and dMRI scenarios in (b-d), evaluated in each modality's native space. Markers correspond to histological ROIs in Figure 1.1f; while (e) includes only those ROIs scanned with ex vivo dMRI (CC-02), panels (f–g) include all ROIs (CC-02 and CC-03) to ensure comparability with the in vivo analysis in Figure 4.2. In (f), markers denote the median estimate across 1000 noise realizations, with the shaded area indicating the 95 % confidence interval. Dashed lines illustrate theoretical perfect agreement, whereas dotted lines represent linear regressions. Annotated metrics include Pearson's correlation coefficient (R) and corresponding p-value, normalized root-mean-square error (NRMSE), and the fitting success rate (FSR) (see Section 8.8.1 for metric definitions).

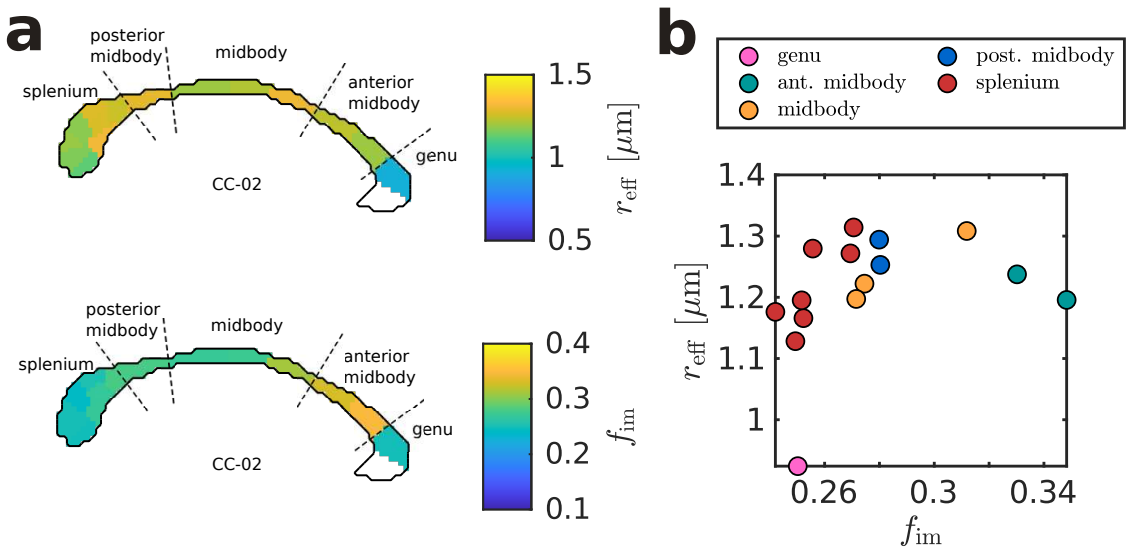

Figure 4.5: Impact of immobile water on ex vivo MRI-based r_{eff}. **(a)** Spatial patterns of ex vivo dMRI-based r_{eff} and immobile water fraction (f_{im}) across the corpus callosum, shown in a mid-sagittal MNI slice with subregions indicated (dashed lines). Spatial patterns were interpolated using nearest-neighbor interpolation, evaluated at the CC-02 histological ROI locations in Figure 1.1f. The void in the genu indicates an ROI not scanned with ex vivo dMRI. **(b)** ROI-wise comparison of r_{eff} and f_{im}. Markers correspond to CC-02 ROIs in Figure 1.1f.

4.3 Discussion

We addressed the longstanding challenge of quantitatively validating axon radius measurements from dMRI by assessing spatial correlations with histological values from two densely sampled human corpora callosa. A significant group-level correlation in vivo provides the first quantitative evidence that dMRI can capture microstructural variation in axon radii in the human brain, as demonstrated here via r_{eff}. Remarkably, this correlation emerges despite a newly identified "model-inherent bias" that reduces dMRI sensitivity to r_{eff}. Under ex vivo conditions, this sensitivity reduction is more pronounced and likely accounts for the absence of a significant correlation with histological values from the same tissue. We also illustrate that ex vivo r_{eff} estimation is further complicated by the presence of the immobile water fraction (f_{im}).

In vivo sensitivity persists despite confounds and model limitations

Mechanistically, our findings offer experimental proof that the in vivo dMRI signal in the human brain retains measurable sensitivity to r_{eff}. Notably, this sensitivity to r_{eff} is preserved despite unmodeled signal contributions affecting the core signal model assumptions of r_{eff}. In particular, a growing body of simulation studies [23–28] grounded in 3D histological work [23, 26, 148, 149] has raised concerns about the simplifying assumption of idealized, cylindrical axons underlying r_{eff} modeling. These studies show that realistic axonal geometries, including radius variations and undulations, can substantially alter the dMRI signal. Alongside the impact of geometric complexity, our results point to an additional modeling limitation: a model-inherent proportional bias that reduces sensitivity to r_{eff}. This effect is consistently present in both experiments and simulations. Crucially, it also appears in idealized simulations, suggesting that the bias affects the core axon radius–related signal.

Importantly, in vivo dMRI's sensitivity to r_{eff} holds up not only against modeling limitations of the axon radius-related signal, but also against a broader range of confounding influences. These include signal contributions from compartments not accounted for in the model [13, 15, 19–22], as well as exchange between intra- and extra-axonal compartments [19, 164, 165], axonal surface relaxation effects [38], orientation dispersion [27, 29, 30], partial volume contamination [107, 168], and Rician noise bias [31]. Comparisons between in vivo dMRI and histology introduce further sources of uncertainty, such as tissue deformation and shrinkage [17, 167, 169, 170], anatomical and demographic variation across individuals, cohort differences (e.g., the age differences in our data: mean age 61 years in histology vs. 31 years in vivo), and scan–rescan variability – although the latter has been shown to be modest for the acquisition protocol used here [6, 163].

Achieving specificity remains challenging

While the observed sensitivity to r_{eff} in vivo is encouraging, the myriad of confounding factors outlined above suggests that achieving true specificity to r_{eff} remains challenging. Indeed, our experimental in vivo data hint at such complexity: despite

simulations predicting underestimation due to model-inherent bias, we observe a slight overestimation of r_{eff} relative to histology. This suggests that additional confounding effects of comparable magnitude may be acting in the opposite direction, effectively compensating for model-inherent bias. Hence, comparing value ranges [15] rather than assessing point-wise relationships may be ambiguous and difficult to interpret. However, disentangling the individual contributions of confounding effects remains challenging, particularly due to their potential interactions. Therefore, in light of the previously unproven sensitivity of dMRI to r_{eff}, establishing experimental evidence of such sensitivity defined the scope of our analysis.

A coarse anatomical pattern drives in vivo correlation

From an anatomical perspective, the spatial variation underlying the in vivo dMRI–histology correlation reflects a coarse anterior-to-posterior trend across the corpus callosum, spanning the anterior midbody, midbody, posterior midbody, and splenium. This pattern is visible only at the group level and aligns most closely with previous findings in humans [41] and nonhuman primates [4, 147]. Differences to regional trends reported in other human studies [4, 6, 17, 20, 38, 42, 43] may stem from variations in anatomical definitions, ROI placement, acquisition protocols, and analysis methods, but could also partially reflect inter-individual variability in axon morphology. Indeed, our data suggests substantial inter-individual variability of in vivo r_{eff} patterns, raising the question of whether finer-grained spatial trends are preserved across subjects, or whether apparent differences simply reflect spatial shifts or misalignment. In light of this variability, confirming the sensitivity of in vivo dMRI to r_{eff} on independent datasets remains among the most immediate priorities, given the limited number of histology donors and in vivo subjects in our dataset.

Ex vivo validation appears challenging

Ex vivo validation is often used as an intermediate step toward in vivo validation, as it circumvents inter-individual differences by enabling direct comparison with histology in the same tissue [12, 14, 15, 37, 134–139]. However, our results suggest that such an approach may be difficult for r_{eff}. In line with the poor spatial correspondence observed in our experimental data, our simulations indicate that model-inherent bias strongly limits sensitivity – more so than in vivo. For practical measurements with the current ex vivo protocol, the sensitivity leaves little headroom to detect correlations if additional, confounding effects are present. One strong candidate for such an effect is the presence of an immobile water fraction (f_{im}) in ex vivo tissue [22]. In our results, the estimated f_{im} appears to covary with r_{eff}, challenging the specificity of r_{eff} estimates.

Large-scale 2D histology as a practical validation framework

The observed correspondence between in vivo dMRI–based r_{eff} and our 2D histology (see Chapter 3) supports the notion that axon radius distributions measured from 2D cross-sections can serve as reasonable proxies for the 3D microstructural environment underlying the dMRI signal. This interpretation is consistent with insights from recent 3D histology studies [26], which suggest that axon radius distributions, and by

extension r_{eff}, remain relatively stable within local fiber populations, although this has only been demonstrated for a small number (~ 50) of large axons. In light of our findings, large-scale 2D histology emerges as a complementary approach to current 3D histology efforts [23, 26, 148, 149]. While 3D histology uniquely enables dMRI simulations of complex axonal morphology on a few (~ 100) reconstructed axons [23–28, 149], our 2D approach offers a scalable and practical route for validating real-world dMRI measurements, providing unprecedented spatial sampling with access to 46 million axons across 35 ROIs.

Limitations and future directions

Our r_{eff} estimation assumes constant literature values for axoplasmic diffusivity (D_0) across voxels [82, 128], which may introduce bias if D_0 is misestimated and overlooks voxel-wise heterogeneity. However, prior work suggests only moderate sensitivity to deviations in D_0 [27]. Similarly, our simulations use fixed literature values for parameters such as axonal volume fraction [128], but this is unlikely to qualitatively challenge the major finding of reduced sensitivity due to model-inherent bias.

For histology–dMRI comparisons, we compensated for tissue shrinkage by uniformly scaling radii of individual axons, which unlikely captures all biological complexities, such as non-linear shrinkage in the extra-axonal space [169], altered fiber orientations [170], or region-specific shrinkage responses [171]. However, our correlation-based evaluation is robust to systematic biases in the absolute scale.

To mitigate alignment inaccuracies between modalities and suppress apparent noise in our in vivo dMRI-based r_{eff} maps, we applied spatial smoothing (see Figure B.6). While the smoothing limits sensitivity to subtle spatial variations, the considerable variability across subjects already casts doubt on whether consistent fine-scale structure exists across individuals.

Conclusion

Our findings demonstrate that in vivo MRI can capture anatomical variation in r_{eff}, as reflected by its significant spatial correlation with histological ground truth. This provides an important step toward validating MRI-based axon radius mapping and supports its potential for scientific and clinical applications. At the same time, the lack of individual-level correlations and discrepancies in ex vivo data highlights the need to better understand the method's limitations. In the next chapters, we address these gaps through histology-based simulations designed to better understand modeling limitations and study candidates for remaining discrepancies (see Chapter 5), as well as to explore the path towards adoption on clinical scanners (see Chapter 6).

Chapter 5

Understanding limitations of MRI-based axon radius mapping

This chapter is based on Mordhorst et al. [47], with adaptations and extensions for this thesis.

5.1 Introduction

The previous chapter provided the first quantitative evidence that dMRI can detect spatial variations in axon radius distributions in humans. Such experimental validation provides a comprehensive reality check, capturing the combined influence of many factors – biophysical modeling, acquisition protocols, processing pipelines, tissue properties, and even inter-individual variability. This comprehensiveness is both a strength and a limitation: while it validates the entire estimation chain, it does not isolate the underlying causes of either agreement – and, more critically, the remaining disagreement.

To disentangle these potential sources of disagreement, simulations offer a crucial complement to experimental validation, in particular for the complex biophysical microstructure model underlying r_{eff} estimation. This physically interpretable model goes beyond empirical fitting and provides a mechanistic link between microscopic structure, such as axon radius distributions, and dMRI signal formation at the macroscopic scale [121]. Simulations based on this forward model allow a systematic investigation of how individual factors, including acquisition parameters, noise characteristics, and modeling assumptions influence r_{eff} estimation under controlled conditions.

In the context of our experimental findings in Chapter 4, simulations may help clarify the observed sensitivity limitations. The limited sensitivity was due to an underestimation of large r_{eff}, resulting in a reduced dynamic range of estimated values. We labeled this effect "model-inherent bias" because it persisted even in simulations isolating axon radius–related signal components. As such, it joins other fundamental limitations – most notably, the unmodeled influence of complex axonal morphology [23, 25–28, 150], which violates the perfect cylinder assumption in

current axon radius dMRI signal models. Better understanding this bias is essential for improving sensitivity and for defining the anatomical and experimental conditions under which r_{eff} mapping remains viable.

A separate issue concerns specificity: our experimental results showed a global offset compared to simulations, whose origin is difficult to trace given the number of potential candidates. While some discrepancies are inherent to the validation design—particularly in comparisons between in vivo dMRI and histology—others likely stem from limitations in the dMRI signal model. These include insufficiently accounted for signal compartments [15, 19–22], exchange between intra- and extra-axonal compartments [19, 164, 165], axonal surface relaxation effects [38], fixed diffusivity assumptions [15, 27], or noise characteristics [31]. Identifying the most relevant contributors is essential to improving specificity and ensuring that observed variations in r_{eff} can be reliably attributed to underlying microstructural differences, especially with a view toward future clinical application.

In this chapter, we use histology-based dMRI simulations to investigate both the origin and implications of model-inherent bias in r_{eff} mapping, as well as the impact of potential confounding factors. We begin by examining signal approximations as candidate sources of the observed sensitivity reduction via the model-inherent bias and show that the effect arises directly from how axon radius distributions are compressed into the scalar metric r_{eff}. Moreover, we demonstrate that the magnitude of this effect increases with both r_{eff} itself and the diffusion gradient amplitude – making it particularly relevant under ex vivo conditions, where gradient strengths are typically higher. To assess potential confounders affecting specificity, we evaluate the influence of plausible inaccuracies in noise and model parameters. Our results show that incorrect estimation of the noise level can substantially distort r_{eff} when using magnitude dMRI with Rician-distributed signals. In ex vivo tissue, the immobile water fraction (f_{im}) emerges as an additional strong confounder.

5.2 Results

5.2.1 Origins of model-inherent bias

To identify the origins of the model-inherent bias, we examined the successive approximations made during the derivation of r_{eff} (see Section 2.3.6.2). Specifically, we compared their effects on powder-averaged signals $S^{\circ}(b)$, the signal level at which r_{eff} is fitted.

Figure 5.1 shows simulated $S^{\circ}(b)$ for both in vivo and ex vivo experimental MRI protocols across these approximations. The matrix method (see Appendix A) provides the most detailed representation among the evaluated approaches and therefore serves as a reference. All other methods introduce successive simplifications, as arranged from left to right in the legend, ultimately leading to the signal model used for r_{eff} fitting in experimental data.

The Taylor approximation drives the model-inherent bias
Both ex vivo and in vivo (see Figure 5.1a-d), deviations between approximations scale with r_{eff}, mirroring the proportional bias observed in r_{eff} itself. The Taylor approximation introduces by far the largest deviations among the successive approximations, thereby driving the model-inherent bias. The WPA causes only minor deviations, whereas the GPA aligns with the reference (matrix method) almost perfectly. Although the relative pattern of differences is consistent across ex vivo and in vivo conditions, deviations are overall stronger for the ex vivo case.

Dependence of the model-inherent bias on r_{eff} and acquisition parameters
The observed scaling of deviations with r_{eff} for the Taylor approximation and the WPA can be understood from their underlying dependencies. For the Taylor approximation, accuracy improves when the necessary but not sufficient condition $\kappa r_{\text{eff}}^4 \ll 1$ (with $\kappa = \frac{7}{48}\frac{g^2\gamma^2\delta}{D_0}$; κ values annotated above the plots) is satisfied. While violation of this condition with increasing r_{eff} is evident, the stronger deviations under ex vivo conditions arise from the quadratic dependency on g and the reduced D_0. Similarly, the WPA assumption ($\delta \gg r^2/D_0$) is less well satisfied ex vivo, where D_0 is reduced and δ is shorter (enabled by higher g). Thus, the stronger deviations observed in ex vivo dMRI likely reflect the combined impact of tissue properties and acquisition settings.

Powder-averaged signals decay near-linearly at high b
Interestingly, $S^\circ(b)$ appears to decay almost linearly with r_{eff} for protocols with high b (see Figure 5.1b,d). This behavior suggests an intrinsic property of the signal model, warranting further exploration.

5.2.2 Implications of model-inherent bias

To assess the implications of model-inherent bias beyond the human corpus callosum, we mimicked axon radius distributions of other axon populations. Specifically, we applied scaling factors to our human corpus callosum axon radius distributions to extrapolate to the rat corpus callosum (scaling factor: 0.5 [15]) and the human corticospinal tract (scaling factor: 1.15 [6]).

Figure 5.2a illustrates the resulting distributions alongside their corresponding r_{eff} values. Figure 5.2b–c show ROI-wise comparisons of r_{eff} between dMRI simulations and histological values for these populations, evaluated under both ex vivo and in vivo protocols.

The previously observed trends – stronger model-inherent bias at larger r_{eff} and under ex vivo conditions – persist across axon populations (see Figure 5.2b–c). The extended r_{eff} range across populations provides a broader perspective on how the bias scales, revealing a nonlinear relationship with a tendency toward saturation at large r_{eff}. In small-axon populations such as the rat corpus callosum, the comparatively mild model-inherent bias may facilitate accurate validation, provided that lower r_{eff} values remain distinguishable from noise under experimental conditions [157]. Conversely, in regions with particularly large axons, such as the human corticospinal

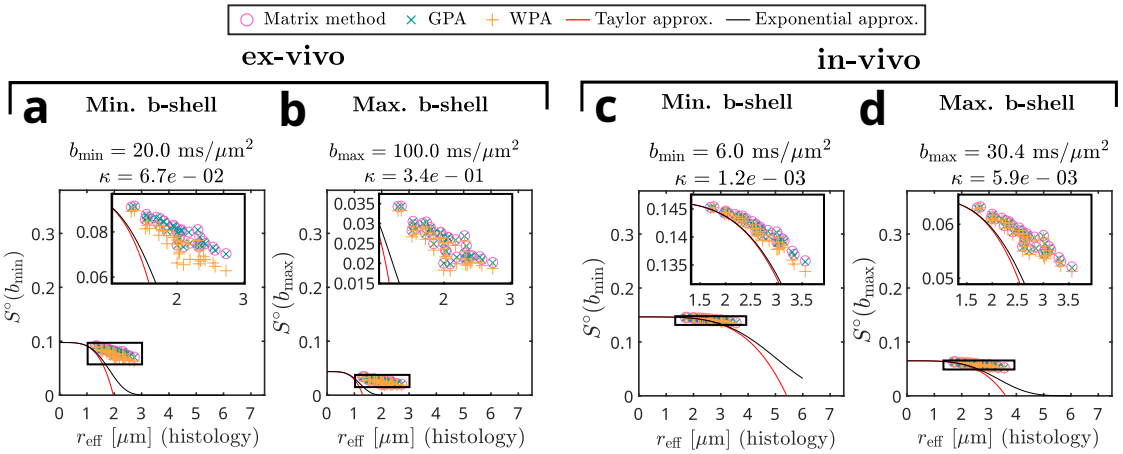

Figure 5.1: Origins of model-inherent bias. **(a–b)** Ex vivo simulated powder-averaged signals $S^\circ(b)$ for: **(a)** the minimum $b = b_{\text{min}}$ shell and **(b)** the maximum $b = b_{\text{max}}$ shell (see annotated b values). Marker symbols/lines represent different $S^\circ(b)$ approximations. The matrix method provides the most accurate approach and serves as the reference. All other methods introduce successive simplifications, as arranged from left to right in the legend, ultimately leading to the signal model used for r_{eff} estimation. Approximations shown as markers correspond to simulations based on axon radius distribution–weighted signals, with individual markers representing histological ROIs in Figure 1.1f. In contrast, lines depict $S^\circ(b)$ at later approximation stages, where the axon radius distribution is incorporated into r_{eff}, allowing $S^\circ(b)$ to vary continuously. The annotated κ values encode a constant used in the wide pulse approximation (WPA), which depends both on acquisition and tissue parameters. **(c–d)** In vivo simulated $S^\circ(b)$, following the same definitions as in (a–b). For all panels (a–d), simulations were performed using Equation (2.51) with the matrix method, whereas the approximations correspond to Equations (2.41), (2.42), (2.45) and (2.46).

tract, the bias is more pronounced, illustrating the method's inherently lower sensitivity in brain regions characterized by large r_{eff}.

5.2.3 Modeling assumptions as confounders

Beyond r_{eff}, the signal model used for fitting relies on several assumptions: fully decayed extra-axonal signal ($S_{\text{e}} = 0$) and fixed values for axoplasmic diffusivity ($D_0 = 0.35\,\mu\text{m}^2/\text{ms}$ ex vivo and $D_0 = 2.07\,\mu\text{m}^2/\text{ms}$ in vivo). In ex vivo tissue, one also needs to estimate the immobile water fraction (f_{im}). Violations of these assumptions or inaccuracies in their estimation ($\hat{f}_{\text{im}}, \hat{D}_0$) may bias r_{eff}. Here, we assess these effects by simulating the impact of residual extra-axonal signal ($S_{\text{e}} > 0$) and by systematically varying $\hat{f}_{\text{im}}$ and $\hat{D}_0$ relative to the ground-truth values used for signal simulation.

Residual extra-axonal signal introduces modest offset

Figure 5.3 shows how residual extra-axonal signal affects estimated r_{eff} values compared to the case of fully decayed extra-axonal signal, under both ex vivo (see

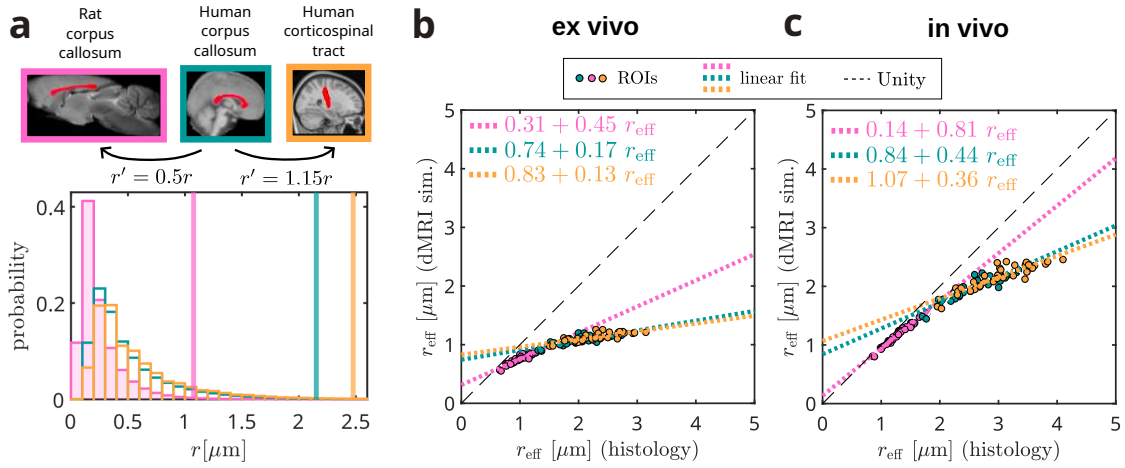

Figure 5.2: Implications of model-inherent bias. **(a)** Axon radius distributions for different populations: rat corpus callosum (magenta), human corpus callosum (green), and human corticospinal tract (orange). Vertical lines indicate the corresponding r_{eff} values. To synthesize axon radius distributions for the rat corpus callosum and human corticospinal tract, we applied literature-derived scaling factors to axon radii from our primary dataset of the human corpus callosum (see annotations). The displayed distributions correspond to the ex vivo scenario; for in vivo simulations, an additional scaling factor of 1.3 was applied to account for tissue shrinkage [17, 167]. **(b-c)** ROI-wise comparisons of r_{eff} from idealized dMRI simulations (SNR $= \infty$) against histological r_{eff} for each population in (a), evaluated under: **(b)** the experimental ex vivo protocol and **(c)** the experimental in vivo protocol. Marker/line colors indicate axon population as in (a). Markers correspond to histological ROIs in Figure 1.1f. Dashed lines illustrate theoretical perfect agreement, whereas dotted lines represent linear regressions.

Figure 5.3a) and in vivo (see Figure 5.3b) conditions.

Residual extra-axonal signal introduces a modest overestimation of r_{eff}, particularly in the in vivo case and for smaller r_{eff} values. While R remains largely unaffected by residual extra-axonal signal, NRMSE is reduced because the overestimation partially compensates for the model-inherent bias.

Inaccuracies in D_0 have minimal impact on r_{eff}

Figure 5.4 studies the impact of imperfect D_0 estimation, with panels Figure 5.4a,d showing r_{eff} comparisons with histological values for both ex vivo and in vivo conditions. Panels Figure 5.4b–c,e–f show the resulting R and NRMSE as a function of relative misestimation ($\hat{D}_0/D_0$).

Inaccuracies in $\hat{D}_0$ have only moderate effects on estimated r_{eff} (see Figure 5.4a,d), with only minor offsets visible even under substantial under- or overestimation of up to 50 %. This insensitivity to misestimation translates into stable R and NRMSE values across a broad range of $\hat{D}_0$ settings (see Figure 5.4b-c,e-f).

Inaccuracies in f_{im} strongly affect r_{eff}

Figure 5.5 repeats the D_0 analysis from Figure 5.4, but for f_{im}. Here, only ex vivo conditions are shown, assuming that f_{im} is present only in ex vivo tissue [22, 172].

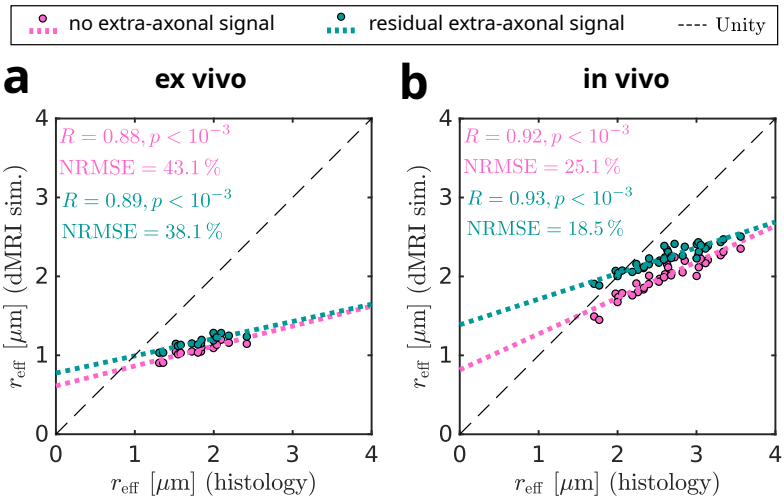

Figure 5.3: Impact of residual extra-axonal signal. **(a)** ROI-wise comparisons of r_{eff} from ex vivo dMRI simulations (SNR $= \infty$) against histological r_{eff}, comparing signals simulated with a fully decayed (magenta) or residual (green) extra-axonal signal (S_{e}). In both cases, r_{eff} was fitted under the assumption of fully decayed extra-axonal signal. Markers correspond to histological ROIs in Figure 1.1f. The dashed line illustrates theoretical perfect agreement, whereas the dotted line represents a linear regression. Legend reports Pearson's correlation coefficient (R), p-value, and normalized root-mean-square error (NRMSE) (see Section 8.8.1 for metric definitions). **(b)** Impact of residual extra-axonal signal on in vivo dMRI-based r_{eff}, following the same definitions as in (a).

Even mild deviations from the ground truth in $\hat{f}_{\mathrm{im}}$ introduce noticeable offsets in r_{eff} estimates (see Figure 5.5a), indicating that inaccuracies in $\hat{f}_{\mathrm{im}}$ can strongly confound ex vivo r_{eff} estimation. While R is only mildly affected, NRMSE is highly sensitive to bias introduced by inaccurate $\hat{f}_{\mathrm{im}}$ (see Figure 5.5b-c). The NRMSE reaches its minimum when this bias compensates for the model-inherent underestimation – corresponding to the blue markers in Figure 5.5a.

5.2.4 Noise as a confounder

To assess the impact of measurement noise on r_{eff} estimation, we conducted simulations with Gaussian and Rician noise. We used the corresponding maximum likelihood (ML) estimators during the powder-averaging step across directions $\mathbf{g}$, an intermediate stage before r_{eff} fitting. In the Rician case, we also tested the impact of inaccuracies in noise level (σ) estimates $\hat{\sigma}$, which is required for Rician ML fitting.

Figure 5.6a–b,e–f compare estimated r_{eff} against histological values under Gaussian and Rician noise, both in ex vivo and in vivo settings. For Rician noise (see Figure 5.6b,f), the analysis is shown for various $\hat{\sigma}$.

In the ex vivo case, neither the noise distribution nor the choice of $\hat{\sigma}$ in the Rician noise scenario substantially affects r_{eff}, R, or NRMSE (Figure 5.6a–d), likely due to the relatively high SNR.

For in vivo dMRI (Figure 5.6e–h), differences between Gaussian and Rician noise

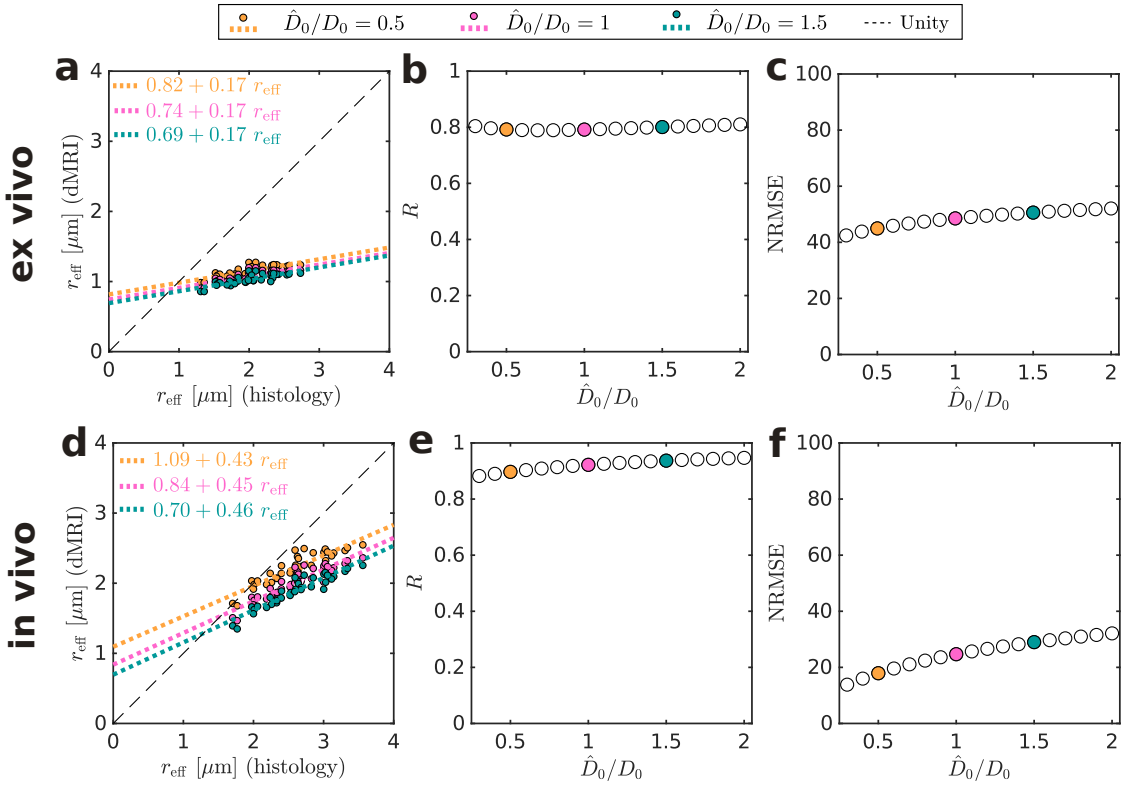

Figure 5.4: Impact of axoplasmic diffusivity estimation. **(a)** ROI-wise comparisons of simulated ex vivo dMRI-based r_{eff} and histological values for different axoplasmic diffusivity (D_0) estimates, denoted as $\hat{D}_0$ (see legend). Here, signals were simulated using ground truth D_0, while fitting assumed $\hat{D}_0$. Markers correspond to histological ROIs in Figure 1.1f. Dashed lines illustrate theoretical perfect agreement, whereas dotted lines represent linear regressions. **(b–c)** Error metrics as a function of relative misestimation ($\hat{D}_0/D_0$): **(b)** Pearson's correlation coefficient (R) and **(c)** normalized root-mean-square error (NRMSE) (see Section 8.8.1 for metric definitions). Colored markers indicate the $\hat{D}_0$ values shown in (a). **(d–f)** In vivo dMRI equivalents of (a–c).

become apparent even in the idealized case of perfectly estimated noise level ($\hat{\sigma} = \sigma$). Although the resulting r_{eff} values appear qualitatively similar, R and NRMSE are slightly improved under Gaussian noise (see magenta markers versus blue lines in Figure 5.6g-h). This suggests that the Rician ML estimator does not fully correct for the noise floor – despite accurate knowledge of σ. When $\hat{\sigma} \neq \sigma$, estimation errors propagate into the r_{eff} estimates, introducing noticeable offsets. Interestingly, both R and NRMSE become optimal when $\hat{\sigma} > \sigma$. For NRMSE, this improvement likely reflects partial compensation of the model-inherent underestimation bias. For R, we hypothesize that overestimating σ leads to overcorrection of the Rician bias, effectively suppressing the noise floor at the cost of r_{eff} overestimation. This effect, however, is not observed in experimental data (see Figure B.7), possibly due to greater voxel-wise heterogeneity in parameters such as orientation dispersion, which is not captured in our simulations.

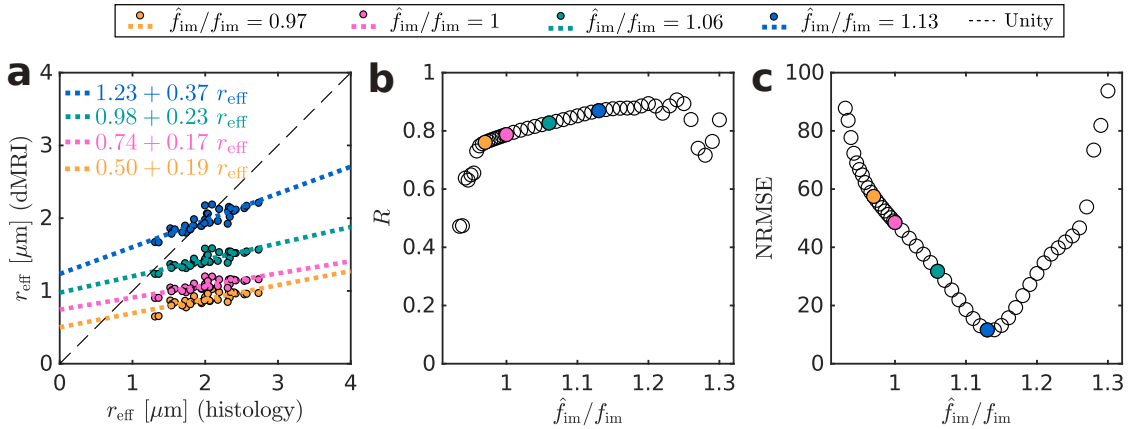

Figure 5.5: Impact of immobile water fraction estimation. **(a)** ROI-wise comparisons of simulated ex vivo dMRI-based r_{eff} and histological values for different immobile water fraction (f_{im}) estimates, denoted as $\hat{f}_{im}$ (see legend). Here, signals were simulated using ground truth f_{im}, while fitting assumed $\hat{f}_{im}$. Markers correspond to histological ROIs in Figure 1.1f. Dashed lines illustrate theoretical perfect agreement, whereas dotted lines represent linear regressions. **(b-c)** Error metrics as a function of relative misestimation ($\hat{f}_{im}/f_{im}$): **(b)** Pearson's correlation coefficient (R) and **(c)** normalized root-mean-square error (NRMSE) (see Section 8.8.1 for metric definitions). Colored markers indicate the $\hat{f}_{im}$ values used in (a).

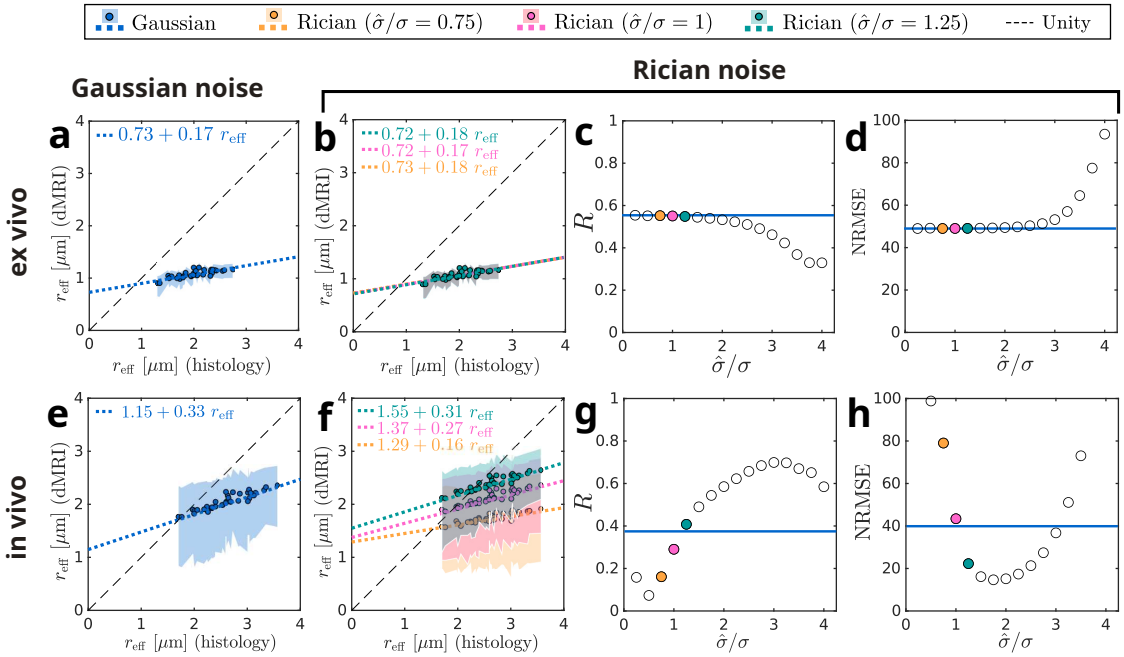

Figure 5.6: Noise as a confounder. **(a-b)** ROI-wise comparisons of ex vivo dMRI-based r_{eff} and histological values for **(a)** Gaussian noise and **(b)** Rician noise. Color coding in (b) indicates different noise level (σ) estimates, denoted as $\hat{\sigma}$. Here, signals were simulated using ground truth σ, while fitting assumed $\hat{\sigma}$. Markers correspond to histological ROIs in Figure 1.1f. Dashed lines illustrate theoretical perfect agreement, whereas dotted lines represent linear regressions. **(c-d)** Error metrics as a function of relative misestimation ($\hat{\sigma}/\sigma$): **(c)** Pearson's correlation coefficient (R) and **(d)** normalized root-mean-square error (NRMSE) (see Section 8.8.1 for metric definitions). Colored markers correspond to the $\hat{\sigma}$ values used in (b), whereas the solid blue line corresponds to the Gaussian noise scenario in (a). **(e-g)** In vivo dMRI equivalents of (a-d).

5.3 Discussion

We revisited the experimental validation of state-of-the-art dMRI protocols for r_{eff} estimation using simulations, aiming to better understand the driving forces behind limitations in sensitivity and specificity observed in the experimental results (see Chapter 4). For sensitivity, the key limitation—previously identified as a model-inherent bias—is shown here to stem from a violated modeling assumption, related to how the axon radius distribution is compressed into the scalar metric r_{eff}. This leads to a disproportionately strong underestimation of large r_{eff}, imposing anatomical constraints in brain regions with large axons, and practical limitations when using high gradient amplitudes typical for ex vivo dMRI. In terms of specificity, we examined how plausible inaccuracies in model parameters affect r_{eff} estimates. The most pronounced effects stem from incorrect assumptions about the immobile water fraction (f_{im}) under ex vivo conditions and the noise level (σ).

Implications of model-inherent bias

We investigated the origin of the model-inherent bias and found that it depends predominantly on r_{eff} and the diffusion gradient amplitude. Adding to these theoretical insights, we extrapolated from our corpus callosum histology to other axon populations to explore the practical implications of the bias.

While in vivo experimental validation in Chapter 4 demonstrated that dMRI can capture group-level correlations with histological r_{eff} in the corpus callosum, our simulations reveal that further challenges may arise in other brain regions. The model-inherent bias increases non-linearly with r_{eff}, saturating toward larger values, and may therefore limit sensitivity in areas with larger axons such as the corticospinal tract [5, 6]. Additionally, the dependency of the model-inherent bias on diffusion gradient amplitude suggests that sensitivity could further decline on newer research scanners with even stronger diffusion gradients of up to 500 mT/m than those used in our study (300 mT/m). While such high gradient amplitudes are beneficial for resolving small r_{eff} [6, 14, 30, 42, 157], their impact on sensitivity reduction to large r_{eff} is another factor that may be relevant for protocol design.

Under ex vivo conditions, the sensitivity reduction becomes even more pronounced. Although our ex vivo experimental data (Chapter 4) already suggested this limitation, the analyses in this chapter show that the limited sensitivity is inherent to ex vivo conditions by providing a mechanistic explanation: the combination of high diffusion gradient amplitudes and low axoplasmic diffusivity (D_0) typical of ex vivo tissue amplifies the model-inherent bias, effectively diminishing sensitivity to r_{eff}. While practical measurements may retain sufficient sensitivity in species with predominantly small axons, such as rats, the sensitivity in human white matter appears prohibitively low – at least for the investigated experimental protocol. Consequently, validation studies performed in rodents [15, 40] are not only anatomically limited in their relevance [173], but would also likely fail to generalize due to fundamentally different sensitivity constraints.

The impact of noise distribution

Our simulations highlight the advantages of Gaussian over Rician-distributed signals in dMRI. Rician noise, typical of magnitude dMRI, arises from rectifying complex-valued signals and introduces a signal-dependent bias at low SNR – commonly known as Rician noise bias [31]. Correcting this bias requires an accurate estimate of the noise level σ [32–34], whereas no such estimate is needed when working with Gaussian-distributed signals. Even when σ is known, Rician-distributed signals yield lower Pearson's correlation (R) and higher normalized root-mean-square error (NRMSE) than Gaussian-distributed signals. In practice, σ must always be estimated, and inaccuracies in this estimate lead to under- or overcompensation of the Rician noise bias, resulting in substantial residual bias in r_{eff}. Interestingly, our simulations showed that overestimating σ can increase R, though at the cost of increased bias in absolute r_{eff} values. This apparent improvement may reflect an illusory gain of our idealized simulations, as the effect did not persist in our experimental data – likely due to greater tissue heterogeneity (e.g., voxel-wise variation in dispersion or diffusivity). Overall, we recommend preprocessing pipelines that enforce Gaussian-distributed real-valued dMRI signals [104–106], which eliminate the need for σ estimation.

Immobile water is a critical confounder ex vivo

Our simulations show that small inaccuracies in estimating the immobile water fraction (f_{im}) can strongly bias r_{eff} in ex vivo tissue. This is concerning, as our experimental results in Chapter 4 showed covariation between r_{eff} and f_{im}, suggesting that estimates may lack specificity – at least with our estimation approach. Based on our ex vivo estimation, we assumed that f_{im} would contribute 27 % to the non-diffusion-weighted signal, which is notably higher than the values of 8 to 17 % obtained with a dedicated acquisition in rodents [15]. This discrepancy may also reflect differences in fixation techniques: immersion fixation, as used here, and perfusion fixation, as in the rodent study [15], can have different effects on diffusion and compartmental water fractions [174, 175]. Regardless of the exact magnitude of f_{im}, its substantial contribution—as a non-decaying signal component—can become dominant at strong diffusion weighting, where most other compartments are strongly attenuated. To address this confounding effect, recent methods propose avoiding explicit estimation of f_{im} by modeling the spherical variance of the dMRI signal instead of its spherical mean [20, 176]. However, the practical feasibility of these approaches remains to be systematically evaluated, given their potentially increased demands on SNR and directional sampling.

Axoplasmic diffusivity and extra-axonal signal appear less influential

Imperfect assumptions about D_0 had only limited effect in our simulations, aligning with previous findings [27]. This is likely due to the fourth-root dependency in r_{eff} estimation. Similarly, residual extra-axonal signal (S_{e}) appears effectively suppressed in the diffusion regimes of the evaluated protocols. While our conclusions are based on simulations using corpus callosum literature values [128], they are consistent with in vivo experimental evidence in whole white matter [19].

Limitations and future directions

Our simulation-based assessment of potential confounding factors was designed to illustrate plausible explanations for the global offsets observed in experimental r_{eff} estimates (see Chapter 4). While we considered several prominent candidates, the assessment remains non-exhaustive and omits other plausible contributors, such as somas [21], exchange between intra- and extra-axonal compartments [19, 164, 165], axonal surface relaxation effects [38], and the influence of complex axonal morphology [23, 25–28]. Importantly, our approach serves to demonstrate the potential magnitude of specific confounders, but identifying the dominant contributors in experimental data would require targeted experimental investigations beyond the scope of simulations alone.

Unmodeled effects could also influence how the model-inherent bias manifests in realistic tissue. The bias stems from compressing axon radius distributions into the scalar r_{eff}, and our simulations focused on across-axon variation sampled with 2D histology. While recent work suggests that r_{eff} also reflects along-axon variation [150], our analyses show that the bias will continue to scale with r_{eff}. Thus, the practical impact of the bias would only change if the altered distributions substantially shift the resulting r_{eff} regime.

An alternative approach to reduce the model-inherent bias at large r_{eff} may involve measurements in the narrow-pulse limit ($\delta \ll r^2/D_0$) rather than the wide-pulse limit ($\delta \gg r^2/D_0$) used in our work. In this regime, the effective axon radius is given by $r_{\text{eff,narrow}} = \sqrt{\langle r^4 \rangle / \langle r^2 \rangle}$ [14, 16], which emphasizes smaller radii. Consequently, narrow-pulse measurements can be expected to yield smaller values in humans, thereby reducing the model-inherent bias that grows with r_{eff} under wide-pulse conditions.

Finally, refining the signal model appears to be an immediate avenue for improvement – either by incorporating higher-order terms in the Taylor approximation or by exploring the apparent linear decay of powder-averaged signals with r_{eff}.

Conclusion

Taken together, our results offer a deeper understanding of the mechanisms limiting r_{eff} mapping with current dMRI protocols and their practical consequences. By identifying key factors underlying limited sensitivity and highlighting strong candidates that reduce specificity, we provide a mechanistic basis to guide future improvements in modeling and experimental design. Practically, we find that, in vivo, sensitivity may be constrained in brain regions with very large axons, while the inherently low sensitivity under ex vivo conditions raises fundamental questions about the feasibility of ex vivo validation for r_{eff}. Building on these insights, the next chapter explores how in vivo dMRI protocols can be optimized for clinically feasible r_{eff} mapping (see Chapter 6).

Chapter 6

Towards clinical translation of MRI-based axon radius mapping

This chapter is based on Mordhorst et al. [47], with adaptations and extensions for this thesis.

6.1 Introduction

While the validation of r_{eff} sensitivity to anatomical variation on in vivo research dMRI scanners in Chapter 4 marks a key milestone, it remains only an initial step toward meaningful application. To realize the clinical potential of r_{eff}, the next major challenges are to establish its technical feasibility on clinical dMRI scanners and to evaluate its utility as a biomarker for neurological disorders.

Although a few studies have applied dMRI-based axon radius mapping in clinical research [177, 178], its broader adoption remains limited due to validation challenges and technical constraints on clinical MRI systems. In contrast, histological evidence of disease-related changes in axon caliber is more prevalent, including the loss of large axons or focal swellings due to disrupted axonal transport. Such effects have been reported in autism spectrum disorder (ASD) [7, 8], multiple sclerosis [9], Parkinson's disease [11], Alzheimer's disease [10], and related disorders [179, 180]. Importantly, large axons—or their selective loss—appear to play a critical role in pathology. Fortunately, these are precisely the axons to which r_{eff} is most sensitive, positioning it as a promising imaging biomarker for detecting such abnormalities in clinical research.

The absence of r_{eff} mapping on clinical scanners has largely reflected a technical barrier. Conventional clinical MRI systems, with gradient amplitudes limited to approximately 80 mT/m, are widely considered insufficient for reliable r_{eff} estimation [14, 15, 30, 42, 157]. In contrast, most studies demonstrating promising results with r_{eff} mapping have relied on advanced research scanners with gradient amplitudes of up to 300 mT/m—including the system used for in vivo experiments in this thesis (see Chapter 4). However, the emergence of next-generation clinical scanners offering gradient amplitudes up to 200 mT/m now substantially narrows this gap

and motivates a re-evaluation of whether clinically feasible protocols for r_{eff} mapping can be developed.

The design of such protocols has largely relied on Cramér–Rao lower bound (CRLB) analyses, which optimize the precision for an unbiased estimator [6, 181–183]. However, these analyses cannot account for model violations or systematic biases, such as the reduction in sensitivity caused by model-inherent bias, as demonstrated in Chapters 4 and 5.

In this chapter, we present a data-driven framework for optimizing in vivo dMRI protocols for r_{eff} mapping, using simulations grounded in our histological dataset of the human corpus callosum. We show that, provided substantial improvements in SNR can be achieved, r_{eff} mapping may become feasible on emerging clinical scanners with maximum gradient amplitudes ($g_{\max}$) up to 200 mT/m. We propose specific acquisition protocols and illustrate their potential in a hypothetical clinical scenario, distinguishing individuals with ASD from healthy controls based on r_{eff}. Finally, we extend our optimization to next-generation research scanners with $g_{\max}$ up to 500 mT/m—exceeding the 300 mT/m system used in this thesis—and show that model-inherent bias ultimately limits the achievable gains on these scanners.

6.2 Results

6.2.1 Optimal in vivo MRI protocols

We optimized dMRI protocols across existing in vivo 3 T scanners, spanning the range of clinical scanners with $g_{\max}$ up to 200 mT/m, as well as research scanners with $g_{\max}$ up to 500 mT/m. For each $g_{\max}$, we conducted a protocol parameter grid search and evaluated protocol candidates by assessing their Pearson's correlation (R) between histological r_{eff} and simulated r_{eff} under Gaussian noise, focusing on clinically relevant single-subject correlations across the ROIs in Figure 1.1f. We accounted for protocol parameter–dependent signal-to-noise (SNR) variations and additionally considered increases in baseline SNR, independent of protocol parameters, to explore potential gains achievable through technical or acquisition improvements.

Next-generation clinical scanners could narrow gap to research scanners Figure 6.1 shows R and normalized root-mean-square error (NRMSE) as a function of $g_{\max}$ across a range of SNR baselines. In general, higher performance corresponds to larger R and smaller NRMSE, both of which improve with increasing $g_{\max}$ up to an optimal value. Beyond this point, R tends to plateau while NRMSE begins to rise again, indicating diminishing returns of higher $g_{\max}$. While the optimum is typically accessible or nearly so with research scanners, current state-of-the-art clinical scanners consistently operate well below this range. In contrast, next-generation clinical systems – despite having $g_{\max}$ values only midway between current clinical and research scanners – yield R and NRMSE values much closer to research scanners, especially at increased SNR baselines. Figure B.8 replicates the analysis in Figure 6.1 for various assumptions on tissue shrinkage, showing similar

qualitative trends.

Next-generation scanners may support correlation at sufficient SNR
Figure 6.2 illustrates selected results from Figure 6.1 in more detail, focusing on optimal next-generation clinical scanner protocols. It shows correlations between r_{eff} simulations and histological values at different SNR levels, corresponding to the diamond markers in Figure 6.1. At SNR ≈ 27, corresponding to the expected SNR of the protocol candidate under our experimental conditions in Chapter 4, next-generation clinical scanners would not support a significant subject-level correlation with our histology data ($R = 0.29$, $p = 0.13$; see Figure 6.2a). However, a significant correlation could be revealed at SNR ≈ 48 ($R = 0.49$, $p = 3.7{\cdot}10^{-3}$; Figure 6.2b) and a stronger correlation at SNR ≈ 68 ($R = 0.63$, $p < 0.05$; Figure 6.2c). Figure B.9 provides complementary correlation plots for all scanner classes highlighted in Figure 6.1, suggesting that improvements are largely precision-driven across most g_{max} and SNR baselines.

Protocol design requires a trade-off between sensitivity and bias
The deterioration of NRMSE at high g_{max} observed in Figure 6.1b highlights a challenge for protocol design. Up to a certain point, increases in g_{max} improve both R and NRMSE, suggesting that improved precision drives both metrics. Beyond this optimal range, however, R plateaus while NRMSE worsens, indicating that the model-inherent bias begins to dominate (see also Figure B.9). This trade-off between precision and bias becomes particularly relevant for protocol design on ultra-high-gradient next-generation research systems.

6.2.2 Clinical application simulation

Figure 6.3 illustrates a hypothetical application of r_{eff} mapping on the next-generation clinical scanner protocols evaluated in Figure 6.2. Specifically, we estimated the required sample sizes (assuming equal group sizes) to distinguish individuals with ASD from healthy controls, based on a reported 28.6 % reduction in axon radii in the splenium under ASD conditions (see Figure 6.3a–c). This analysis follows the approach of Veraart et al. [6], who assessed cohort-level detectability of r_{eff} differences through statistical power estimation in the presence of scan–rescan variability, whereas our analysis models the anatomical variation of axon radii within the splenium based on our histological dataset.

Figure 6.3d presents the statistical power as a function of group size. A typical power target of 0.9 could be achieved with 12 subjects per group at SNR ≈ 27, corresponding to the conditions of our experimental protocol. Increasing the SNR to SNR ≥ 48 would substantially reduce the group size requirement to 6 or fewer subjects per group.

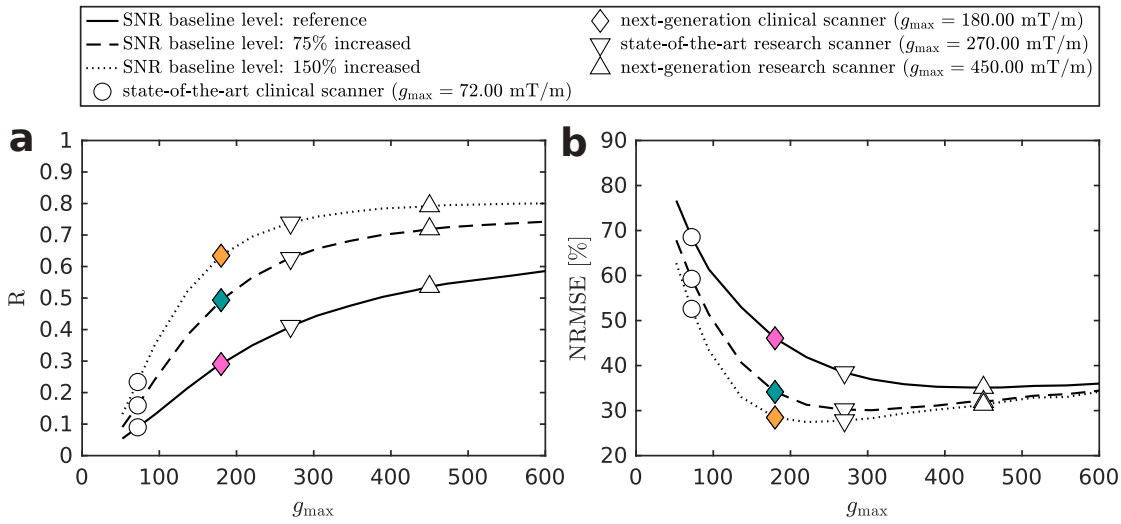

Figure 6.1: In vivo MRI protocol optimization metrics. **(a-b)** Performance metrics as a function of maximum gradient amplitude (g_{max}): **(a)** Pearson's correlation coefficient (R) and **(b)** normalized root-mean-square error (NRMSE). Markers encode g_{max} of existing clinical scanners and research scanners (assuming 90 % of the nominal g_{max}). Line colors indicate different SNR baseline levels. While the reference SNR baseline level reflects our experimental conditions, increased SNR baseline levels assume an SNR increase through potential technical or acquisition advances. In addition, the SNR of a particular protocol candidate depends on the protocol parameters (see Equation (8.12)). For our experimental protocol, baseline SNR levels would correspond to SNR values of 32 (reference), 56 (75 % increased), and 80 (150 % increased). Note that we optimized protocols by maximizing R, whereas NRMSE is an auxiliary metric. The full set of scanner protocol parameters highlighted by markers in (a-b) is listed in Table C.1.

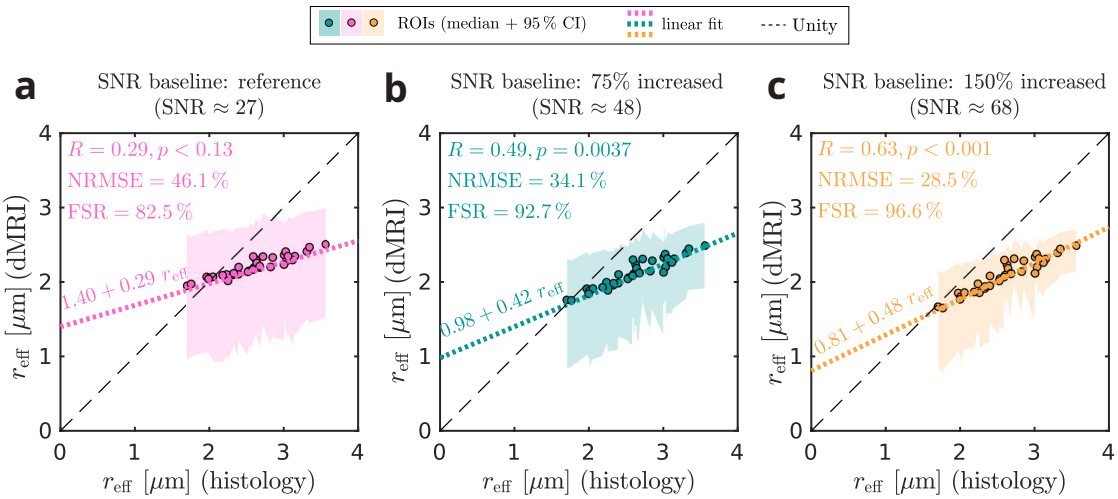

Figure 6.2: Optimal in vivo MRI protocols for clinical scanners. **(a-c)** Comparison of r_{eff} from dMRI simulations against histological values for next-generation clinical scanners across different SNR levels: **(a)** 27, **(b)** 48 and **(c)** 68. These protocols correspond to diamond markers in Figure 6.1. Markers correspond to histological ROIs in Figure 1.1f. The 95 % confidence intervals (shaded areas) were computed across 1000 noise realizations. Dashed lines illustrate theoretical perfect agreement, whereas dotted lines represent linear regressions. Annotated metrics include Pearson's correlation coefficient (R) and corresponding p-value, normalized root-mean-square error (NRMSE), and the fitting success rate (FSR) (see Section 8.8.1 for metric definitions).

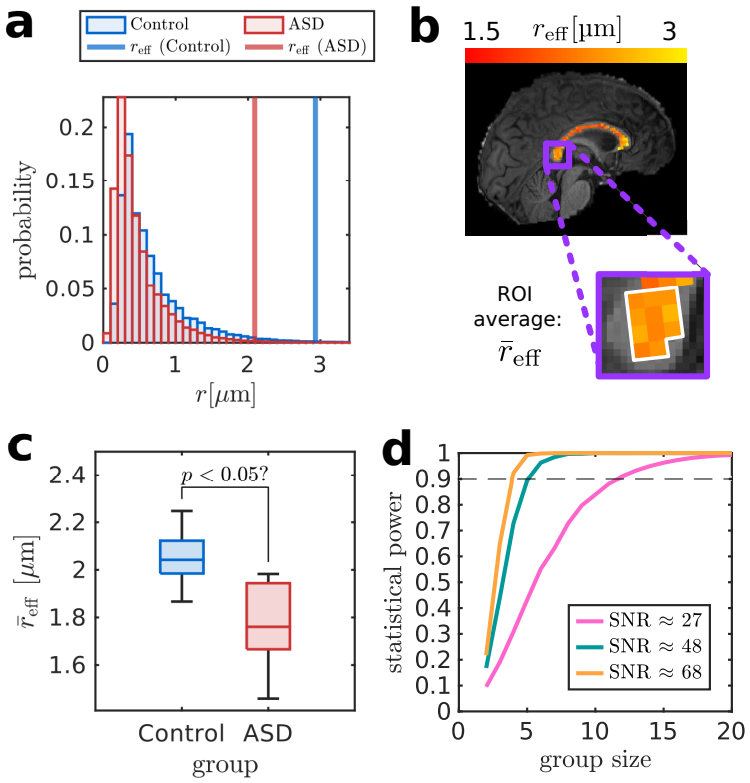

Figure 6.3: Simulation of clinical application for r_{eff} mapping. **(a)** Exemplary axon radius distributions in the splenium for subjects with autism spectrum disorder (ASD) and healthy controls, based on distributions from a splenium ROI in Figure 1.1f. ASD conditions were simulated by scaling down radii by 28.6 % [7], whereas distributions for healthy controls were used as is. **(b)** Illustration of subject-level mean r_{eff} in the splenium, denoted as $\bar{r}_{\text{eff}}$. Values were computed over 11 voxels, reflecting the average number of splenium voxels in the mid-sagittal slice in our in vivo dMRI subjects. **(c)** Illustration of one Monte Carlo iteration for statistical power estimation. We assessed group differences in $\bar{r}_{\text{eff}}$ between healthy and ASD subjects using a two-sample t-test ($\alpha = 0.05$) and approximated statistical power over 5000 Monte Carlo iterations as the fraction of tests that rejected the null hypothesis of equal means. **(d)** Statistical power as a function of the group size. Colors indicate optimal next-generation clinical scanner protocols for different SNR baseline levels determined in Figure 6.2. The dashed line indicates a typical statistical power target value of 0.9. We assumed equal group sizes.

6.3 Discussion

We investigated the clinical feasibility of in vivo dMRI-based axon radius mapping through data-driven protocol optimization anchored in histology-based simulations from two densely sampled human corpora callosa. We show that – when combined with substantial SNR gains – the proposed clinical scanner protocols may enable subject-level correlation with histology and support clinical applications, as illustrated in detecting axonal abnormalities in autism spectrum disorder (ASD) within feasible group sizes. Beyond the clinical scope, our broader evaluation across scanner types revisits the relationship between protocol performance and achievable diffusion gradient amplitude (g_{max}). While existing research primarily highlights the benefits of increasing g_{max} for precision in r_{eff}, our results highlight that the model-inherent bias simultaneously degrades accuracy, making it a relevant factor for protocol design.

Clinical adoption appears achievable but challenging

To date, r_{eff} mapping with dMRI has been largely confined to advanced research scanners with gradient amplitudes up to 300 mT/m – the same class of system on which we demonstrated group-level correlation between dMRI-based r_{eff} and histology (see Chapter 4). Conventional clinical scanners are limited to around 80 mT/m, but next-generation clinical systems now offer gradient amplitudes of up to 200 mT/m, substantially narrowing the gap. Our data-driven protocol optimization, grounded in histology-based simulations, suggests that these next-generation clinical scanners can approach the performance of research-grade systems, particularly when potential SNR improvements are factored in.

At a baseline SNR ≈ 27, reflecting our experimental conditions after adjusting for protocol differences, subject-level correlations with histology are unlikely to reach statistical significance. However, with a 75 % SNR increase (SNR ≈ 48), a significant correlation emerges ($R = 0.49$, $p = 3.7 \cdot 10^{-3}$). Further increases (SNR ≈ 68) could strengthen this association ($R = 0.63$, $p < 10^{-3}$), although such gains may exceed what is practically achievable. Overall, the SNR gains necessary to support subject-level correlations appear substantial, and these requirements may be even higher when unmodeled signal components reduce correlation strength or when the assumed Gaussian signal distributions cannot be enforced through advanced preprocessing techniques [104–106].

On the bright side, employing the latter technique could enable effective SNR gains through denoising, which we did not apply in our experiments or simulations, in order to preserve Rician-distributed signals for Rician ML fitting of powder-averaged signals [34]. Importantly, the identified model-inherent bias highlights a key target for future modeling advances that could help relax SNR demands. Recent developments also promise future SNR gains, e.g., a 30 % SNR gain was recently demonstrated using advanced acquisition techniques for the same in vivo protocol applied in our study [163]. Looking further ahead, improvements may arise from

ongoing innovations in coil design and gradient hardware [184, 185].

Hypothetical application in ASD illustrates potential clinical utility

Extending our simulations from technical feasibility to potential clinical utility, we explored how SNR advances could support applications of r_{eff} in neurological disorders. In a hypothetical clinical scenario, we estimated the group size requirements to distinguish individuals with ASD from healthy controls, based on an assumed 28.6 % reduction in axon radii in the mid-sagittal splenium [7]. Although this reduction was reported for the arithmetic mean axon radius, we applied it uniformly across all radii. This may, in fact, underestimate the effect size, as large axons – which disproportionately influence r_{eff} – appear particularly reduced in ASD subjects. Our simulations suggest that 12 subjects per group would be needed to achieve a statistical power target of 0.9 at SNR $\approx$ 27, while only six or fewer would be required at SNR $\geq$ 48. These modest numbers are enabled by spatial averaging across splenium voxels, which effectively boosts SNR – a strategy previously applied for r_{eff} mapping along white matter tracts [6]. However, we suggest that these results rather emphasize the strong positive impact of potential SNR gains rather than providing accurate estimates for the required group sizes, given that there are unmodeled variabilities such as scan-rescan variability [6, 163].

Model-inherent bias influences optimal protocol design

Expanding beyond clinical protocols, we provide broader insights into the design of in vivo r_{eff} measurements, exploring gradient amplitudes ranging from state-of-the-art clinical scanners with 80 mT/m to next-generation research systems with 500 mT/m. Previous studies have primarily evaluated scanner performance in terms of achievable precision as a function of gradient amplitude and noise [6, 14, 30, 42, 157]. In contrast, we assess accuracy alongside precision using a data-driven approach grounded in histology-based simulations, which allows us to implicitly capture the newly identified model-inherent bias. This bias increases with both gradient amplitude and r_{eff}, degrading absolute agreement as measured by normalized root-mean-square error (NRMSE). By contrast, higher gradient amplitudes tend to improve correlation (R) through improved precision, aligning with previous findings [6, 14, 30, 42, 157]. However, these gains in R become marginal for gradient amplitudes beyond 300 mT/m in regimes of high SNR and large r_{eff}, at the expense of reduced accuracy. This becomes particularly pronounced for next-generation research scanners with gradient amplitudes of 500 mT/m, suggesting that further improvements in modeling are required to fully harness the potential of these scanners.

Limitations and future directions

In addition to the fixed parameter choices discussed in Chapter 5, the simulations in this chapter assume Gaussian-distributed signals. This differs from the Rician-distributed signals, typical of magnitude dMRI [31], present in our experimental data in Chapter 4. While advanced preprocessing techniques exist that can effectively restore Gaussian-distributed complex dMRI signals [104–106], they are not yet widely adopted, particularly in clinical practice.

A core strength of our protocol design approach is its data-driven nature, grounded in a large histological dataset of the human corpus callosum. Rather than relying solely on theoretical considerations, this allows us to capture practical limitations such as the sensitivity reduction caused by model-inherent bias. Although the qualitative agreement between these simulations and experimental dMRI on research scanners (see Chapters 4 and 5) suggests that our simulations capture relevant effects, they do not account for all discrepancies, indicating that further improvements in specificity are needed. Hence, our optimized next-generation clinical scanner protocols represent only an initial step toward clinical translation and must be validated experimentally. In the absence of acquisition techniques that achieve the required SNR directly, a practical first step could involve averaging over repeated scans.

While our hypothetical application assumes that changes in r_{eff} reflect alterations in the underlying axon radius distribution, it remains unclear whether dMRI-derived r_{eff} is specific to such changes. Other morphological features commonly observed in pathological tissue – such as beadings, undulations, or branching – may also affect the diffusion signal and thereby influence r_{eff} [25, 26, 150]. Further research is needed to determine whether such effects can be disentangled and to evaluate the specificity and broader clinical utility of r_{eff} as a biomarker.

Conclusion

Our study outlines a pathway for translating axon radius mapping from advanced research scanners to clinical scanners. While experimental validation of the proposed clinical scanner protocols is a necessary next step, the suggested feasibility of r_{eff} mapping on clinical scanners encourages the exploration of potential clinical applications of r_{eff} as a biomarker, as exemplified by the autism spectrum disorder application shown here. Beyond the proposed specific clinical protocols, our insights into the impact of model-inherent bias on protocol design may help guide further methodological improvements or practical measurements under the current modeling constraints.

Chapter 7

General discussion

This thesis provides the first experimental evidence that in vivo dMRI-based estimates of the effective axon radius (r_{eff}) reflect anatomical variation in the human brain. Leveraging a novel light microscopy (LM) dataset that bridges the spatial scale gap between histology and dMRI, we demonstrate a significant group-level correlation between in vivo r_{eff} and histologically derived values in the corpus callosum. These findings are complemented by histology-informed simulations, which provide insight into the sensitivity and limitations of the current signal model and help define a path toward implementation on clinical scanners.

Quantitative evidence for anatomical validity in vivo

We provide the first quantitative evidence that in vivo dMRI-based r_{eff} captures anatomical variation in axon radius distributions, based on a significant group-level spatial correlation with histological values ($R = 0.41$, $p < 0.05$). This marks a shift from prior qualitative hints [6, 13, 15, 20, 42, 105, 146] to quantitative validation – a critical milestone. Mechanistically, it supports the feasibility of measuring r_{eff} as a genuine biophysical property with dMRI, despite evidence from 3D histology that real axons deviate from the idealized cylindrical model underlying r_{eff} [23, 25–28, 38, 148–150]. Biologically, r_{eff} reveals a coarse anterior–posterior gradient across the corpus callosum, partially consistent with earlier anatomical reports [4, 41, 147].

Scope and limits of in vivo validation

Despite the group-level correlation observed in vivo, most individual subjects do not show significant subject-level correlations. This may reflect the moderate overall sensitivity of the method, which is partly driven by a newly discovered model-inherent bias, reducing sensitivity to large r_{eff}. Beyond this bias, the substantial inter-individual variability observed in both in vivo dMRI and histology raises the question of whether fine-grained spatial patterns exist across individuals at all, or whether such patterns are merely misaligned between them.

More broadly, our demonstration of sensitivity does not imply specificity, as evidenced by persistent global offsets between histology, dMRI experiments, and simulations. Although we explore potential sources of these offsets through simulations, improving specificity in experimental data remains an open challenge and lies beyond the scope of this thesis, which focused on establishing the previously

unproven sensitivity of r_{eff} mapping in the human brain.

Large-scale 2D light microscopy as a scalable validation framework
Our light microscopy (LM) dataset addresses critical limitations in the histological validation of dMRI-based r_{eff}. First, it enables dense sampling within individual ROIs, capturing axon ensembles large enough to match the spatial scale of dMRI voxels. Second, it allows for high-throughput coverage across many ROIs. Together, these features allowed us to move beyond previous 2D histological efforts [4, 17, 38, 45] and enabled quantitative spatial correlation with dMRI-based r_{eff}.

Importantly, the observed correlation between in vivo dMRI-based r_{eff} and our histological values not only demonstrates the sensitivity of dMRI to r_{eff}, but also strengthens confidence in our 2D histological reference. This is noteworthy in the light of recent findings from 3D histology [23, 26, 148, 149], which show that real axons often deviate from the idealized cylinder shapes assumed in our histological analysis. Hence, until 3D histology becomes more practical at scale, our approach offers a scalable and effective framework for validating r_{eff}.

Ex vivo validation appears challenging
Ex vivo dMRI is often used as an intermediate step toward in vivo validation, as it enables histological comparison within the same tissue sample and thereby avoids inter-individual variability. However, in the context of r_{eff}, ex vivo validation appears inherently difficult. This is because the model-inherent bias, which already limits sensitivity under in vivo conditions, is further amplified under typical ex vivo tissue and scanning conditions. As a result, sensitivity in ex vivo human white matter is so low that there is little margin to detect correlations with the investigated experimental protocol – especially if additional unmodeled effects are present. One strong candidate is the immobile water compartment in fixed tissue [22], which introduces an extra parameter estimation step—along with its associated uncertainty—that is not required for in vivo modeling.

A path to clinical translation
Axon radius mapping has so far been limited to a few research scanners, as used in this thesis, with diffusion gradient amplitudes of at least 300 mT/m. While standard clinical systems (up to 80 mT/m) do not provide sufficient sensitivity to r_{eff}, new high-gradient clinical scanners—reaching up to 200 mT/m—are narrowing this gap.

Our histology-informed simulations suggest that clinical adoption of r_{eff} mapping may become feasible on these scanners, provided that substantial SNR gains on the order of 75 % can be achieved to support single-subject correlations between histological and dMRI-based r_{eff}. While challenging, several strategies may help meet this requirement, including advanced acquisition schemes [104–106, 163] and complex denoising [106, 186, 187], while further gains could come from hardware innovations [184, 185]. Moreover, the model-inherent bias we identified points to untapped sensitivity that advances in signal modeling may help unlock.

Encouragingly, if such SNR levels can be achieved, our simulations suggest that clinically meaningful applications based on r_{eff} may become feasible – illustrated

by a hypothetical case of distinguishing individuals with autism spectrum disorder (ASD) from controls.

Limitations and future directions

The observed in vivo correlation was derived from a single multimodal dataset. Given substantial variability across individuals and cohorts—such as the age difference between our histological (61 years) and in vivo (31 years) samples—replication on independent data is needed to confirm the robustness and generalizability of our findings.

While we optimized dMRI protocols for in vivo application, we did not attempt to improve protocols for ex vivo application. Given the important role of ex vivo validation as an intermediate step toward in vivo validation, optimizing such protocols should be a priority for future work.

Our r_{eff} estimates and simulations relied on fixed parameter assumptions from the literature, including axoplasmic diffusivity, compartmental volume fractions, and tissue shrinkage corrections. While these simplifications may introduce biases, we expect our correlation-based findings to remain qualitatively robust.

We conclude that large-scale 2D histology and emerging 3D histology offer complementary strengths: the former enables broad sampling across many axons, while the latter captures detailed along-axon morphology. Combining both modalities could enable more realistic simulation substrates and improved model validation.

Finally, while we identify the origin of the model-inherent bias, we do not propose methods to mitigate it. Future work should explore modeling advances to address this limitation, as doing so could unlock substantial sensitivity gains.

Conclusion

This work establishes a scalable framework for validating dMRI-based r_{eff} in the human brain. Building on this framework, we provide the first quantitative evidence that dMRI is sensitive to axon radius variation in the human brain. By combining large-scale histology data, experimental validation, and simulation-based analysis, we define the conditions under which r_{eff} mapping is feasible today and identify what is still missing for clinical adoption. At the same time, we identify a key limitation in current modeling, thereby highlighting an avenue toward realizing this goal.

Chapter 8

Materials and methods

This chapter details the materials and methods used throughout the thesis. Section 8.1 describes the ex vivo tissue samples and their preparation. The following sections describe the imaging and processing steps specific to each modality: microscopy, with a dedicated section on convolutional neural network (CNN) training for axon segmentation of microscopy data (Sections 8.2 and 8.3); in vivo dMRI (Section 8.4); and ex vivo dMRI (Section 8.5). Section 8.6 presents the framework used to conduct dMRI simulations based on axon radius distributions derived from the microscopy data. Finally, Sections 8.7 to 8.10 outline analyses specific to the individual Chapters 3 to 6.

8.1 Tissue samples

We used six ex vivo human white matter samples from distinct donors: three from the corpus callosum and one each from the optic chiasm, corticospinal tract, and anterolateral system. The entire procedure of case recruitment, acquisition of the patients' personal data, the protocols and the informed consent forms, performing the autopsy and handling the autopsy material has been approved by the responsible authorities (Approval #205/17-ek and WF-74/16).

In total, we prepared 48 ROIs for imaging with light microscopy (LM), 6 with electron microscopy (EM), and 15 with ex vivo dMRI. Table 8.1 summarizes tissue sample and ROI information, whereas Figure 1.1e-f illustrates ROI locations in the corpus callosum samples.

Cross-modality correspondences

While all ROIs were imaged with LM, the ROIs imaged with EM and ex vivo dMRI formed subsets of the LM ROIs, enabling cross-modality comparisons.

For EM, we imaged six ROIs of CC-01. Each ROI was represented by a single tissue block, from which we cut adjacent sections for LM and EM. The separation between the LM and EM imaging planes within a block was at most 100 µm (see Figure 8.1a).

For ex vivo dMRI, we imaged 15 ROIs of CC-02. Before histological preparation, we bisected the corpus callosum along the mid-sagittal plane, yielding hemispheric

sections. We placed LM ROIs close to the cutting plane so that we could define corresponding ROIs in the contralateral ex vivo dMRI hemisphere (see Figure 8.1b).

Tissue preparation

We first immersion-fixed tissue samples in 3 % paraformaldehyde and 1 % glutaraldehyde in phosphate-buffered saline (pH 7.4).

For ROIs used for microscopy imaging (LM or EM), we extracted tissue blocks of 1 to 4 mm edge length and applied a preparation protocol typically used for EM: contrasting with osmium tetroxide and uranyl acetate, dehydration in graded acetones, and embedding in Durcupan resin. This ensured structural preservation and cross-modality comparability. For LM imaging, we then cut semi-thin sections (≈ 500 nm thickness) covering 8 mm^2 on average, mounted them on Thermo Scientific SuperFrost Plus glass slides, stained them with 1 % toluidine blue, air dried, and coverslipped them with Sigma-Aldrich Entellan toluene. For EM imaging, we cut ultrathin sections (≈ 50 nm thickness) covering 120^2 μm^2 on average.

For ex vivo dMRI, we cut the corpus callosum hemisphere dedicated for imaging into five segments along the anterior–posterior axis (see Figure 8.1b) using a Reichert Ultracut II and embedded the segments in 1.5 % low-melting agarose in phosphate-buffered saline in a custom-made container.

Table 8.1: Tissue sample information. The following tissue samples were investigated: three corpus callosum (CC) samples, a corticospinal tract (CST), an optic chiasm (OC), and an anterolateral system (AS). Six ROIs in CC-01 were spatially matched between LM and EM (see Figure 8.1a). ROIs in CC-02 were spatially matched between LM and ex vivo dMRI (see Figure 8.1b), with one genu ROI missing in ex vivo dMRI. Abbreviations: PMD – postmortem delay, the time between death and tissue fixation.

Sample	Sex	Age [years]	PMD [hours]	Cause of death	Modality	ROIs	Application
OC	m	59	48	multi organ failure	LM	1	CNN training/validation
CST	f	89	24	heart failure	LM	1	CNN training/validation
AS	m	81	24	multi organ failure	LM	1	CNN training/validation
CC-01	m	74	24	multi organ failure	LM	4	CNN training/validation
					LM	6	CNN test
					EM	6	CNN test
CC-02	m	61	20	myocardial infarction	LM	16	Experimental validation
					dMRI	15	Experimental validation
CC-03	f	60	24	multi organ failure	LM	19	Experimental validation

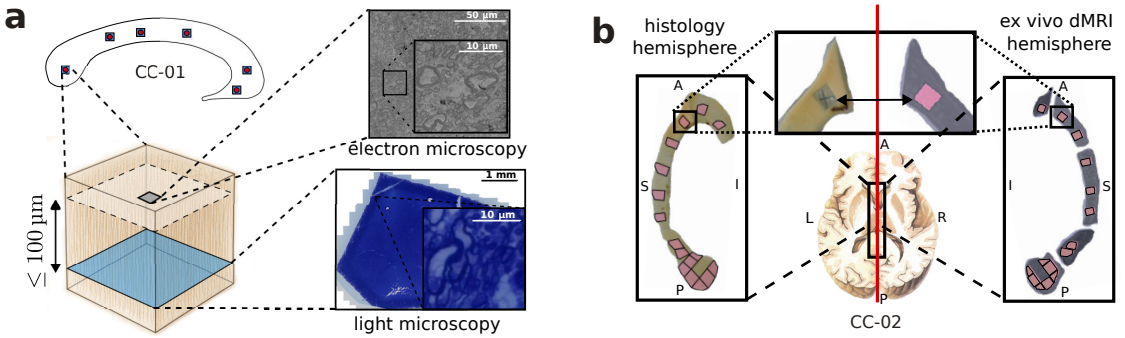

Figure 8.1: Cross-modality correspondence in ex vivo tissue. **(a)** Illustration of spatially matched ROIs between light microscopy (LM) and electron microscopy (EM) for six ROIs of CC-01. These ROIs were used to test the performance of our LM-based axon radius estimation pipeline. Using the tissue block of the same ROI, we cut sections for LM (blue plane) and EM (gray plane) within 100 µm distance, with the same bundle of axons (thin lines) passing through both image planes. **(b)** Illustration of spatially matched ROIs between LM and ex vivo dMRI for CC-02. We bisected the brain along the mid-sagittal plane, indicated by the red line, yielding hemispheric sections for LM (left) and ex vivo dMRI (right). We first defined LM ROIs near the mid-sagittal plane; then, we manually defined corresponding ROIs in ex vivo dMRI. Magnified views illustrate an example of matching ROIs in LM and ex vivo dMRI (extracted tissue area in histology and magenta area in ex vivo dMRI). Note that the genu was only partially scanned with ex vivo dMRI (anterior segment).

8.2 Microscopy

Electron microscopy

We acquired six EM images, one for each CC-01 ROI shown in Figure 8.1a, using a Zeiss LEO EM 912 Omega TEM operated at 80 kV. We recorded digital micrographs with a dual-speed 2K on-axis charge-coupled device (CCD) camera coupled to a yttrium aluminum garnet scintillator (TRS-Tröndle) at a pixel size of 0.0043 µm and a resolution limit of 4 nm.

Light microscopy

We acquired 48 LM images, one for each ROI listed in Table 8.1, using a Zeiss AxioScan Z1 with a 40× objective (numerical aperture 0.95; resolution limit 292 nm) in brightfield mode. Images were sampled at 0.1112 µm/pixel[a].

Axon radius estimation on light microscopy

We estimated axon radii in three steps: semantic segmentation, instance segmentation, and radius approximation (see Figure 3.1). First, we performed semantic segmentation to classify each pixel as axon, myelin, or background using a convolutional neural network (CNN) applied in a sliding-window manner (see Figure 3.1a). The architecture and training of this CNN are detailed in a dedicated section (see Section 8.3). Next, we identified individual axons by applying connected component

[a]The effective resolution is limited by the objective to ∼ 292 nm despite finer pixel sampling.

labeling [65] (see Figure 3.1b). Finally, we approximated the radius of each axon using the circular equivalent area method (see Figure 3.1c), yielding empirical axon radius distributions (see Figure 3.1d).

8.3 Convolutional neural network training

This section describes the convolutional neural network (CNN) and its training used for the semantic segmentation step of our axon radius estimation pipeline on LM images (see Figure 3.1a).

Training data annotation

For CNN training, we manually annotated 64 LM subsections drawn from 7 ROIs dedicated to the training (see Table 8.1), with subsection sizes ranging from $70 \times 70\,\mu m^2$ to $120 \times 120\,\mu m^2$. In particular, we annotated 46 subsections of CC-01, four from the optic chiasm, four from the corticospinal tract, and 10 from the anterolateral system. Within some subsections, we labeled only a subset of pixels and assigned an "ignore" label to the remaining pixels, which were excluded during training. We adopted this strategy to prioritize (i) capturing a diverse range of axon shapes and staining contrasts across many subsections, and (ii) ensuring inclusion of large axons, given their disproportionate influence on r_{eff}.

We followed the annotation procedure described by Zaimi et al. [151], first outlining the myelin sheath and then filling in the axonal interior. At later stages, we used a prototype CNN to generate preliminary annotations, which were manually refined. We carried out annotation using GIMP [188] or ITK-SNAP [189] by six trained raters, all instructed by experts (M. Morawski and M. Morozova).

Network architecture

We used a CNN based on the U-Net architecture [75, 190] with an EfficientNet-B3 encoder pretrained on ImageNet [191, 192] (see Figure 8.2). The encoder–decoder structure followed the typical U-Net design of downsampling and upsampling paths connected via skip connections. In the decoder, we used standard convolution blocks combined with batch normalization, rectified linear unit (ReLU) activations [72], and squeeze-and-excitation (scSE) modules [193]. The final output layer applied a softmax activation to generate pixel-wise probabilities for axon, myelin, and background. The network had approximately 3.8 million trainable parameters.

Input preprocessing

We normalized input images by subtracting the per-channel mean and dividing by the corresponding standard deviation, computed across the entire training dataset.

Input augmentation

We applied data augmentation on-the-fly during training using *imgaug* [194], including the following transformations:

- adjustments to hue, saturation, and value in HSV color space
- contrast modification

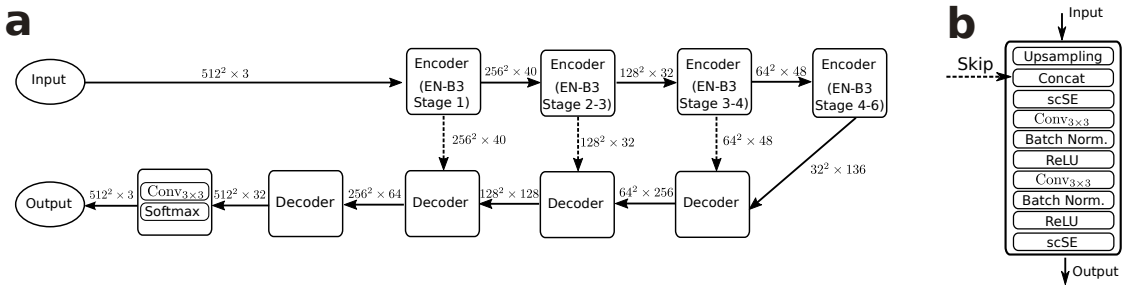

Figure 8.2: Semantic segmentation network architecture. **(a)** Overview of the U-Net [75] architecture used for segmenting axons, myelin, and background. The encoder (top path) is a pretrained EfficientNet-B3 [191], and the decoder (bottom path) follows the standard U-Net design with skip connections (from top to bottom) between matching resolutions. Annotated numbers denote spatial resolution and the number of channels. **(b)** Decoder block. Applied are nearest-neighbor upsampling, concatenation of encoder features, and two consecutive blocks of: a 3×3 convolution with batch normalization and rectified linear unit (ReLU) activation [72]. Finally, a squeeze-and-excitation (scSE) module [193] is used and a softmax activation is applied to yield pixel-wise class probabilities.

- Gaussian blurring
- horizontal and vertical flipping
- affine transformations (scaling: $[0.8, 1.2]$, rotation: $[-45°, 45°]$, shearing: $[-25°, 25°]$)
- staining augmentation based on [195, 196]

Hyperparameter optimization

We optimized the initial learning rate, learning rate decay factor γ, and the number of epochs of 150 randomly sampled training patches[a] using a grid search with Optuna [197] in a 4-fold cross-validation setup across the 64 LM training subsections. As a target metric, we used the mean Dice score (see Equation (2.12)) for axon and myelin classes, evaluated every 10 epochs on the validation data from the respective fold. Each model was trained for at least 150 epochs. To mitigate overfitting, training was stopped early if the target metric did not improve for three consecutive validation steps (i.e., 30 epochs). Final hyperparameters were selected to maximize the average target metric across all CV folds.

Training the final model

Using the selected hyperparameters, we trained the final model for 200 epochs. We performed training using mini-batch gradient descent with a batch size of 4, Nesterov momentum (0.95) [80], an initial learning rate of 10^{-2}, and a decay factor $\gamma = 0.2$ applied every 50 epochs after the initial 100 epochs, minimizing a Lovàsz-softmax loss [198]. We trained the model end-to-end, with all weights updated. Training took approximately 45 minutes on an NVIDIA Quadro RTX 6000 GPU. We used a PyTorch-based framework [199, 200] for the entire training workflow.

[a]We use "epoch" to denote a fixed number of resampled, augmented patches rather than a strict full pass over unique samples.

8.4 In vivo diffusion MRI

Subjects

We recruited five healthy adult subjects (age: 31 ± 3 years, representing mean $\pm$ standard deviation; sex: two male, three female). The subjects were scanned under the approval of the Ethics Commission of the Medical Faculty of Leipzig University (reference number 293/18-ek). The participants gave written informed consent before participation in the study.

Image acquisition

We acquired magnitude dMRI data using a 32-channel receive coil and 300 mT/m gradient coils on a Siemens Connectom 3T scanner at the Max Planck Institute for Human Cognitive and Brain Sciences in Leipzig, Germany. We followed the dMRI protocol described by Veraart et al. [6]. Briefly, we used a single-shot multi-band EPI sequence (multi-band factor: 2) with blipped-CAIPI [201](Controlled Aliasing in Parallel Imaging) and in-plane GRAPPA (GeneRalized Autocalibrating Partial Parallel Acquisition) acceleration (acceleration factor: 2) [202, 203]. We applied diffusion-weighting with the following fixed parameters: $\delta = 15$ ms, $\Delta = 29.25$ ms, TE = 66 ms, TR = 3500 ms, matrix size of 88×88 with 54 slices, and isotropic voxel edge length of 2.5 mm. We varied the diffusion weighting across five $b = (0.5, 1, 2.5, 6, 30.45)$ ms/µm^2. For each b, we acquired $(30, 30, 30, 60, 120)$ gradient directions isotropically distributed on a sphere [204], with corresponding gradient amplitudes $g = (36, 51, 80, 124, 279)$ mT/m.

For geometric susceptibility correction, we acquired 23 non-diffusion-weighted images interleaved with the diffusion-weighted acquisition, along with 10 images with reverse phase encoding. Additionally, we acquired T1-weighted MP-RAGE (Magnetization Prepared – Rapid Gradient Echo) images [205]. The total scan time, including non-diffusion-weighted and diffusion-weighted MRI, was 25 min.

Preprocessing

We corrected for Gibbs ringing artifacts (using *MRtrix3 mrdegibbs* [112, 206]), susceptibility distortions, eddy current distortions, and motion artifacts (using *MRtrix3 dwifslpreproc* [113, 115, 206, 207]), and gradient nonlinearity distortions (using *gradunwarp* [118, 119]). We did not correct for gradient nonlinearity effects on b, as our analysis focused on the corpus callosum, a region close to the isocenter where these effects are expected to be small [120].

Parameter estimation

For $b \leq 2.5$ ms/µm^2, we estimated the noise level σ using Marchenko-Pastur principal component analysis prior to preprocessing (using *MRtrix3 dwidenoise*[a] [186, 187, 206]). After preprocessing, we estimated the diffusion tensor $\mathbf{D}$ (see Equation (2.29)) using diffusion kurtosis imaging (DKI) and mapped fractional anisotropy (FA) (using *MRtrix3 dwi2tensor* and *tensor2metric* [122, 125, 206, 208]).

[a]We discarded the denoised images and kept only the σ map.

For $b \geq 6\,\mathrm{ms/\mu m^2}$, we estimated powder-averaged signals $S^\circ(b)$ as the zeroth-order spherical harmonic using an estimator of the even-order spherical harmonic coefficients up to the sixth order (using the *Standard Model Imaging (SMI) Toolbox* [48, 209, 210]). Specifically, we determined the spherical harmonics basis functions and estimated the coefficients using a Rician maximum likelihood (ML) estimator [34], which relied on the σ maps. Finally, we estimated r_{eff} using Equations (2.49) and (2.50), assuming $D_0 = 2.07\,\mathrm{\mu m^2/ms}$ [128] and $f_{\mathrm{im}} = 0$ [172].

8.5 Ex vivo diffusion MRI

Image acquisition

We acquired magnitude dMRI data of CC-02 (see Figure 1.1f and Figure 8.1b) using a Bruker Biospin 9.4T scanner with a single-channel transceiver volume coil and a gradient insert coil with a maximum gradient amplitude of 1500 mT/m at the Berlin Ultrahigh Field Facility in Berlin, Germany. We followed a protocol similar to that suggested by Veraart et al. [15] for ex vivo r_{eff} mapping in rats. Briefly, we applied diffusion-weighting for 65 gradient directions using a multi-shot EPI sequence with four segments and the following fixed parameters: $\delta = 7\,\mathrm{ms}$, $\Delta = 20.1\,\mathrm{ms}$, $\mathrm{TE} = 34.7\,\mathrm{ms}$, $\mathrm{TR} = [15000, 25000]\,\mathrm{ms}$ (depending on the size of the tissue segment, see Figure 8.1b), and isotropic voxel edge length of 0.35 mm. For different tissue segments, the field-of-view was adjusted between $22 \times 28 \times 9\,\mathrm{mm^3}$ and $25 \times 30 \times 10.5\,\mathrm{mm^3}$. We varied b between 2.5 and $100\,\mathrm{ms/\mu m^2}$, and g between 200 and 1278 mT/m, as detailed in Table 8.2. To enhance SNR, we averaged repeated measurements prior to image reconstruction for higher b-values, as shown in the *Repetitions* column of Table 8.2.

Preprocessing

We corrected for Gibbs ringing artifacts (using *MRtrix3 mrdegibbs* [112, 206]). To account for signal drift across b-shells, we normalized images within each b-shell to an S_0, using a non-diffusion-weighted image acquired at the start of acquisition for that shell.

Parameter estimation

Per b, we estimated the noise level σ using Marchenko-Pastur principal component analysis prior to preprocessing (using *MRtrix3 dwidenoise*[a] [186, 187, 206]). Then, we estimated powder-averaged signals $S^\circ(b)$ as the zeroth-order spherical harmonic using an estimator of the even-order spherical harmonic coefficients up to the sixth order (using the *Standard Model Imaging (SMI) Toolbox* [48, 209, 210]). Specifically, we determined the spherical harmonics basis functions and estimated the coefficients using a Rician ML estimator [34], which relied on the b-dependent σ maps.

For $b \leq 10\,\mathrm{ms/\mu m^2}$, we estimated the main fiber orientation $\bar{\mathbf{n}} \in \mathbb{R}^3$, with the σ

[a]We discarded the denoised images and kept only the σ map.

Table 8.2: Ex vivo dMRI acquisition parameters. *Repetitions* denotes the number of repeated measurements per diffusion gradient direction, which were averaged in k-space prior to image reconstruction.

b [ms/µm^2]	g [mT/m]	Repetitions
2.5	200	1
5.0	283	1
7.5	347	1
10.0	401	1
20.0	567	2
30.0	695	2
40.0	802	3
50.0	896	3
60.0	982	4
70.0	1061	5
80.0	1134	6
90.0	1203	7
100.0	1278	8

map for $b = 2.5\,\text{ms/µm}^2$ provided as additional input (using the *NODDI*[a] *matlab toolbox*[108, 211]).

For $b \geq 20\,\text{ms/µm}^2$, we estimated r_{eff} from $S^\circ(b)$ using Equations (2.38) and (2.49) via non-linear fitting [133], assuming $D_0 = 0.35\,\text{µm}^2\text{/ms}$ [212]. We expected a non-negligible contribution of the immobile water fraction f_{im} (see Section 2.3.6.3) and estimated it from strongly decayed directional signals. Specifically, we selected signals from the highest b-shell with high alignment between $\mathbf{g}$ and $\bar{\mathbf{n}}$ (angle $\leq 20°$), fitted a Rician distribution, and approximated f_{im} by its expected value.

8.6 Diffusion MRI simulations

To place the experimental dMRI results from Sections 8.4 and 8.5 into a model-based context, we mirrored the experimental protocols and conditions with realistic simulations grounded in histological axon radius distributions. First, we generated one tissue substrate per histology ROI (see Figure 8.3) and simulated diffusion-weighted signals $S(b, \mathbf{g})$ relative to the non-diffusion-weighted reference S_0 using the three-compartment model in Equation (2.51). Then, we applied the same powder-averaging and r_{eff} estimation pipeline as for experimental data. The following paragraphs describe the simulation approach in detail, and Table 8.3 summarizes all parameters.

[a] *Neurite Orientation Dispersion and Density Imaging*, a variant of the standard white matter model (see Section 2.3.6.1) with fixed diffusivity assumptions.

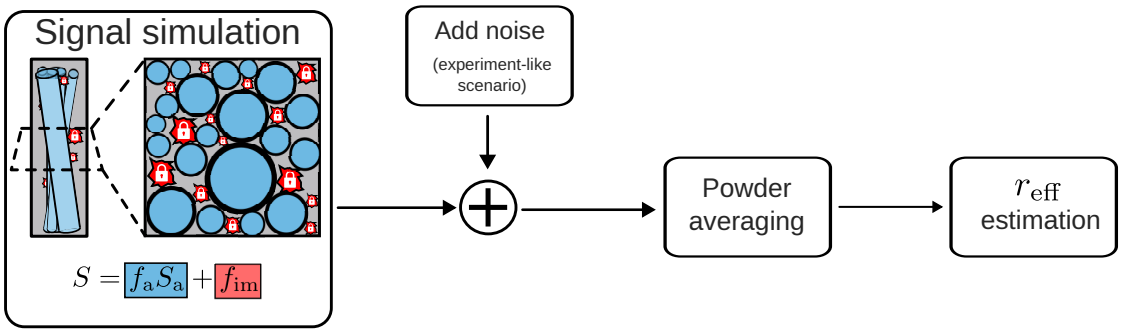

Figure 8.3: Schematic of diffusion MRI simulations. We modeled the tissue substrate using histologically derived axon radius distributions (blue cylinders and circles). Each substrate was based on one axon radius distribution from histological ROIs in Figure 1.1f. The signal included intra-axonal contributions (S_a) and, for ex vivo only, an immobile water fraction (f_{im}). We neglected the extra-axonal signal (S_e) but retained a nonzero signal fraction ($f_e > 0$) to keep compartment fractions realistic. To mimic experimental conditions, we added Rician noise (in vivo: SNR = 32; ex vivo: b-dependent SNR = 17 to 51). We then performed powder-averaging and estimated r_{eff} using the same pipeline as for experimental data (see Sections 8.4 and 8.5).

Intra-axonal signal

We factorized the intra-axonal signal in Equation (2.36) into a product of parallel and perpendicular components [213]:

$$S_a(b,\mathbf{g}) \approx \int_{|\mathbf{n}|=1} \Psi(\mathbf{n}) \underbrace{e^{-(\mathbf{g}\cdot\mathbf{n})^2 b D_a^{\parallel}}}_{S_a^{\parallel}(b,\mathbf{g},\mathbf{n})} \underbrace{\left[\frac{\int_0^\infty H(r)\, r^2\, S_{cyl}(b,\mathbf{g},\mathbf{n},r)\, dr}{\int_0^\infty H(r)\, r^2\, dr}\right]}_{S_a^{\perp}(b,\mathbf{g},\mathbf{n})} d\mathbf{n}. \tag{8.1}$$

We simulated $S_a^{\parallel}(b,\mathbf{g},\mathbf{n})$ using a literature value for $D_a^{\parallel}$ (see Table 8.3) and computed $S_a^{\perp}(b,\mathbf{g},\mathbf{n})$ as a volume-weighted average over histological axon radius distributions $H(r)$ (analogously to Equation (2.43)). For in vivo simulations, we scaled histologically-derived r by 1.3 to compensate for tissue shrinkage [17, 167]. We discretized the radius r into non-uniform bins with edges $(0, 0.1, \ldots, 5, 5.2, \ldots, 10, 10.5, \ldots, 20)$. For each bin, we simulated $S_{cyl}(b,\mathbf{g},\mathbf{n},r)$ using the matrix method (see Appendix A), which is not limited to the Gaussian phase approximation (GPA). Specifically, we used the MISST (Microstructure Imaging Sequence Simulation Toolbox [214, 215]) implementation of the matrix method with modifications for the rectangular PGSE waveform [216]. The rectangular waveform assumes infinitely fast gradient ramp-up (infinite slew rate), whereas real scanners impose finite slew rates.

Extra-axonal signal

We assumed a fully decayed extra-axonal signal ($S_e(b,\mathbf{g}) = 0$) but retained a nonzero f_e to prevent artificial inflation of f_a or f_{im}, which would otherwise lead to an effective overestimation of SNR.

Immobile water
In ex vivo simulations, we included an immobile water fraction $f_{\text{im}} = 0.27$ (estimated from data; see Section 8.5). For in vivo simulations, we set $f_{\text{im}} = 0$, assuming negligible contribution [172].

Fiber orientation dispersion
We modeled a single fiber bundle oriented along the main fiber direction $\bar{\mathbf{n}} = [0, 0, 1]^\top$ and drew orientations $\mathbf{n}$ from the Watson distribution [217], which we used as the orientation distribution function (ODF) $\Psi(\mathbf{n})$. The neurite dispersion (concentration) parameter $\kappa = 8.2$ was estimated from our experimental in vivo dMRI data using NODDI [108, 211]. We performed the integration over $\mathbf{n}$ using Lebedev quadrature of degree 590 [218, 219].

Simulation scenarios
We simulated two scenarios:

- *Idealized*: noise-free simulations to isolate model-inherent effects.
- *Experiment-like*: simulations with Rician noise (in vivo SNR = 32; ex vivo SNR = 17 to 51). We repeated each simulation 1000 times to quantify variability and precision.

While these scenarios were designed to closely mirror our experimental data (Sections 8.4 and 8.5), we introduce further targeted simulations within this framework in Sections 8.9 and 8.10.

Estimation of r_{eff}
We estimated r_{eff} using the same pipeline as for the experimental data. We fitted the powder-averaged signals while assuming known f_{im}. For noise-free data, we used a Gaussian ML estimator; for noisy data, we used a Rician ML estimator [34].

Table 8.3: MRI Simulation Parameters. Annotations denote:
[1] estimated as the mean of previously reported values [17, 167];
[2] estimated from our experimental data;
[3] parameters of our experimental protocols;
[4] we assumed $D_0 = D_{\mathrm{a}}^{\parallel}$;
[5] reported by West et al. [212];
[6] reported by Veraart et al. [128];
[7] reported by Tax et al. [172];
[8] computed as $f_a = f_0 e^{-\mathrm{TE}/T_{2,\mathrm{a}}} / (f_0 e^{-\mathrm{TE}/T_{2,\mathrm{a}}} + (1 - f_0 - f_{\mathrm{im}}) e^{-\mathrm{TE}/T_{2,\mathrm{e}}} + f_{\mathrm{im}})$ where f_0 is the non-T_2-weighted intra-axonal water fraction and f_{im} includes the T_2-related decay at experimental TE;
[9] computed as $f_{\mathrm{e}} = 1 - f_{\mathrm{a}} - f_{\mathrm{im}}$;
[10] we extrapolated $T_{2,a}$ and $T_{2,e}$ values from a 3 T scanner [128] to 9.4 T by scaling with a conversion factor $T_2(9.4\,\mathrm{T})/T_2(3\,\mathrm{T}) \approx 30\,\mathrm{ms}/83.8\,\mathrm{ms} \approx 0.358$ using literature values [220, 221].

Parameter	Symbol	Unit	Ex vivo value	In vivo value
Signal-to-noise ratio	SNR	-	32^2	$[17, 51]^2$
Radius scaling factor	-	-	1.0	1.3^1
Neurite dispersion	-	-	8.2^2	8.2^2
Diffusion shells	-	-	9^3	2^3
Gradient directions per shell	-	-	65^3	$(60, 120)^3$
Axoplasmic diffusivity	D_0	µm^2/ms	0.35^4	2.07^4
Parallel intra-axonal diffusivity	$D_{\mathrm{a}}^{\parallel}$	µm^2/ms	0.35^5	2.07^6
Minimum b	$b_{\min}$	ms/µm^2	20^3	6^3
Maximum b	$b_{\max}$	ms/µm^2	100^3	30.45^3
Minimum g	$g_{\min}$	mT/m	200^3	124^3
Maximum g	$g_{\max}$	mT/m	1278^3	279^3
Diffusion gradient time	δ	ms	7^3	15^3
Diffusion gradient separation	Δ	ms	20.1^3	29.25^3
Intra-axonal water fraction	f_0	-	0.41^6	0.41^6
Immobile water fraction	f_{im}	-	0.27^2	0^7
T_2-weighted intra-axonal signal fraction	f_{a}	-	0.58^8	0.58^8
T_2-weighted extra-axonal signal fraction	f_{e}	-	0.15^9	0.42^9
Extra-axonal signal	S_{e}	-	0	0
Intra-axonal transverse relaxation time	$T_{2,\mathrm{a}}$	ms	29.4^{10}	82^6
Extra-axonal transverse relaxation time	$T_{2,\mathrm{e}}$	ms	15.8^{10}	44^6
Echo time	TE	ms	34.7^3	66^3

8.7 Analyses for Chapter 3: A histological reference for MRI-based axon radius mapping

8.7.1 Segmentation metrics

Image-level segmentation performance
To assess how well the CNN trained in Section 8.3 segments axons, we treated the task as a binary pixel-wise classification, distinguishing axons from non-axonal structures (myelin and background). We compared the CNN segmentations against manual annotations on 30 small LM subsections (see Figure 8.4) and evaluated segmentation using the metrics defined in Equations (2.9) to (2.12).

Per-axon segmentation performance
Because the ensemble metrics (r_{eff} and r_{arith}) assessed in our work are sensitive to specific axon size regimes, we further analyzed segmentation performance as a function of axon size. Following Abdollahzadeh et al. [158], we matched each annotated axon to the predicted axon with the highest pairwise Dice score (see Equation (2.12)), enforcing a one-to-one correspondence. Annotated axons with no overlap to any prediction (Dice = 0) were counted as false negatives, while predicted axons without a corresponding annotation were counted as false positives.

8.7.2 Axon radius estimates at MRI scale

To assess the ability of our method to represent r_{eff} and r_{arith} at a scale relevant for dMRI, we evaluated both metrics in LM subsections that match the spatial scale of the ex vivo dMRI voxels used in this thesis (field-of-view: $350\,\mu\text{m} \times 350\,\mu\text{m}$; see Figure 8.5a–b). Specifically, we applied our axon radius estimation pipeline (see Figure 3.1) on 18 LM subsections, with three selected from each test ROI of CC-01 (see Figure 8.1a and Table 8.1). To generate reference values for r_{eff} and r_{arith}, we used manual annotations on these LM subsections and additionally included annotations from smaller EM subsections cut in close spatial proximity with a plane-to-plane distance of at most $100\,\mu\text{m}$ between LM and EM (see Figure 8.5a). The detailed approach for computing reference r_{eff} and r_{arith} values, along with the quantitative metrics evaluated, is outlined below.

Reference for r_{arith}
We computed reference values for r_{arith} from EM-based axon radius distributions (see Figure 8.5c), assuming that EM best captures the most relevant parts of the axon radius distribution for the frequency-weighted r_{arith}, including small axons ($r < 0.3\,\mu\text{m}$) that LM cannot resolve.

Reference for r_{eff}
Since r_{eff} is highly sensitive to the tail of the axon radius distribution, it is essential to assess large fields-of-views of LM to robustly sample the sparsely occurring large axons. To make manual annotation tractable, we annotated large axons ($r \geq 1.6\,\mu\text{m}$)

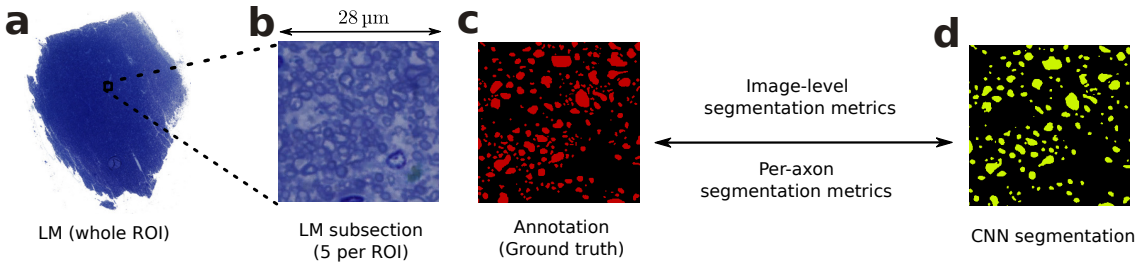

Figure 8.4: Evaluation of segmentation performance. **(a)** Whole light microscopy (LM) section of an exemplary ROI. **(b)** Exemplary LM subsection from the ROI in (a). **(c–d)** Segmentation of the LM subsection in (b) into axons (red, yellow) and background (black) for: **(c)** manual annotation (ground truth) and **(d)** convolutional neural network (CNN) segmentation. We quantitatively compared the CNN segmentation (d) to the manual annotation (c) using both image-level and per-axon segmentation metrics, as defined in Equations (2.9) to (2.12) and Section 8.7.1. The analysis included 30 LM subsections in total (five per ROI in Figure 8.1a).

in the LM subsections and captured the distribution of smaller axons ($r < 1.6\,\mu\text{m}$) from the smaller EM subsections. Due to differing axon counts between EM and LM subsections, we applied a scaling factor f when combining axon counts to synthesize a unified axon radius distribution:

$$n_{\text{eff},k} = \begin{cases} f \cdot n_{\text{EM},k}, & \text{for bins } k \text{ with bin radius } r_k < 1.6\,\mu\text{m}, \\ n_{\text{LM},k}, & \text{for bins } k \text{ with bin radius } r_k \geq 1.6\,\mu\text{m}. \end{cases} \tag{8.2}$$

Here, $n_{\text{EM},k}$ and $n_{\text{LM},k}$ denote the counts in EM and LM subsections for the k-th bin. Because there was no single correct choice for f, we computed both a lower and an upper bound (see Figure 8.6 for an illustration). As a lower bound, we used the ratio of LM-resolvable axons ($r \geq 0.3\,\mu\text{m}$) in LM and EM. This reflects our expectation that the CNN is more likely to underestimate than overestimate axon counts. As an upper bound, we used the ratio of subsection areas in LM and EM, acknowledging that EM subsections were hand-picked for high axon density and excluded large non-fiber structures such as blood vessels.

Evaluation metrics

To quantify the agreement between estimates ($\hat{r}_{\text{arith},i}$) and reference values ($r_{\text{arith},i}$), we computed bias using the normalized mean bias error

$$\text{NMBE} = \frac{\frac{1}{N}\sum_{i=1}^{N}(\hat{r}_{\text{arith},i} - r_{\text{arith},i})}{\frac{1}{N}\sum_{i=1}^{N} r_{\text{arith},i}}, \tag{8.3}$$

and precision using the coefficient of variation

$$\text{CoV} = \frac{\text{std}(\hat{r}_{\text{arith},i})}{\frac{1}{N}\sum_{i=1}^{N} r_{\text{arith},i}}, \tag{8.4}$$

where std(·) denotes the standard deviation across N subsections. For r_{eff}, we computed the same metrics separately for the axon radius distributions synthesized using the lower and upper bounds of f, yielding lower and upper estimates for the metrics above.

8.7.3 Staining as a confounder

We assessed whether spatial variation in image intensity, e.g., due to staining heterogeneity, confounds the mapping of r_{eff} and r_{arith}. To this end, we computed their spatial Pearson's correlations (R) with the grayscale-converted image intensity across whole LM ROIs, analogously to the use of Pearson's correlation coefficient defined in Equation (8.7). We performed this analysis on a $350 \times 350\,\mu\text{m}^2$ grid, where each grid cell provided a local sampling area for estimating r_{eff}, r_{arith}, and mean image intensity. We restricted this analysis to four of the six test ROIs of CC-01 (see Figure 8.1a and Table 8.1) with similar r_{eff} and r_{arith} values.

8.7.4 Establishing a reference for MRI validation

We applied our LM axon radius estimation pipeline (see Figure 3.1) to all ROIs of CC-02 and CC-03 (see Figure 1.1f) to generate a new histological reference dataset for MRI-scale axon radius distributions and r_{eff} in the human corpus callosum. To assess whether the larger ROIs improve bias and precision in r_{eff} compared to existing 2D histology datasets [4, 17, 38, 45], we used our LM-based axon radius distributions as a baseline and simulated smaller ROIs via subsampling. Specifically, we drew 1000 subsamples per ROI size, with sizes ranging from 10^2 to 10^5 axons, and computed the sampling distribution of r_{eff}. For each subsample size, we assessed bias and precision across all ROIs following Equations (8.3) and (8.4).

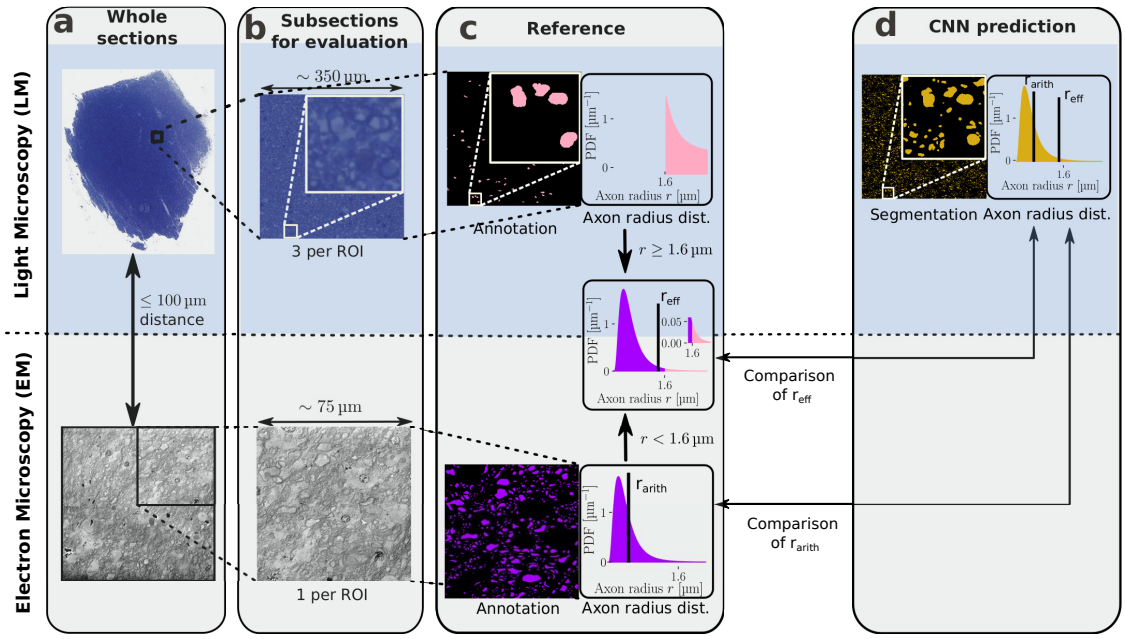

Figure 8.5: Evaluation of r_{eff} and r_{arith} estimation at dMRI scale. **(a)** Light microscopy (LM) and electron microscopy (EM) sections from the same test ROI. Sections were cut parallel to each other with a maximum distance of 100 µm (see also Figure 8.1a). **(b)** Microscopy subsections used for r_{eff} and r_{arith} evaluation, consisting of three LM subsections and one EM subsection. **(c)** Reference data generation. We fully annotated EM subsections and used the resulting axon radius distribution as a reference for r_{arith}. For r_{eff}, we used part of the axon radius distribution from EM, including only axons with $r < 1.6\,\mu\text{m}$, and complemented the distribution with large axons from LM ($r \geq 1.6\,\mu\text{m}$). This approach follows the notion that the large-axon tail of the radius distribution can only be robustly captured in the large fields-of-view of LM. **(d)** CNN segmentation and derived axon radius distribution. For evaluation, r_{eff} and r_{arith}, computed from this axon radius distribution, were compared against their reference counterparts in (c). This procedure was applied to 18 LM subsections in total, three per test ROI of CC-01 (see Figure 8.1a and Table 8.1). Within each ROI, the same EM subsection served as the counterpart reference for all three LM subsections.

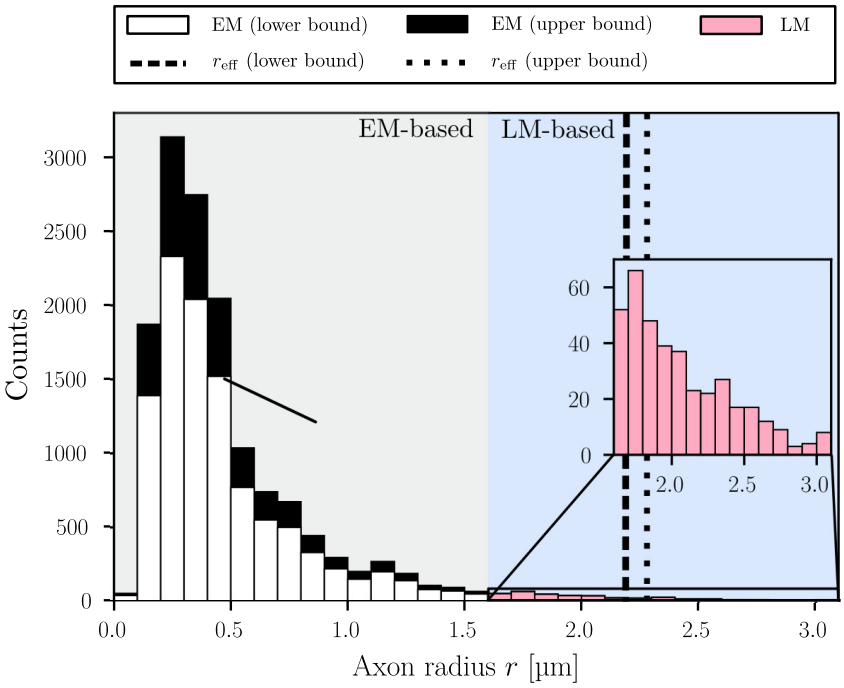

Figure 8.6: Generating reference axon radius distributions for r_{eff}. The histogram shows how we combined axon radius distributions from light microscopy (LM) and electron microscopy (EM) images to compute reference values for r_{eff}. Counts for $r < 1.6\,\mu\text{m}$ (gray background) were extracted from EM-based distributions, while counts for $r \geq 1.6\,\mu\text{m}$ (blue background) are taken from LM-based distributions. While LM-based counts were fixed, EM-based counts were scaled by a factor f to compensate for count differences due to the different subsection sizes between LM and EM. As f was unknown, we used lower and upper bound estimates based on specific assumptions (see main manuscript), leading to the two possible EM-based distributions shown. The resulting lower and upper estimates for r_{eff}, obtained after combining EM-based counts with fixed LM-based counts, are annotated as vertical lines.

8.8 Analyses for Chapter 4: Experimental validation of MRI-based axon radius mapping

8.8.1 Comparison of MRI-based axon radii across modalities

Qualitative comparison of spatial r_{eff} patterns

We examined how spatial patterns of r_{eff} in the mid-sagittal corpus callosum compare across modalities, including in vivo dMRI, ex vivo dMRI, histology and histology-based dMRI simulations. To this end, we projected r_{eff} values from each modality onto the mid-sagittal slice in MNI space [166]. The procedure was as follows:

- For histology and histology-based dMRI simulations, we aligned two-dimensional tissue masks to the mid-sagittal slice of the FSL HCP-1065 FA atlas in MNI space [222] (see Figure 8.7a,c,f). We then transformed ROI centroids into MNI space, assigned the corresponding histological or simulated r_{eff} values, and

generated continuous spatial maps using nearest-neighbor interpolation.

- For ex vivo dMRI, each ROI contained several voxels. We averaged r_{eff} values across voxels within the ROI in native space, then mapped these ROI-mean values to MNI space in the same way as for histology, taking advantage of the ROI-level registration between histology and ex vivo dMRI defined by our study design (see Figure 8.7e).
- For in vivo dMRI, we performed registration using both T_1-weighted images and FA maps to align data to MNI space (using the FSL HCP-1065 FA atlas and the FSL MNI152 T_1-weighted template [222]; see Figure 8.7g). After transforming per-subject r_{eff} maps to MNI space, we restricted analyses to voxels within the corpus callosum by applying a coarse mask from the JHU ICBM-DTI-81 white matter atlas [222, 223], together with thresholds on FA and r_{eff} (FA ≥ 0.65, $r_{\text{eff}} \geq 0.1\,\mu\text{m}$).

Quantitative comparison of spatial r_{eff} patterns

For the quantitative analysis, we compared r_{eff} values from dMRI experiments and simulations with corresponding histological measurements in their respective native spaces.

- For histology-based simulations, we directly compared simulated r_{eff} against the ground truth.
- For ex vivo dMRI, we calculated the mean r_{eff} across all voxels within each ROI, making use of the registration between ex vivo dMRI and histological ROIs established in our study design (see Figure 8.7e).
- For in vivo dMRI, histological ROI coordinates were first transformed to MNI space and then projected back to the closest voxel in native dMRI space (see Figure 8.7a,c–d). We applied the same voxel selection criteria for the corpus callosum as in the qualitative analysis (see previous paragraph). To generate values for comparison with histology, we used group-average r_{eff} maps obtained from spatially smoothed per-subject data (FWHM = 3.75 mm), with smoothing constrained to corpus callosum voxels [224]. The influence of spatial smoothing on the quantitative results was evaluated separately (see Figure B.6).

Error metrics

We evaluated quantitative agreement between histological values (r_{eff}) and estimates from dMRI experiments or simulations ($\hat{r}_{\text{eff}}$) using several complementary metrics. We fitted a linear regression and used its slope to characterize the scaling behavior of $\hat{r}_{\text{eff}}$ relative to r_{eff}.

Additionally, we calculated the fitting success rate (FSR), defined as the proportion of ROIs with biologically plausible estimates:

$$\text{FSR} = \frac{1}{N}\sum_{i=1}^{N} \mathbb{1}(\hat{r}_{\text{eff},i} > 0.1\,\mu\text{m}), \tag{8.5}$$

where $N = 35$ is the number of histological ROIs (see Figure 1.1f) and $\mathbb{1}(\cdot)$ is the

indicator function, equal to 1 if the condition holds and 0 otherwise.

To quantify absolute agreement, we computed the normalized root-mean-square error (NRMSE):

$$\mathrm{NRMSE} = \frac{\sqrt{\sum_{i=1}^{N}(\hat{r}_{\mathrm{eff},i} - r_{\mathrm{eff},i})^2}}{\sum_{i=1}^{N} r_{\mathrm{eff},i}}, \tag{8.6}$$

where we set $\hat{r}_{\mathrm{eff},i} = 0\,\mu\mathrm{m}$ for unsuccessful fits.

To quantify the ability to capture linear relationships, we computed Pearson's correlation coefficient:

$$R = \frac{\sum_{i=1}^{N}(\hat{r}_{\mathrm{eff},i} - \langle\hat{r}_{\mathrm{eff}}\rangle)(r_{\mathrm{eff},i} - \langle r_{\mathrm{eff}}\rangle)}{\sqrt{\sum_{i=1}^{N}(\hat{r}_{\mathrm{eff},i} - \langle\hat{r}_{\mathrm{eff}}\rangle)^2}\sqrt{\sum_{i=1}^{N}(r_{\mathrm{eff},i} - \langle r_{\mathrm{eff}}\rangle)^2}}, \tag{8.7}$$

with $\langle r_{\mathrm{eff}}\rangle$ and $\langle\hat{r}_{\mathrm{eff}}\rangle$ denoting the mean histological and estimated values across ROIs. We assessed statistical significance using a Monte Carlo permutation test under the null hypothesis that $\hat{r}_{\mathrm{eff}}$ and r_{eff} are uncorrelated ($R = 0$). We computed the p-value as

$$p = \frac{1}{K}\sum_{i=1}^{K} \mathbb{1}(|R_i'| \geq |R|), \tag{8.8}$$

where R_i' resulted from pairing shuffled histological values with fixed $\hat{r}_{\mathrm{eff}}$, using $K = 10^6$ permutations.

For dMRI simulations with $M = 1000$ repetitions, we pooled over all $M \times N$ values to compute the linear regression, FSR, R, and NRMSE. Accordingly, we computed p over $M \times K$ iterations with $K = 1000$ so that $M \times K = 10^6$.

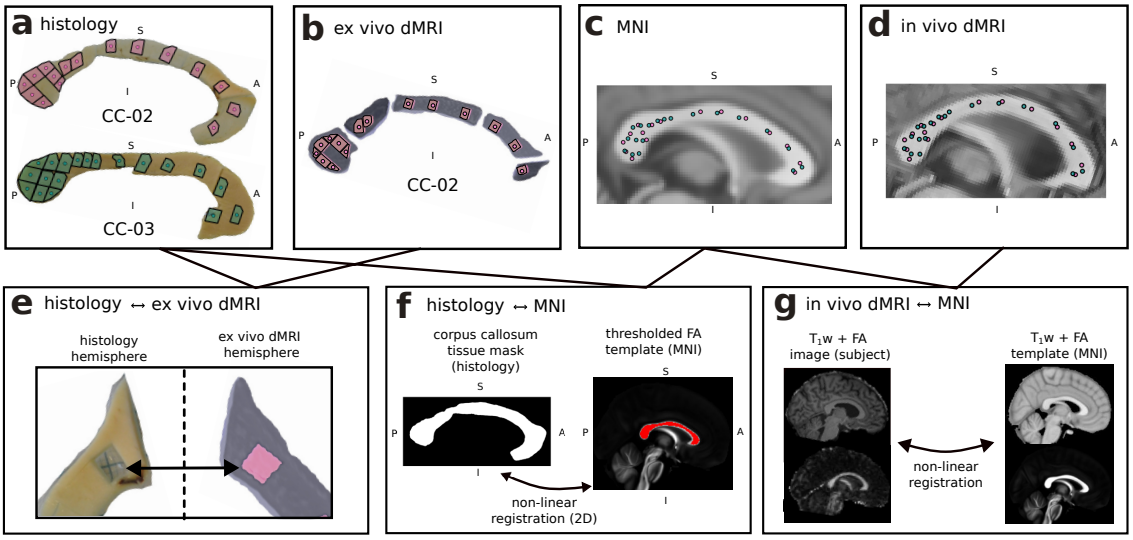

Figure 8.7: Regions of interest in different spaces and their registration **(a-d)** Regions of interest (ROIs) shown in different spaces: **(a)** histology, **(b)** ex vivo dMRI, **(c)** MNI space (overlaid on T1-weighted template), **(d)** in vivo dMRI (overlaid on T1-weighted image). Polygons and circles indicate ROI boundaries and centroids, with colors representing tissue sample CC-02 (magenta) or CC-03 (green). **(e)** Registration between histology and ex vivo dMRI. Matching ROIs were defined by the study design (see details in Figure 8.1b). Shown is one matching ROI in the two modalities. **(f)** Registration between histology and MNI space. We manually created 2D tissue masks (left image) for the images in (a) and registered these masks with the mid-sagittal slice of a fractional anisotropy (FA) atlas (the FSL HCP-1065 FA atlas [222], thresholded at FA ≥ 0.3) in MNI space (see red area in right image). **(g)** Registration between MNI space and in vivo dMRI. We simultaneously registered T_1-weighted image and FA map in native space to their corresponding templates in MNI space (the FSL HCP-1065 FA atlas and the FSL MNI152 T_1-weighted template [222]).

8.9 Analyses for Chapter 5: Understanding limitations of MRI-based axon radius mapping

8.9.1 Investigating the model-inherent bias

The analyses in Section 8.8 revealed a systematic discrepancy between dMRI-based r_{eff} and histological values, which we denoted as "model-inherent bias". To further study this bias, we conducted additional simulations based on the framework in Section 8.6 to examine its origins and its implications across different axon populations.

Origins of model-inherent bias

To identify the origins of model-inherent bias, we studied the approximations made during the derivation of r_{eff} from $S(b, \mathbf{g})$ (see Equation (2.51)) as potential candidates behind the model-inherent bias. These approximations include in successive order:

- the Gaussian phase approximation (GPA; see Equation (2.41)),
- the wide pulse approximation (WPA; see Equation (2.42)),
- the Taylor approximation (see Equation (2.45)),
- the exponential approximation (see Equation (2.46)).

To assess the accuracy of these approximations with respect to our reference method, we compared powder-averaged signals $S^\circ(b)$ generated using these approximations. In case of GPA and WPA, we used the corresponding expressions (see Equations (2.41) and (2.42)) for $S_{\text{cyl}}(b, \mathbf{g}, \mathbf{n}, r)$ to simulate $S_{\text{a}}(b, \mathbf{g})$ (see Equation (8.1)), then determined $S^\circ(b)$ via powder-averaging. For Taylor and exponential approximations, we directly simulated $S^\circ(b)$ using Equation (2.38) with the corresponding expression for $S_{\text{a}}^{\circ,\perp}(b)$ (see Equations (2.45) and (2.46)).

Implications of model-inherent bias

While the previous analysis aimed to identify the mechanisms behind the model-inherent bias to guide future modeling improvements, it is also essential to assess the applicability of r_{eff} within current methodological constraints. Therefore, we investigated how the model-inherent bias could affect r_{eff} measurements beyond the human corpus callosum, specifically in the human corticospinal tract and the rat corpus callosum. To this end, we repeated idealized (noiseless) simulations as in Section 8.6, applying scaling factors to extrapolate axon radii representative of the target anatomies (rat corpus callosum: 0.5 [15], human corticospinal tract: 1.15 [6]). For in vivo simulations, these scaling factors were combined with the tissue shrinkage compensation factor (1.3). For example, this resulted in an effective scaling of $1.15 \cdot 1.3 \approx 1.5$ for the corticospinal tract.

8.9.2 Impact of potential confounding factors

While the model-inherent bias originates from the mathematical formulation of the intra-axonal signal model, additional biases can arise from external sources, such as unaccounted-for signal contributions or noise.

Modeling assumptions as confounders

The signal model underlying r_{eff} estimation (see Equation (2.38)) requires additional parameters beyond r_{eff} itself: the immobile water fraction f_{im} and the intra-axonal diffusivity D_0. In the experimental validation in Chapter 4, these parameters are either estimated from experimental data (e.g., f_{im} ex vivo) or assumed to be fixed (e.g., $f_{\text{im}} = 0$ in vivo; literature-based D_0 for both scenarios). In additional simulations, we studied how inaccuracies in these parameters affect r_{eff} estimation by systematically varying estimates ($\hat{f}_{\text{im}}$ and $\hat{D}_0$), while using the "true" f_{im} and D_0 for signal simulations.

Noise as a confounder

We assessed how noise affects r_{eff}-estimation under both Gaussian and Rician noise models, which correspond to the expected noise distributions in complex-valued and magnitude dMRI data, respectively [31, 33, 34, 225]. To this end, we simulated

diffusion-weighted signals with Gaussian- or Rician-distributed signals, and used the corresponding ML powder-average estimator in the simulation pipeline (see Figure 8.3). The Rician ML estimator requires knowledge of the noise level σ. Similar to D_0 and f_{im}, the σ-dependency introduces an additional parameter estimation step and its associated errors. Hence, we adopted the approach of varying estimated values $\hat{\sigma}$ during processing while keeping the true σ for signal simulation.

8.10 Analyses for Chapter 6: Towards clinical translation of MRI-based axon radius mapping

8.10.1 Optimal in vivo MRI protocols

Using our dMRI simulation framework (see Section 8.6), we optimized in vivo protocols across maximum gradient amplitudes $g_{\max} \in [40, 600]$ mT/m, covering contemporary clinical and research 3 T scanners. The objective was to maximize the correlation R between histological r_{eff} and simulated r_{eff} for a single hypothetical subject across candidate protocols.

Definition of the optimization problem

To streamline the parameter search, we imposed the constraints of our experimental in vivo protocol: two-b-shell designs with timing parameters (δ, Δ) and the minimum gradient amplitude $g_{\min}$ as optimization variables, with (δ, Δ) shared across shells. We fixed the minimum b-value to $b_{\min} = 6\,\mathrm{ms/\mu m^2}$ and assumed this effectively suppresses the extra-axonal signal; accordingly, we set $S_{\mathrm{e}}(b, \mathbf{g}) = 0$ in the simulations. Formally, the optimization problem can be written as:

$$\theta^*\big|_{g_{\max}} = \arg\max_{\theta} R(\theta)\big|_{g_{\max}}, \qquad \theta = \{\delta, \Delta, g_{\min}\}. \tag{8.9}$$

The search grid for θ and additional simulation parameters and assumptions are listed in Table 8.4. Furthermore, we enforced the timing constraint $\Delta \geq \delta + 4\,\mathrm{ms}$ to accommodate RF and readout gradients.

Noise assumptions

We assumed Gaussian noise for the optimization, in contrast to the Rician noise present in magnitude dMRI data [31], including our experimental data. While Rician noise tends to obscure correlations, preprocessing techniques can mitigate its effects and approximately restore Gaussian-distributed signal behavior [104–106]. We therefore used Gaussian noise to focus on protocol performance independent of correction methods for non-Gaussian noise distribution [32–34].

Modeling echo time, intra-axonal fraction, and SNR

We modeled how the timing parameters (δ, Δ) affect the echo time (TE), the T_2-weighted intra-axonal water fraction (f_{a}), and signal-to-noise ratio (SNR). We

estimated the echo time for a candidate protocol as

$$\mathrm{TE}(\theta) = \delta + \Delta + C, \tag{8.10}$$

with $C = 21\,\mathrm{ms}$ to account for RF and readout gradients; this value was derived from our experimental protocol. Assuming $f_{\mathrm{im}} = 0$ [172], we computed

$$f_{\mathrm{a}}(\mathrm{TE}) = \frac{f_0\, e^{-\mathrm{TE}/T_{2,\mathrm{a}}}}{f_0\, e^{-\mathrm{TE}/T_{2,\mathrm{a}}} + (1 - f_0)\, e^{-\mathrm{TE}/T_{2,\mathrm{e}}}}, \tag{8.11}$$

with $f_0 = 0.41$, $T_{2,\mathrm{a}} = 82\,\mathrm{ms}$, and $T_{2,\mathrm{e}} = 44\,\mathrm{ms}$ [128]. We scaled SNR relative to our experimental reference protocol ($\mathrm{SNR}_{\mathrm{ref}} = 32$, $\mathrm{TE}_{\mathrm{ref}} = 66\,\mathrm{ms}$) as

$$\mathrm{SNR}(\mathrm{TE}) = \mathrm{SNR}_{\mathrm{ref}} \cdot \frac{f_0\, e^{-\mathrm{TE}/T_{2,\mathrm{a}}} + (1 - f_0)\, e^{-\mathrm{TE}/T_{2,\mathrm{e}}}}{f_0\, e^{-\mathrm{TE}_{\mathrm{ref}}/T_{2,\mathrm{a}}} + (1 - f_0)\, e^{-\mathrm{TE}_{\mathrm{ref}}/T_{2,\mathrm{e}}}}. \tag{8.12}$$

Note that, despite assuming $S_{\mathrm{e}} = 0$, the extra-axonal compartment still enters Equations (8.11) and (8.12) via $T_{2,\mathrm{e}}$ and (1-f_0). These equations are evaluated for the two-compartment baseline at $b \approx 0$, consistent with how $\mathrm{SNR}_{\mathrm{ref}}$ was measured.

To assess potential gains from improved hardware or acquisition, we repeated the optimization with $\mathrm{SNR}_{\mathrm{ref}}$ increased by 75 % and 150 %, yielding SNRs of 56 and 80 for our experimental reference protocol.

8.10.2 Clinical application simulations

Motivated by prior reports of a 28.6 % reduction in axon radii in the splenium of individuals with autism spectrum disorder (ASD) [7], we studied a hypothetical application in which r_{eff} distinguishes ASD subjects from healthy controls. To this end, we conducted a statistical power analysis using optimized protocols for next-generation clinical scanners (see Section 8.10.1). We focused on the mid-sagittal slice of the splenium, which contained $L = 11$ voxels on average in our in vivo dMRI data. We estimated statistical power via a Monte Carlo simulation with $M = 5000$ iterations, evaluating various group sizes (N). In each iteration:

1. We sampled $L \times N$ splenium ROIs per group (healthy and ASD) with replacement from our histological dataset (see splenium ROIs in Figure 1.1f).

2. To synthesize axon radius distributions for the ASD group, we reduced all radii by 28.6 %, while leaving those of healthy controls unchanged.

3. We simulated Gaussian-distributed dMRI signals and estimated r_{eff} for all sampled ROIs.

4. We averaged r_{eff} across the L splenium voxels to obtain subject-level values.

5. We performed a two-sample t-test ($\alpha = 0.05$) to assess group differences, with the null hypothesis of equal group means.

Table 8.4: Protocol optimization parameters. Annotations denote:
[1] estimated as the mean of previously reported values [17, 167];
[2] estimated from our experimental data;
[3] parameters of our experimental protocol;
[4] we assumed $D_0 = D_{\mathrm{a}}^{\parallel}$;
[5] reported by Veraart et al. [128];
[6] reported by Tax et al. [172];
[7] computed via the PGSE b-value relation (see Equation (2.28));
[8] computed as $f_{\mathrm{e}} = 1 - f_{\mathrm{a}} - f_{\mathrm{im}}$.

Parameter	Symbol	Unit	Value
Signal-to-noise ratio	SNR	-	Equation (8.12)
Radius scaling factor	-	-	1.3^{1}
Neurite dispersion	-	-	8.2^{2}
Diffusion shells	-	-	2^{3}
Gradient directions per shell	-	-	$(60, 120)^{3}$
Axoplasmic diffusivity	D_0	µm^2/ms	2.07^{4}
Parallel intra-axonal diffusivity	$D_{\mathrm{a}}^{\parallel}$	µm^2/ms	2.07^{5}
Minimum b	b_{min}	ms/µm^2	6^{3}
Maximum b	b_{max}	ms/µm^2	$f(\delta, \Delta, g_{\mathrm{max}})$ [7]
Minimum g	g_{min}	mT/m	$f(\delta, \Delta, b_{\mathrm{min}})$ [7]
Maximum g	g_{max}	mT/m	$[40, 600]$
Diffusion gradient time	δ	ms	$[2, 60]$
Diffusion gradient separation	Δ	ms	$[6, 80]$
Intra-axonal water fraction	f_0	-	0.41^{5}
Immobile water fraction	f_{im}	-	0^{6}
T_2-weighted intra-axonal water fraction	f_{a}	-	Equation (8.11)
T_2-weighted extra-axonal water fraction	f_{e}	-	$f(f_{\mathrm{a}}, f_{\mathrm{im}})$ [8]
Extra-axonal signal	S_{e}	-	0
Intra-axonal transverse relaxation time	$T_{2,\mathrm{a}}$	ms	82^{5}
Extra-axonal transverse relaxation time	$T_{2,\mathrm{e}}$	ms	44^{5}
Echo time	TE	ms	Equation (8.10)

Finally, we estimated statistical power as the proportion of iterations in which the t-test rejected the null hypothesis (of equal group means).

Appendix A

The matrix method for diffusion MRI simulations

The matrix method [216] provides an efficient way to compute diffusion-weighted signals in restricted geometries, such as axonal cylinders, without resorting to computationally expensive Monte Carlo simulations. The key idea is to discretize the gradient waveform into short intervals of length τ, with the instantaneous gradient amplitude $g(n\tau)$ encoded as integer steps of size g_{step} (see Figure A.1). At time $n\tau$, the amplitude of the (scalar) wave-vector is $m_n q$, where $m_n \in \mathbb{Z}$ and $q = (2\pi)^{-1}\tau g_{\text{step}}$. Following the convention in the literature, the normalized signal is denoted by E and can be written as

$$E = S(q)\, R\, [A(q)]^{m_2} R \ldots R\, [A(q)]^{m_{N-1}} R\, S^T(-q), \tag{A.1}$$

where the matrices S, R, and A represent, respectively, the initial phase modulation, diffusive attenuation during τ, and coupling of diffusion modes under a gradient. Their specific form depends on the restricted geometry (e.g., cylindrical or spherical), but once computed, they provide a compact and efficient representation of the signal evolution. For further details, see Callaghan [216].

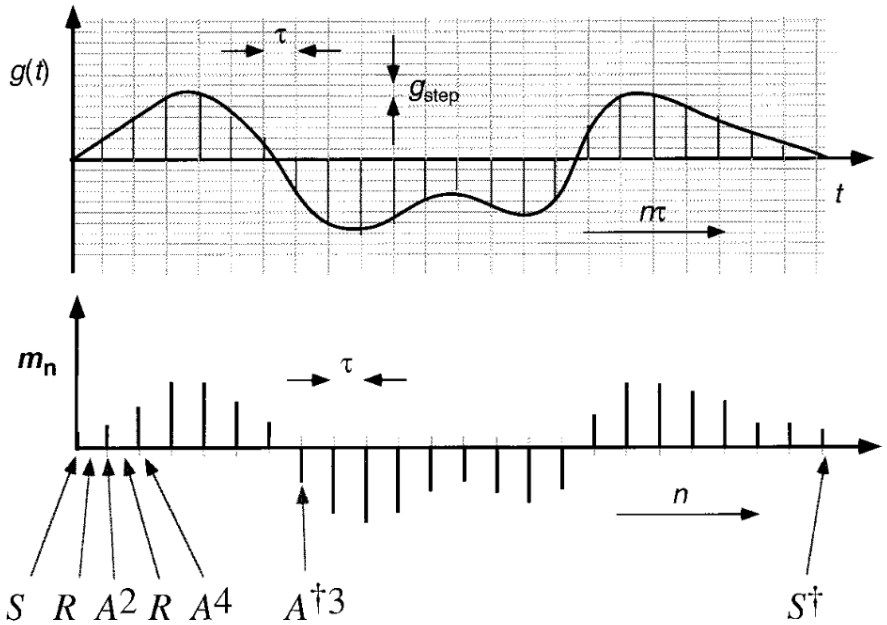

Figure A.1: The matrix method. Schematic decomposition of a generalized gradient waveform $g(t)$ into a sequence of time intervals of length τ (top). Each interval is represented by an integer multiple m_n of the basic gradient step g_{step}. The diffusion signal can then be written as a sequence of matrix operators (bottom), alternating between phase-modulation operators S and A^{m_n}, and diffusive attenuation R. Negative gradient steps are represented by the Hermitian transpose $A^{\dagger}$.[a]

[a]Reproduced from Callaghan [216], with permission from Elsevier.

Appendix B

Supplementary figures

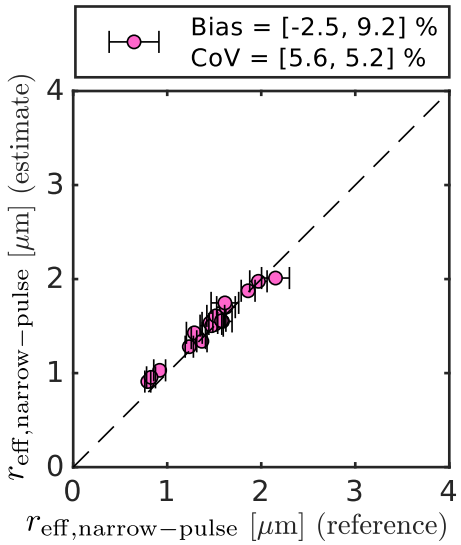

Figure B.1: Validation of $r_{\mathbf{eff}}$ in the narrow-pulse definition. **(a)** Comparison of light microscopy (LM)-based estimates of the narrow-pulse approximation of the effective radius, $r_{\mathrm{eff,narrow\text{-}pulse}} = \sqrt{\langle r^4 \rangle / \langle r^2 \rangle}$, against reference values from manual annotations. Each marker represents one LM subsection, while the dashed line indicates theoretical perfect agreement. Reference values are shown as a bounded range, reflecting uncertainty in combining EM-based estimates for small axons ($r < 1.6\,\mu\mathrm{m}$) and LM-based estimates for large axons ($r \geq 1.6\,\mu\mathrm{m}$) (see Figure 8.5 in *Materials and methods* for an illustration). The legend reports bias (see Equation (8.3)), and coefficient of variation (CoV, see Equation (8.4)), each calculated for the lower and upper bounds of the reference.

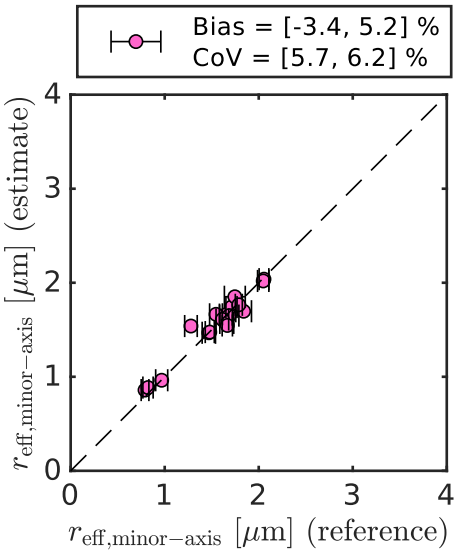

Figure B.2: Validation of $r_{\mathbf{eff}}$ using the minor-axis definition. Comparison of light microscopy (LM)-based r_{eff} estimates against reference values from manual annotations, using the minor axis of an ellipse fitted to each axon as the radius estimate (see Figure 2.7c for an illustration). Each marker represents one LM subsection, while the dashed line indicates theoretical perfect agreement. Reference values are shown as a bounded range, reflecting uncertainty in combining EM-based estimates for small axons ($r < 1.6\,\mu\mathrm{m}$) and LM-based estimates for large axons ($r \geq 1.6\,\mu\mathrm{m}$) (see Figure 8.5 in *Materials and methods* for an illustration). The legend reports bias (see Equation (8.3)), and coefficient of variation (CoV, see Equation (8.4)), each calculated for the lower and upper bounds of the reference.

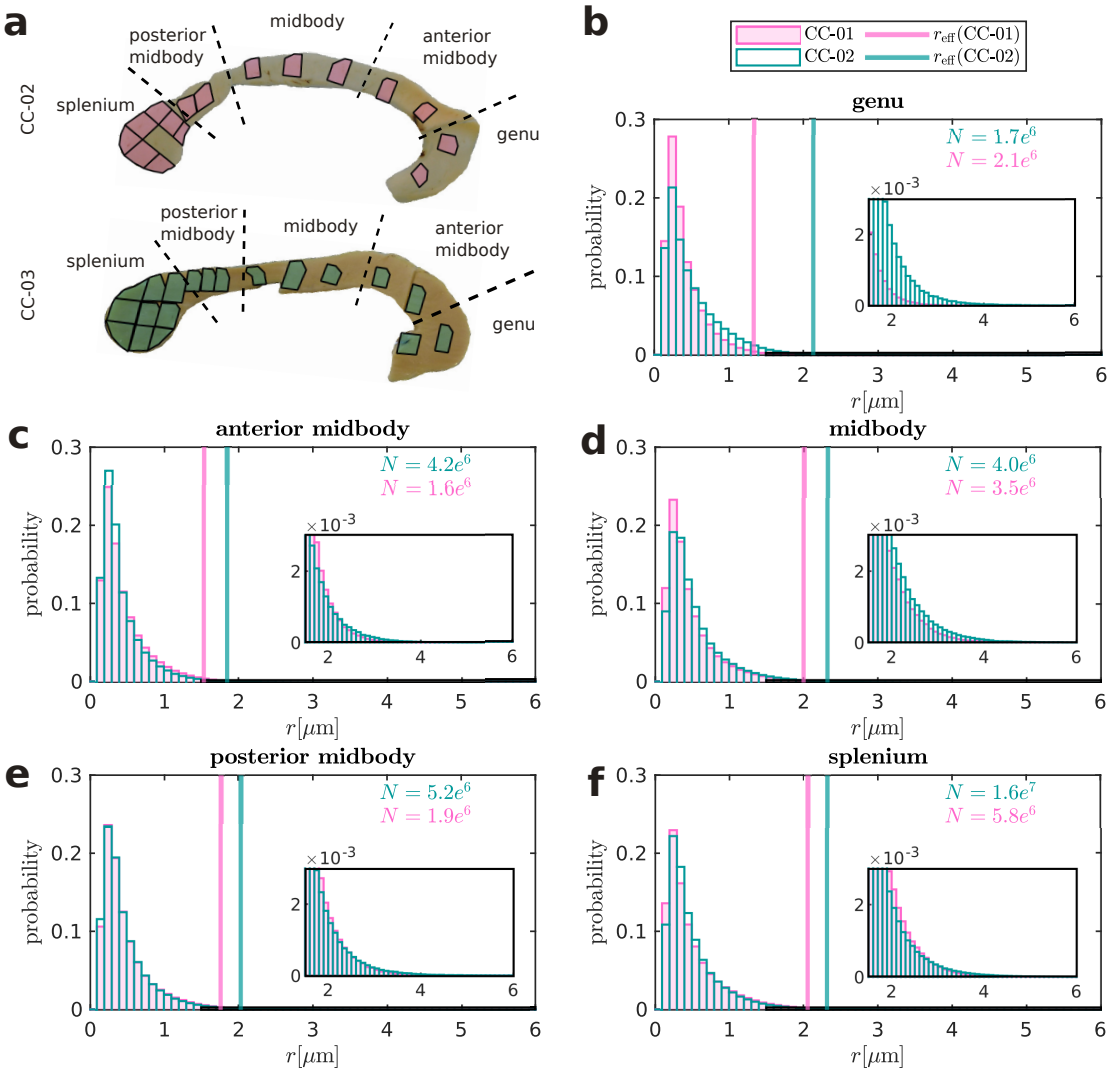

Figure B.3: Axon radius distributions from light microscopy. **(a)** Corpus callosum sketch with light microscopy (LM) ROIs (polygons) and segmentation into five regions (dashed lines). **(b-f)** Axon radius distributions pooled over the light microscopy ROIs for each corpus callosum region shown in (a). Colors indicate tissue sample (see legend in (b)). Vertical lines denote r_{eff} as per Equation (2.47). Annotated numbers inside the plot denote axon count. Insets highlight the tail of axon radius distributions.

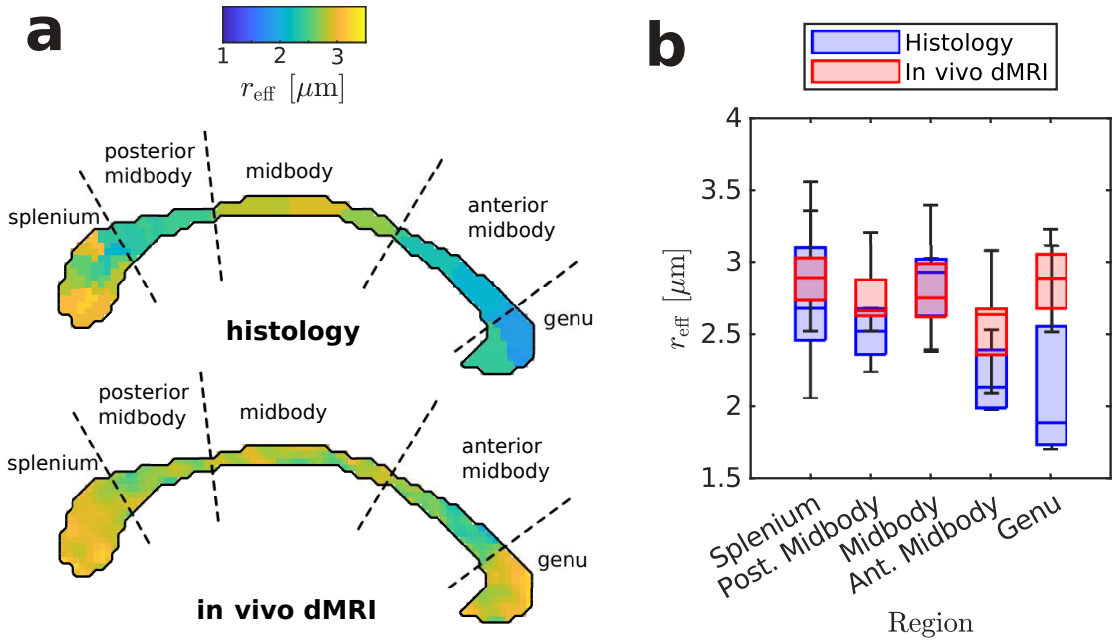

Figure B.4: Validation of in vivo MRI-based spatial r_{eff} pattern. **(a)** Group-level spatial patterns of r_{eff} across the corpus callosum for histology and in vivo dMRI, shown in a mid-sagittal MNI slice with corpus callosum subregions indicated (dashed lines). Histological spatial patterns were interpolated using the nearest-neighbor method, evaluated at histological ROI locations in Figure 1.1f. **(b)** Distribution of r_{eff} values across corpus callosum subregions annotated in (a), pooled over ROI voxels within each subregion. Histological values in (a–b) were scaled by 1.3 to compensate for tissue shrinkage compared to in vivo conditions [17, 167].

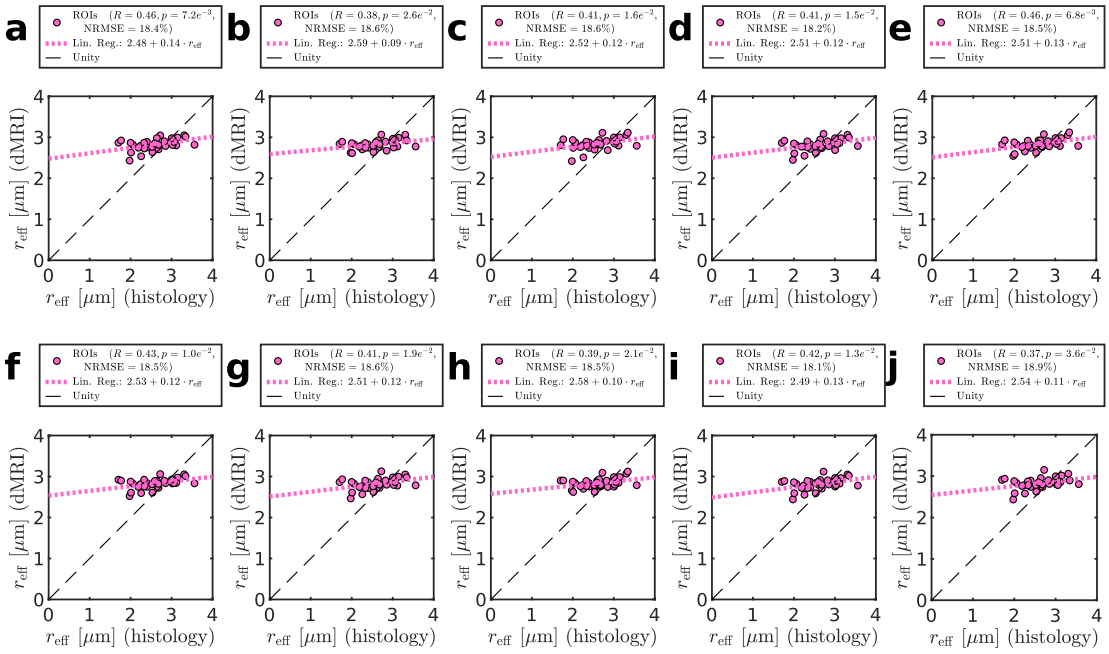

Figure B.5: Reproducibility of in vivo MRI-based r_{eff}. **(a-j)** ROI-wise comparisons of group-level in vivo dMRI-based r_{eff} against histological values. Each plot represents one of ten repeated runs through our in vivo processing pipeline. Markers correspond to histological ROIs in Figure 1.1f. Dashed lines illustrate theoretical perfect agreement, whereas dotted lines represent linear regressions. Legends provide metrics computed over all ROIs, including Pearson's correlation coefficient (R) with corresponding p-value, and the normalized root-mean-square error (NRMSE) (see Section 8.8.1 for metric definitions). Run-to-run differences arose from non-determinism in the GPU-accelerated eddy current and motion correction [115, 206, 207] during in vivo dMRI preprocessing.

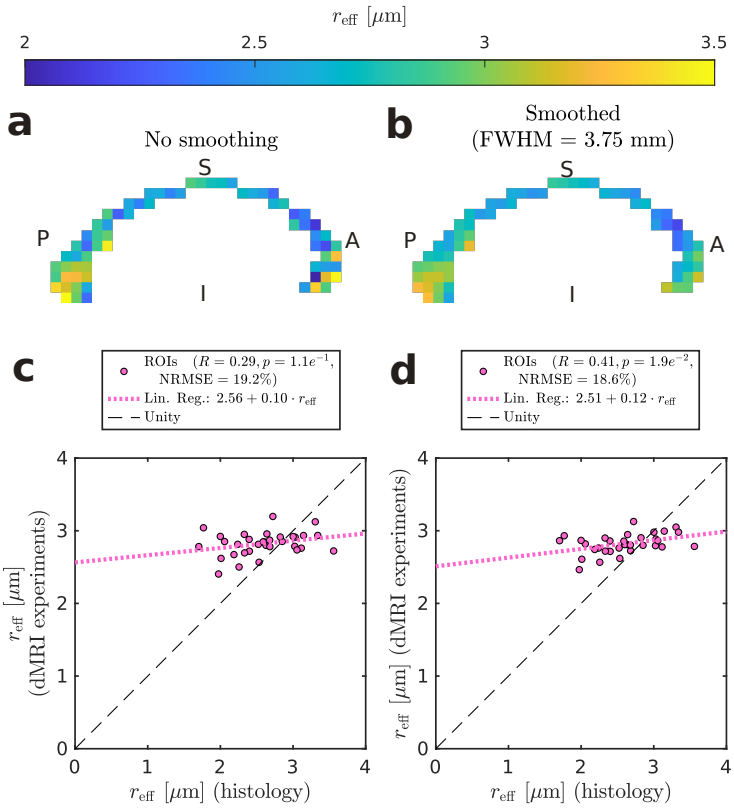

Figure B.6: Impact of smoothing on in vivo MRI-based r_{eff}. **(a-b)** Spatial patterns of r_{eff} across the corpus callosum: **(a)** before smoothing and **(b)** after smoothing with FWHM = 3.75 mm (1.5× voxel size). Patterns show the mid-sagittal section of the corpus callosum for an exemplary subject in native space. **(c-d)** ROI-wise comparison of group-level in vivo dMRI-based r_{eff} against histological values. The group-level r_{eff} were computed from: **(c)** unsmoothed maps, as illustrated in (a), and **(d)** smoothed maps, as illustrated in (b). Markers correspond to histological ROIs in Figure 1.1f. Dashed lines illustrate theoretical perfect agreement, whereas dotted lines represent linear regressions. Legends provide metrics computed over all ROIs, including Pearson's correlation coefficient (R) and the corresponding p-value, the normalized root-mean-square error (NRMSE) (see Section 8.8.1 for metric definitions).

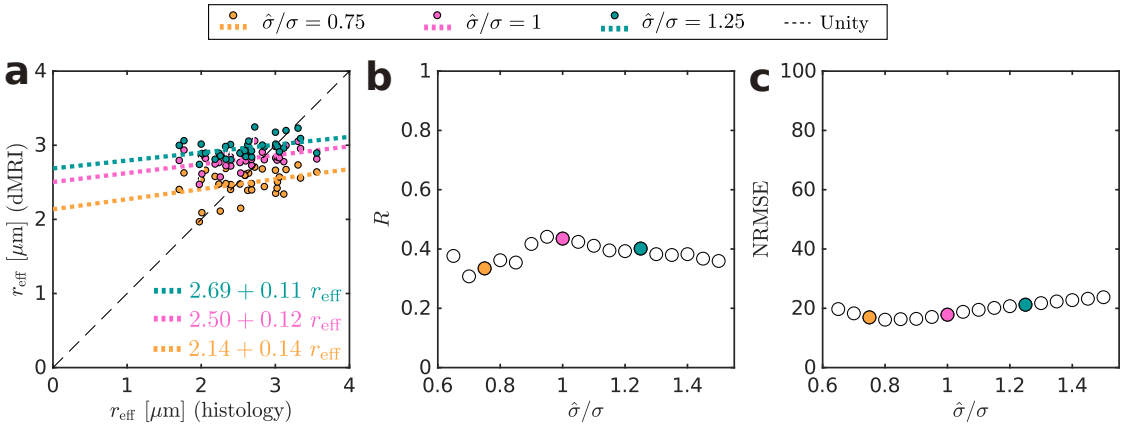

Figure B.7: Impact of noise level estimation in experimental in vivo MRI. **(a)** ROI-wise comparisons of in vivo dMRI-based r_{eff} and histological values. Color coding indicates different noise level (σ) estimates, denoted as $\hat{\sigma}$. Here, we assumed σ estimated from experimental data (see Section 8.4) as the ground truth, and varied $\hat{\sigma}$ relative to σ. From there, we repeated processing as in experimental data, including powder-averaging and r_{eff} estimation. Markers correspond to histological ROIs in Figure 1.1f. Dashed lines illustrate theoretical perfect agreement, whereas dotted lines represent linear regressions. **(b-c)** Error metrics as a function of relative misestimation ($\hat{\sigma}/\sigma$): **(b)** Pearson's correlation coefficient (R) and **(c)** normalized root-mean-square error (NRMSE) (see Section 8.8.1 for metric definitions). Colored markers correspond to the $\hat{\sigma}$ values used in (a).

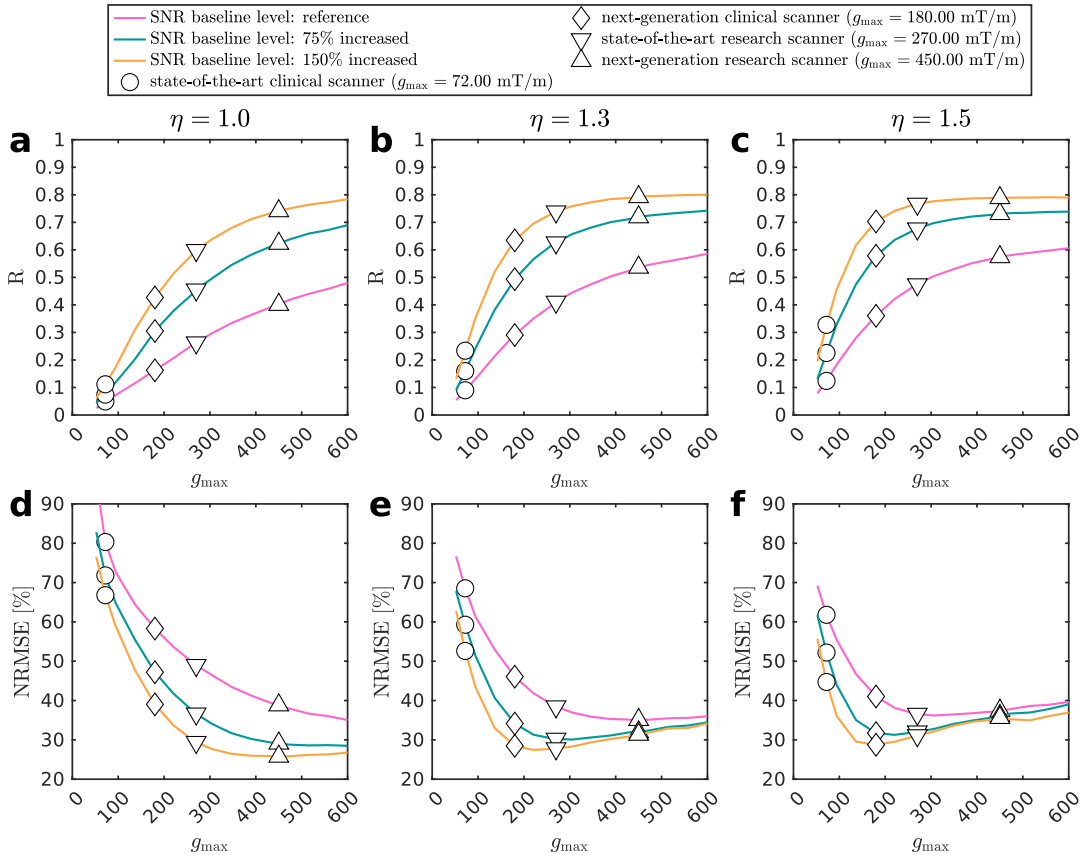

Figure B.8: In vivo protocol optimization metrics for varying tissue shrinkage. **(a-c)** Optimal Pearson's correlation coefficients (R) as a function of maximum gradient amplitude (g_{max}). Columns show R for different radius scaling factors used to compensate for tissue shrinkage: **(a)** $\eta = 1$, **(b)** $\eta = 1.3$, and **(c)** $\eta = 1.5$. While $\eta = 1.3$ [17, 167] was used as an estimate for in vivo conditions throughout the main body of the thesis, $\eta = 1.0$ and $\eta = 1.5$ represent the scenarios of no tissue shrinkage and very strong tissue shrinkage. Markers encode g_{max} of existing clinical scanners and research scanners (assuming 90 % of the nominal g_{max}). Line colors indicate different SNR baseline levels. While the reference SNR baseline level reflects our experimental conditions, increased SNR baseline levels assume an SNR increase through potential technical or acquisition advances. In addition, the SNR of a particular protocol candidate depends on the protocol parameters (see Equation (8.12)). For our experimental protocol, baseline SNR levels would correspond to SNR values of 32 (reference), 56 (75 % increased), and 80 (150 % increased). **(d-f)** Optimal normalized root-mean-square error (NRMSE) as a function of maximum gradient amplitude (g_{max}) for different η, with definitions as in (a-c). Note that we optimized protocols by maximizing R, whereas NRMSE is an auxiliary metric.

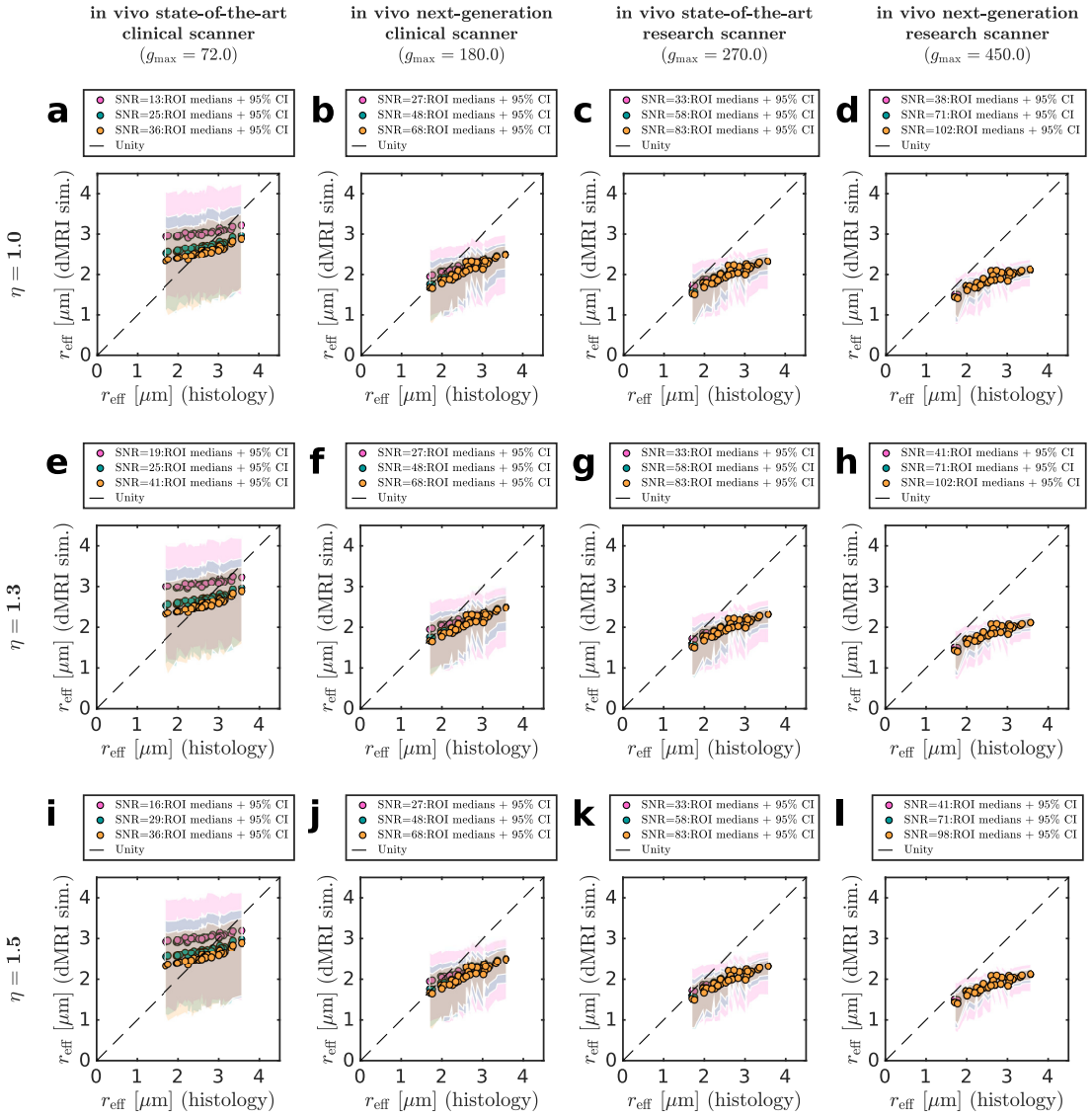

Figure B.9: Optimal in vivo MRI protocols for various scanners. The plots show r_{eff} derived from dMRI simulations with optimal protocols against the histological r_{eff} for various maximum gradient amplitudes g_{max} of existing/upcoming scanners (columns), assuming 90 % of nominal values. The η values (rows) denote radius scaling factors compensating for tissue shrinkage in histology data. While $\eta = 1.3$ [17, 167] was used as an estimate for in vivo conditions throughout the main body of the thesis, $\eta = 1.0$ and $\eta = 1.5$ represent the scenarios of no tissue shrinkage and very strong tissue shrinkage. Markers correspond to histological ROIs in Figure 1.1f. The 95 % confidence interval for ROIs (shaded areas) was computed across 1000 noise realizations. Colors indicate different SNR baseline levels. While the reference SNR baseline level reflects our experimental conditions, increased SNR baseline levels assume an SNR increase through potential technical or acquisition advances. In addition, the SNR of a particular protocol candidate depends on the protocol parameters (see Equation (8.12)). See Table C.1 for the full set of protocol parameters and metrics for protocols shown here.

Appendix C

Supplementary tables

Table C.1: Optimal in vivo MRI protocol parameters. All dMRI protocols use two shells with $(60, 120)$ diffusion gradient directions. The SNR baseline level describes the SNR conditions compared to our dMRI experiments. While the reference SNR baseline level corresponds to our experimental conditions, increased SNR baseline levels assume an SNR increase through potential technical or acquisition advances. η is a radius scaling factor compensating for tissue shrinkage in histology data, where $\eta = 1.3$ reflects the value assumed throughout the main body of the thesis. g_{min} and g_{max} are the diffusion gradient amplitudes of the two diffusion shells; $b_{\text{min}} = 6\,\text{ms}/\mu\text{m}^2$ and b_{max} denote the corresponding diffusion-weightings. δ and Δ are the gradient diffusion time and separation, consistent across shells. Echo time (TE) was estimated according to Equation (8.10). The SNR was estimated using Equation (8.12), reflecting not only the baseline SNR level, but also protocol parameter-dependent SNR variation. Metrics include Pearson's correlation coefficient (R) and its associated p-value, as well as the normalized root-mean-square-error (NRMSE), and the fitting success rate (FSR) (see Section 8.8.1 for metric definitions). The optimal dMRI protocol with maximum R per combination of η and SNR baseline level is highlighted in bold.

SNR baseline	η	g_{max} [mT/m]	g_{min} [mT/m]	b_{max} [ms/µm^2]	δ [ms]	Δ [ms]	TE [ms]	SNR	R	p	NRMSE [%]	FSR [%]
reference	1.0	72	30.9	32.5	48	54	124	12.8	0.05	$8.4e^{-1}$	80.3	54.2
		180	81.3	29.4	24	30	76	27.3	0.16	$4.5e^{-1}$	58.3	68.7
		270	119.9	30.4	18	24	64	33.2	0.26	$1.8e^{-1}$	49.0	78.4
		450	**167.0**	**43.6**	**14**	**20**	**56**	**38.0**	**0.40**	$2.5e^{-2}$	**38.8**	**89.6**
	1.3	72	46.4	14.4	36	42	100	18.6	0.09	$7.0e^{-1}$	68.5	59.2
		180	81.3	29.4	24	30	76	27.3	0.29	$1.3e^{-1}$	46.1	82.5
		270	119.9	30.4	18	24	64	33.2	0.41	$2.0e^{-2}$	38.5	91.4
		450	**203.9**	**29.2**	**12**	**18**	**52**	**40.7**	**0.54**	$< 1e^{-3}$	**35.1**	**97.5**
	1.5	72	40.1	19.4	40	46	108	16.4	0.12	$5.8e^{-1}$	61.8	65.3
		180	81.3	29.4	24	30	76	27.3	0.36	$4.6e^{-2}$	41.0	89.4
		270	119.9	30.4	18	24	64	33.2	0.47	$4.8e^{-3}$	36.6	96.0
		450	**203.9**	**29.2**	**12**	**18**	**52**	**40.7**	**0.57**	$< 1e^{-3}$	**37.4**	**99.2**
75% increased	1.0	72	35.0	25.4	44	50	116	25.3	0.07	$7.6e^{-1}$	71.8	57.9
		180	81.3	29.4	24	30	76	47.7	0.31	$1.2e^{-1}$	47.2	79.3
		270	119.9	30.4	18	24	64	58.1	0.46	$9.9e^{-3}$	36.6	89.1
		450	**203.9**	**29.2**	**12**	**18**	**52**	**71.1**	**0.62**	$< 1e^{-3}$	**29.1**	**96.6**
	1.3	72	35.0	25.4	44	50	116	25.3	0.16	$4.6e^{-1}$	59.3	67.7
		180	81.3	29.4	24	30	76	47.7	0.49	$3.7e^{-3}$	34.1	92.7
		270	119.9	30.4	18	24	64	58.1	0.63	$< 1e^{-3}$	30.2	97.6
		450	**203.9**	**29.2**	**12**	**18**	**52**	**71.1**	**0.72**	$< 1e^{-3}$	**32.0**	**99.7**
	1.5	72	40.1	19.4	40	46	108	28.7	0.23	$2.7e^{-1}$	52.2	75.1
		180	81.3	29.4	24	30	76	47.7	0.58	$< 1e^{-3}$	31.7	96.9
		270	119.9	30.4	18	24	64	58.1	0.68	$< 1e^{-3}$	32.1	99.3
		450	**203.9**	**29.2**	**12**	**18**	**52**	**71.1**	**0.73**	$< 1e^{-3}$	**36.1**	**100.0**
150% increased	1.0	72	35.0	25.4	44	50	116	36.2	0.11	$6.3e^{-1}$	66.8	61.4
		180	81.3	29.4	24	30	76	68.1	0.43	$1.9e^{-2}$	39.0	86.1
		270	119.9	30.4	18	24	64	83.0	0.60	$< 1e^{-3}$	29.4	94.2
		450	**203.9**	**29.2**	**12**	**18**	**52**	**101.6**	**0.74**	$< 1e^{-3}$	**25.8**	**98.6**
	1.3	72	40.1	19.4	40	46	108	40.9	0.23	$2.5e^{-1}$	52.6	74.1
		180	81.3	29.4	24	30	76	68.1	0.63	$< 1e^{-3}$	28.5	96.6
		270	119.9	30.4	18	24	64	83.0	0.74	$< 1e^{-3}$	27.8	99.2
		450	**203.9**	**29.2**	**12**	**18**	**52**	**101.6**	**0.79**	$< 1e^{-3}$	**31.3**	**100.0**
	1.5	72	35.0	25.4	44	50	116	36.2	0.33	$8.5e^{-2}$	44.7	82.3
		180	81.3	29.4	24	30	76	68.1	0.70	$< 1e^{-3}$	28.8	98.8
		270	119.9	30.4	18	24	64	83.0	0.77	$< 1e^{-3}$	31.1	99.8
		450	**190.8**	**33.4**	**12**	**20**	**54**	**98.2**	**0.79**	$< 1e^{-3}$	**35.6**	**100.0**

References

[1] M. Drakesmith, R. Harms, S. U. Rudrapatna, G. D. Parker, C. J. Evans, and D. K. Jones. "Estimating axon conduction velocity in vivo from microstructural MRI". *NeuroImage* 203 (Dec. 2019), p. 116186. DOI: 10.1016/j.neuroimage.2019.116186.

[2] H. Schmidt and T. R. Knösche. "Action potential propagation and synchronisation in myelinated axons". *PLOS Computational Biology* 15.10 (Oct. 2019). Publisher: Public Library of Science, e1007004. DOI: 10.1371/journal.pcbi.1007004.

[3] S. G. Waxman. "Determinants of conduction velocity in myelinated nerve fibers". *Muscle & Nerve* 3.2 (1980), pp. 141–150. DOI: https://doi.org/10.1002/mus.880030207.

[4] R. Caminiti, H. Ghaziri, R. Galuske, P. R. Hof, and G. M. Innocenti. "Evolution amplified processing with temporally dispersed slow neuronal connectivity in primates". *Proceedings of the National Academy of Sciences of the United States of America* 106.46 (Nov. 2009), pp. 19551–19556. DOI: 10.1073/pnas.0907655106.

[5] S. Tomasi, R. Caminiti, and G. M. Innocenti. "Areal Differences in Diameter and Length of Corticofugal Projections". *Cerebral Cortex* 22.6 (June 2012), pp. 1463–1472. DOI: 10.1093/cercor/bhs011.

[6] J. Veraart, E. P. Raven, L. J. Edwards, N. Weiskopf, and D. K. Jones. "The variability of MR axon radii estimates in the human white matter". *Human Brain Mapping* 42.7 (2021), pp. 2201–2213. DOI: 10.1002/hbm.25359.

[7] J. Wegiel, W. Kaczmarski, M. Flory, V. Martinez-Cerdeno, T. Wisniewski, K. Nowicki, I. Kuchna, and J. Wegiel. "Deficit of corpus callosum axons, reduced axon diameter and decreased area are markers of abnormal development of interhemispheric connections in autistic subjects". *Acta Neuropathologica Communications* 6.1 (Dec. 2018), p. 143. DOI: 10.1186/s40478-018-0645-7.

[8] B. Zikopoulos and H. Barbas. "Changes in prefrontal axons may disrupt the network in autism". *The Journal of Neuroscience: The Official Journal of the Society for Neuroscience* 30.44 (Nov. 2010), pp. 14595–14609. DOI: 10.1523/JNEUROSCI.2257-10.2010.

[9] N. Evangelou, D. Konz, M. M. Esiri, S. Smith, J. Palace, and P. M. Matthews. "Size-selective neuronal changes in the anterior optic pathways suggest a differential susceptibility to injury in multiple sclerosis". *Brain: A Journal of Neurology* 124.Pt 9 (Sept. 2001), pp. 1813–1820. DOI: 10.1093/brain/124.9.1813.

[10] H. Fu, J. Li, C. Zhang, G. Gao, Q. Ge, X. Guan, and D. Cui. "Pathological axonal enlargement in connection with amyloidosis, lysosome destabilization, and bleeding is a major defect in Alzheimer's disease". *Neural Regeneration Research* 21.2 (Apr. 2024), pp. 790–799. DOI: 10.4103/NRR.NRR-D-24-01440.

[11] M. Schechter, J. Grigoletto, S. Abd-Elhadi, H. Glickstein, A. Friedman, G. E. Serrano, T. G. Beach, and R. Sharon. "A role for -Synuclein in axon growth and its implications in corticostriatal glutamatergic plasticity in Parkinson's disease". *Molecular Neurodegeneration* 15.1 (Mar. 2020), p. 24. DOI: 10.1186/s13024-020-00370-y.

[12] Y. Assaf, T. Blumenfeld-Katzir, Y. Yovel, and P. J. Basser. "AxCaliber: A Method for Measuring Axon Diameter Distribution from Diffusion MRI". *Magnetic resonance in medicine* 59.6 (June 2008), pp. 1347–1354. DOI: 10.1002/mrm.21577.

[13] D. C. Alexander, P. L. Hubbard, M. G. Hall, E. A. Moore, M. Ptito, G. J. M. Parker, and T. B. Dyrby. "Orientationally invariant indices of axon diameter and density from diffusion MRI". *NeuroImage* 52.4 (Oct. 2010), pp. 1374–1389. DOI: 10.1016/j.neuroimage.2010.05.043.

[14] F. Sepehrband, D. C. Alexander, N. D. Kurniawan, D. C. Reutens, and Z. Yang. "Towards higher sensitivity and stability of axon diameter estimation with diffusion-weighted MRI". *NMR in biomedicine* 29.3 (Mar. 2016), pp. 293–308. DOI: 10.1002/nbm.3462.

[15] J. Veraart, D. Nunes, U. Rudrapatna, E. Fieremans, D. K. Jones, D. S. Novikov, and N. Shemesh. "Noninvasive quantification of axon radii using diffusion MRI". *eLife* 9 (Feb. 2020). Ed. by F. P. de Lange, B. Forstmann, B. Forstmann, S. Jbabdi, and R. Mulkern. Publisher: eLife Sciences Publications, Ltd, e49855. DOI: 10.7554/eLife.49855.

[16] L. M. Burcaw, E. Fieremans, and D. S. Novikov. "Mesoscopic structure of neuronal tracts from time-dependent diffusion". *NeuroImage* 114 (July 2015), pp. 18–37. DOI: 10.1016/j.neuroimage.2015.03.061.

[17] F. Aboitiz, A. B. Scheibel, R. S. Fisher, and E. Zaidel. "Fiber composition of the human corpus callosum". *Brain Research* 598.1 (Dec. 1992), pp. 143–153. DOI: 10.1016/0006-8993(92)90178-C.

[18] F. Sepehrband, D. C. Alexander, K. A. Clark, N. D. Kurniawan, Z. Yang, and D. C. Reutens. "Parametric Probability Distribution Functions for Axon Diameters of Corpus Callosum". *Frontiers in Neuroanatomy* 10 (May 2016), p. 59. DOI: 10.3389/fnana.2016.00059.

[19] J. Veraart, E. Fieremans, and D. S. Novikov. "On the scaling behavior of water diffusion in human brain white matter". *NeuroImage* 185 (Jan. 2019), pp. 379–387. DOI: 10.1016/j.neuroimage.2018.09.075.

[20] M. Pizzolato, E. J. Canales-Rodríguez, M. Andersson, and T. B. Dyrby. "Axial and radial axonal diffusivities and radii from single encoding strongly diffusion-weighted MRI". *Medical Image Analysis* 86 (May 2023), p. 102767. DOI: 10.1016/j.media.2023.102767.

[21] M. Palombo, A. Ianus, M. Guerreri, D. Nunes, D. C. Alexander, N. Shemesh, and H. Zhang. "SANDI: A compartment-based model for non-invasive apparent soma and neurite imaging by diffusion MRI". *NeuroImage* 215 (July 2020), p. 116835. DOI: 10.1016/j.neuroimage.2020.116835.

[22] G. J. Stanisz, G. A. Wright, R. M. Henkelman, and A. Szafer. "An analytical model of restricted diffusion in bovine optic nerve". *Magnetic Resonance in Medicine* 37.1 (1997), pp. 103–111. DOI: 10.1002/mrm.1910370115.

[23] H.-H. Lee, K. Yaros, J. Veraart, J. L. Pathan, F.-X. Liang, S. G. Kim, D. S. Novikov, and E. Fieremans. "Along-axon diameter variation and axonal orientation dispersion revealed with 3D electron microscopy: implications for quantifying brain white matter microstructure with histology and diffusion MRI". *Brain Structure and Function* 224.4 (May 2019), pp. 1469–1488. DOI: 10.1007/s00429-019-01844-6.

[24] H.-H. Lee, A. Papaioannou, S.-L. Kim, D. S. Novikov, and E. Fieremans. "A time-dependent diffusion MRI signature of axon caliber variations and beading". *Communications Biology* 3.1 (July 2020). Publisher: Nature Publishing Group, p. 354. DOI: 10.1038/s42003-020-1050-x.

[25] H.-H. Lee, Q. Tian, M. Sheft, R. Coronado-Leija, G. Ramos-Llorden, A. Abdollahzadeh, E. Fieremans, D. S. Novikov, and S. Y. Huang. "The effects of axonal beading and undulation on axonal diameter estimation from diffusion MRI: Insights from simulations in human axons segmented from three-dimensional electron microscopy". *NMR in Biomedicine* 37.4 (2024), e5087. DOI: 10.1002/nbm.5087.

[26] M. Andersson, H. M. Kjer, J. Rafael-Patino, A. Pacureanu, B. Pakkenberg, J.-P. Thiran, M. Ptito, M. Bech, A. Bjorholm Dahl, V. Andersen Dahl, and T. B. Dyrby. "Axon morphology is modulated by the local environment and impacts the noninvasive investigation of its structure–function relationship". *Proceedings of the National Academy of Sciences* 117.52 (Dec. 2020), pp. 33649–33659. DOI: 10.1073/pnas.2012533117.

[27] M. Andersson, M. Pizzolato, H. M. Kjer, K. F. Skodborg, H. Lundell, and T. B. Dyrby. "Does powder averaging remove dispersion bias in diffusion MRI diameter estimates within real 3D axonal architectures?" *NeuroImage* 248 (Mar. 2022), p. 118718. DOI: 10.1016/j.neuroimage.2021.118718.

[28] S. Winther, H. Lundell, J. Rafael-Patiño, M. Andersson, J.-P. Thiran, and T. B. Dyrby. "Susceptibility-induced internal gradients reveal axon morphology and cause anisotropic effects in the diffusion-weighted MRI signal". *Scientific Reports* 14.1 (Nov. 2024). Publisher: Nature Publishing Group, p. 29636. DOI: 10.1038/s41598-024-79043-5.

[29] M. Nilsson, J. Lätt, F. Ståhlberg, D. van Westen, and H. Hagslätt. "The importance of axonal undulation in diffusion MR measurements: a Monte Carlo simulation study". *NMR in biomedicine* 25.5 (May 2012), pp. 795–805. DOI: 10.1002/nbm.1795.

[30] I. Drobnjak, H. Zhang, A. Ianuş, E. Kaden, and D. C. Alexander. "PGSE, OGSE, and sensitivity to axon diameter in diffusion MRI: Insight from a simulation study". *Magnetic Resonance in Medicine* 75.2 (Feb. 2016), pp. 688–700. DOI: 10.1002/mrm.25631.

[31] H. Gudbjartsson and S. Patz. "The rician distribution of noisy mri data". *Magnetic Resonance in Medicine* 34.6 (1995), pp. 910–914. DOI: 10.1002/mrm.1910340618.

[32] J. Sijbers, A. den Dekker, P. Scheunders, and D. Van Dyck. "Maximum-likelihood estimation of Rician distribution parameters". *IEEE Transactions on Medical Imaging* 17.3 (June 1998). Conference Name: IEEE Transactions on Medical Imaging, pp. 357–361. DOI: 10.1109/42.712125.

[33] C. G. Koay and P. J. Basser. "Analytically exact correction scheme for signal extraction from noisy magnitude MR signals". *Journal of Magnetic Resonance* 179.2 (Apr. 2006), pp. 317–322. DOI: 10.1016/j.jmr.2006.01.016.

[34] D. Varadarajan and J. P. Haldar. "A Majorize-Minimize Framework for Rician and Non-Central Chi MR Images". *IEEE transactions on medical imaging* 34.10 (Oct. 2015), pp. 2191–2202. DOI: 10.1109/TMI.2015.2427157.

[35] S. N. Jespersen, H. Lundell, C. K. Sønderby, and T. B. Dyrby. "Orientationally invariant metrics of apparent compartment eccentricity from double pulsed field gradient diffusion experiments". *NMR in Biomedicine* 26.12 (2013), pp. 1647–1662. DOI: 10.1002/nbm.2999.

[36] E. Kaden, F. Kruggel, and D. C. Alexander. "Quantitative mapping of the per-axon diffusion coefficients in brain white matter". *Magnetic Resonance in Medicine* 75.4 (2016), pp. 1752–1763. DOI: 10.1002/mrm.25734.

[37] J. Mollink, M. Kleinnijenhuis, A.-M. v. Cappellen van Walsum, S. N. Sotiropoulos, M. Cottaar, C. Mirfin, M. P. Heinrich, M. Jenkinson, M. Pallebage-Gamarallage, O. Ansorge, S. Jbabdi, and K. L. Miller. "Evaluating fibre orientation dispersion in white matter: Comparison of diffusion MRI, histology and polarized light imaging". *NeuroImage* 157 (Aug. 2017), pp. 561–574. DOI: 10.1016/j.neuroimage.2017.06.001.

[38] M. Barakovic, M. Pizzolato, C. M. W. Tax, U. Rudrapatna, S. Magon, T. B. Dyrby, C. Granziera, J.-P. Thiran, D. K. Jones, and E. J. Canales-Rodríguez. "Estimating axon radius using diffusion-relaxation MRI: calibrating a surface-based relaxation model with histology". *Frontiers in Neuroscience* 17 (Aug. 2023). Publisher: Frontiers. DOI: 10.3389/fnins.2023.1209521.

[39] J. A. McNab, B. L. Edlow, T. Witzel, S. Y. Huang, H. Bhat, K. Heberlein, T. Feiweier, K. Liu, B. Keil, J. Cohen-Adad, M. D. Tisdall, R. D. Folkerth, H. C. Kinney, and L. L. Wald. "The Human Connectome Project and beyond: initial applications of 300 mT/m gradients". *NeuroImage* 80 (Oct. 2013), pp. 234–245. DOI: 10.1016/j.neuroimage.2013.05.074.

[40] D. Barazany, P. J. Basser, and Y. Assaf. "In vivo measurement of axon diameter distribution in the corpus callosum of rat brain". *Brain* 132.5 (May 2009), pp. 1210–1220. DOI: 10.1093/brain/awp042.

[41] A. Horowitz, D. Barazany, I. Tavor, M. Bernstein, G. Yovel, and Y. Assaf. "In vivo correlation between axon diameter and conduction velocity in the human brain". *Brain Structure and Function* 220.3 (May 2015), pp. 1777–1788. DOI: 10.1007/s00429-014-0871-0.

[42] S. Y. Huang, A. Nummenmaa, T. Witzel, T. Duval, J. Cohen-Adad, L. L. Wald, and J. A. McNab. "The impact of gradient strength on in vivo diffusion MRI estimates of axon diameter". *NeuroImage* 106 (Feb. 2015), pp. 464–472. DOI: 10.1016/j.neuroimage.2014.12.008.

[43] M. Barakovic, G. Girard, S. Schiavi, D. Romascano, M. Descoteaux, C. Granziera, D. K. Jones, G. M. Innocenti, J.-P. Thiran, and A. Daducci. "Bundle-Specific Axon Diameter Index as a New Contrast to Differentiate White Matter Tracts". *Frontiers in Neuroscience* 15 (June 2021). Publisher: Frontiers. DOI: 10.3389/fnins.2021.646034.

[44] D. Graf von Keyserlingk and U. Schramm. "Diameter of axons and thickness of myelin sheaths of the pyramidal tract fibres in the adult human medullary pyramid". *Anatomischer Anzeiger* 157.2 (1984), pp. 97–111.

[45] D. Liewald, R. Miller, N. Logothetis, H.-J. Wagner, and A. Schüz. "Distribution of axon diameters in cortical white matter: an electron-microscopic study on three human brains and a macaque". *Biological Cybernetics* 108.5 (Oct. 2014), pp. 541–557. DOI: 10.1007/s00422-014-0626-2.

[46] L. Mordhorst, M. Morozova, S. Papazoglou, B. Fricke, J. M. Oeschger, T. Tabarin, H. Rusch, C. Jäger, S. Geyer, N. Weiskopf, M. Morawski, and S. Mohammadi. "Towards a representative reference for MRI-based human axon radius assessment using light microscopy". *NeuroImage* 249 (Apr. 2022), p. 118906. DOI: 10.1016/j.neuroimage.2022.118906.

[47] L. Mordhorst, L. J. Edwards, M. Morozova, M. Ashtarayeh, T. Streubel, B. Fricke, F. J. Fritz, H. Rusch, C. Jäger, L. Starke, T. Gladytz, E. Tasbihi, J. S. Periquito, A. Pohlmann, H. Mushumba, K. Püschel, T. Niendorf, N. Weiskopf, M. Morawski, and S. Mohammadi. "MRI-scale histology validates spatial sensitivity of in-vivo MRI-based axon radius estimation". *Imaging Neuroscience* 3 (Dec. 2025), IMAG.a.1030. DOI: 10.1162/IMAG.a.1030.

[48] D. S. Novikov, J. Veraart, I. O. Jelescu, and E. Fieremans. "Rotationally-invariant mapping of scalar and orientational metrics of neuronal microstructure with diffusion MRI". *NeuroImage* 174 (July 2018), pp. 518–538. DOI: 10.1016/j.neuroimage.2018.03.006.

[49] R. J. Duchatel, C. Shannon Weickert, and P. A. Tooney. "White matter neuron biology and neuropathology in schizophrenia". *npj Schizophrenia* 5.1 (July 2019). Publisher: Nature Publishing Group, p. 10. DOI: 10.1038/s41537-019-0078-8.

[50] D. Richards, C. E. Clarke, and T. Clark. *The human brain and its disorders*. Oxford ; New York: Oxford University Press, 2007. ISBN: 978-0-19-929984-3.

[51] R. D. Fields. "White matter matters". *Scientific American* 298.3 (Mar. 2008), pp. 42–49.

[52] D. U. Silverthorn. *Human Physiology: An Integrated Approach*. Pearson, 2016. ISBN: 978-0-321-98122-6.

[53] J. B. Hursh. "Conduction velocity and diameter of nerve fibers". *American Journal of Physiology-Legacy Content* 127.1 (July 1939). Publisher: American Physiological Society, pp. 131–139. DOI: 10.1152/ajplegacy.1939.127.1.131.

[54] S. G. Waxman, J. D. Kocsis, and P. K. Stys. *The axon: structure, function, and pathophysiology*. New York: Oxford University Press, 1995. ISBN: 978-0-19-986580-2.

[55] "White matter neurobiology". *White Matter Dementia*. Ed. by C. M. Filley. Cambridge: Cambridge University Press, 2016, pp. 17–26. ISBN: 978-1-139-54887-8. DOI: 10.1017/CBO9781139548878.005.

[56] C. M. Filley. "Neurobiology of White Matter Disorders". *Diffusion MRI: Theory, Methods, and Applications*. Ed. by P. Jones Derek K. Oxford University Press, Nov. 2010, p. 0. ISBN: 978-0-19-536977-9. DOI: 10.1093/med/9780195369779.003.0002.

[57] E. R. Kandel, J. H. Schwartz, T. Jessell, S. A. Siegelbaum, and A. J. Hudspeth. *Principles of neural science*. Ed. by E. R. Kandel, J. H. Schwartz, T. Jessell, S. A. Siegelbaum, A. J. Hudspeth, and S. H. Mack. Fifth edition. New York ; Lisbon ; London: McGraw-Hill Medical, 2013. ISBN: 978-0-07-139011-8.

[58] J. Pawley. *Handbook of Biological Confocal Microscopy*. Springer Science & Business Media, Dec. 2012. ISBN: 978-1-4615-7133-9.

[59] P. Ruthig, D. E. v. d. Planitz, M. Morozova, K. Reimann, C. Jäger, T. Reinert, S. Mohammadi, N. Weiskopf, E. Kirilina, and M. Morawski. “Short-range human cortico-cortical white matter fibers have thinner axons and are less myelinated compared to long-range fibers despite a similar g-ratio”. *PLOS Biology* 23.8 (Aug. 2025). Publisher: Public Library of Science, e3002906. DOI: 10.1371/journal.pbio.3002906.

[60] M. L. Jones, J. D. Bancroft, and M. Gamble. “10 - Connective Tissues and Stains”. *Theory and Practice of Histological Techniques (Sixth Edition)*. Ed. by J. D. Bancroft and M. Gamble. Edinburgh: Churchill Livingstone, Jan. 2008, pp. 135–160. ISBN: 978-0-443-10279-0. DOI: 10.1016/B978-0-443-10279-0.50017-8.

[61] A. Peters, S. L. Palay, and H. d. Webster. *The Fine Structure of the Nervous System: Neurons and Their Supporting Cells*. Oxford University Press, 1991. ISBN: 978-0-19-506571-8.

[62] J. J. Bozzola and L. D. Russell. *Electron Microscopy: Principles and Techniques for Biologists*. Jones & Bartlett Learning, 1999. ISBN: 978-0-7637-0192-5.

[63] L. G. Shapiro and G. C. Stockman. *Computer Vision*. Prentice Hall, 2001. ISBN: 978-0-13-030796-5.

[64] S. Minaee, Y. Boykov, F. Porikli, A. Plaza, N. Kehtarnavaz, and D. Terzopoulos. “Image Segmentation Using Deep Learning: A Survey”. *IEEE Transactions on Pattern Analysis and Machine Intelligence* 44.7 (July 2022), pp. 3523–3542. DOI: 10.1109/TPAMI.2021.3059968.

[65] A. Rosenfeld and J. L. Pfaltz. “Sequential Operations in Digital Picture Processing”. *J. ACM* 13.4 (Oct. 1966), pp. 471–494. DOI: 10.1145/321356.321357.

[66] S. Beucher and F. Meyer. “The Morphological Approach to Segmentation: The Watershed Transformation”. *Mathematical Morphology in Image Processing*. Num Pages: 49. CRC Press, 1992. ISBN: 978-1-315-21461-0.

[67] E. Upschulte, S. Harmeling, K. Amunts, and T. Dickscheid. “Contour proposal networks for biomedical instance segmentation”. *Medical Image Analysis* 77 (Apr. 2022), p. 102371. DOI: 10.1016/j.media.2022.102371.

[68] K. He, G. Gkioxari, P. Dollár, and R. Girshick. “Mask R-CNN”. *2017 IEEE International Conference on Computer Vision (ICCV)*. ISSN: 2380-7504. Oct. 2017, pp. 2980–2988. DOI: 10.1109/ICCV.2017.322.

[69] I. Goodfellow, Y. Bengio, and A. Courville. *Deep Learning*. Ed. by F. Bach. Adaptive Computation and Machine Learning series. Cambridge, MA, USA: MIT Press, Nov. 2016. ISBN: 978-0-262-03561-3.

[70] W. S. McCulloch and W. Pitts. “A logical calculus of the ideas immanent in nervous activity”. *The bulletin of mathematical biophysics* 5.4 (Dec. 1943), pp. 115–133. DOI: 10.1007/BF02478259.

[71] F. Rosenblatt. “The perceptron: A probabilistic model for information storage and organization in the brain”. *Psychological Review* 65.6 (1958). Place: US Publisher: American Psychological Association, pp. 386–408. DOI: 10.1037/h0042519.

[72] V. Nair and G. E. Hinton. “Rectified linear units improve restricted boltzmann machines”. *Proceedings of the 27th International Conference on International Conference on Machine Learning*. ICML’10. Madison, WI, USA: Omnipress, June 2010, pp. 807–814. ISBN: 978-1-60558-907-7.

[73] K. Fukushima. “Neocognitron: A self-organizing neural network model for a mechanism of pattern recognition unaffected by shift in position”. *Biological Cybernetics* 36.4 (Apr. 1980), pp. 193–202. DOI: 10.1007/BF00344251.

[74] Y. L. Cun, B. Boser, J. S. Denker, R. E. Howard, W. Habbard, L. D. Jackel, and D. Henderson. “Handwritten digit recognition with a back-propagation network”. *Advances in neural information processing systems 2*. San Francisco, CA, USA: Morgan Kaufmann Publishers Inc., June 1990, pp. 396–404. ISBN: 978-1-55860-100-0.

[75] O. Ronneberger, P. Fischer, and T. Brox. “U-Net: Convolutional Networks for Biomedical Image Segmentation”. *Medical Image Computing and Computer-Assisted Intervention – MICCAI 2015*. Ed. by N. Navab, J. Hornegger, W. M. Wells, and A. F. Frangi. Lecture Notes in Computer Science. Cham: Springer International Publishing, 2015, pp. 234–241. ISBN: 978-3-319-24574-4. DOI: 10.1007/978-3-319-24574-4_28.

[76] E. Shelhamer, J. Long, and T. Darrell. “Fully Convolutional Networks for Semantic Segmentation”. *IEEE Trans. Pattern Anal. Mach. Intell.* 39.4 (Apr. 2017), pp. 640–651. DOI: 10.1109/TPAMI.2016.2572683.

[77] Zhou and Chellappa. “Computation of optical flow using a neural network”. *IEEE 1988 International Conference on Neural Networks*. July 1988, 71–78 vol.2. DOI: 10.1109/ICNN.1988.23914.

[78] Y. Lecun, L. Bottou, Y. Bengio, and P. Haffner. “Gradient-based learning applied to document recognition”. *Proceedings of the IEEE* 86.11 (Nov. 1998), pp. 2278–2324. DOI: 10.1109/5.726791.

[79] D. P. Kingma and J. Ba. *Adam: A Method for Stochastic Optimization*. arXiv:1412.6980 [cs]. Jan. 2017. DOI: 10.48550/arXiv.1412.6980. URL: http://arxiv.org/abs/1412.6980 (visited on 08/27/2025).

[80] I. Sutskever, J. Martens, G. Dahl, and G. Hinton. “On the importance of initialization and momentum in deep learning”. *Proceedings of the 30th International Conference on Machine Learning*. ISSN: 1938-7228. PMLR, May 2013, pp. 1139–1147.

[81] N. Srivastava, G. Hinton, A. Krizhevsky, I. Sutskever, and R. Salakhutdinov. “Dropout: A Simple Way to Prevent Neural Networks from Overfitting”. *Journal of Machine Learning Research* 15.56 (2014), pp. 1929–1958.

[82] K. L. West, N. D. Kelm, R. P. Carson, and M. D. Does. "A revised model for estimating g-ratio from MRI". *NeuroImage* 125 (Jan. 2016), pp. 1155–1158. DOI: 10.1016/j.neuroimage.2015.08.017.

[83] A. Abdollahzadeh, I. Belevich, E. Jokitalo, A. Sierra, and J. Tohka. "DeepACSON automated segmentation of white matter in 3D electron microscopy". *Communications Biology* 4.1 (Feb. 2021). Number: 1 Publisher: Nature Publishing Group, pp. 1–14. DOI: 10.1038/s42003-021-01699-w.

[84] I. I. Rabi, J. R. Zacharias, S. Millman, and P. Kusch. "A New Method of Measuring Nuclear Magnetic Moment". *Physical Review* 53.4 (Feb. 1938). Publisher: American Physical Society, pp. 318–318. DOI: 10.1103/PhysRev.53.318.

[85] E. M. Purcell, H. C. Torrey, and R. V. Pound. "Resonance Absorption by Nuclear Magnetic Moments in a Solid". *Physical Review* 69.1-2 (Jan. 1946). Publisher: American Physical Society, pp. 37–38. DOI: 10.1103/PhysRev.69.37.

[86] F. Bloch. "Nuclear Induction". *Physical Review* 70.7-8 (Oct. 1946). Publisher: American Physical Society, pp. 460–474. DOI: 10.1103/PhysRev.70.460.

[87] P. E. Watson, I. D. Watson, and R. D. Batt. "Total body water volumes for adult males and females estimated from simple anthropometric measurements". *The American Journal of Clinical Nutrition* 33.1 (Jan. 1980), pp. 27–39. DOI: 10.1093/ajcn/33.1.27.

[88] R. W. Brown, Y.-C. N. Cheng, E. M. Haacke, M. R. Thompson, and R. Venkatesan. *Magnetic Resonance Imaging: Physical Principles and Sequence Design*. John Wiley & Sons, May 2014. ISBN: 978-1-118-63397-7.

[89] P. T. Callaghan. "Physics of Diffusion". *Diffusion MRI: Theory, Methods, and Applications*. Ed. by P. Jones Derek K. Oxford University Press, Nov. 2010, p. 0. ISBN: 978-0-19-536977-9. DOI: 10.1093/med/9780195369779.003.0004.

[90] A. Fick. "Ueber Diffusion". *Annalen der Physik* 170.1 (1855), pp. 59–86. DOI: 10.1002/andp.18551700105.

[91] A. Einstein. "Zur Theorie der Brownschen Bewegung". *Annalen der Physik* 324.2 (Jan. 1906), pp. 371–381. DOI: 10.1002/andp.19063240208.

[92] H. C. Torrey. "Bloch Equations with Diffusion Terms". *Physical Review* 104.3 (Nov. 1956). Publisher: American Physical Society, pp. 563–565. DOI: 10.1103/PhysRev.104.563.

[93] V. G. Kiselev. "The Cumulant Expansion: An Overarching Mathematical Framework For Understanding Diffusion NMR". *Diffusion MRI: Theory, Methods, and Applications*. Ed. by P. Jones Derek K. Oxford University Press, Nov. 2010, p. 0. ISBN: 978-0-19-536977-9. DOI: 10.1093/med/9780195369779.003.0010.

[94] P. P. Mitra. "Multiple wave-vector extensions of the NMR pulsed-field-gradient spin-echo diffusion measurement". *Physical Review B* 51.21 (June 1995). Publisher: American Physical Society, pp. 15074–15078. DOI: 10.1103/PhysRevB.51.15074.

[95] C. H. Neuman. "Spin echo of spins diffusing in a bounded medium". *The Journal of Chemical Physics* 60.11 (1974), pp. 4508–4511. DOI: 10.1063/1.1680931.

[96] B. Balinov, B. Jonsson, P. Linse, and O. Soderman. "The NMR Self-Diffusion Method Applied to Restricted Diffusion. Simulation of Echo Attenuation from Molecules in Spheres and between Planes". *Journal of Magnetic Resonance, Series A* 104.1 (Aug. 1993), pp. 17–25. DOI: 10.1006/jmra.1993.1184.

[97] P. Van Gelderen, D. Despres, P. C. M. Vanzijl, and C. T. W. Moonen. "Evaluation of Restricted Diffusion in Cylinders. Phosphocreatine in Rabbit Leg Muscle". *Journal of Magnetic Resonance, Series B* 103.3 (Mar. 1994), pp. 255–260. DOI: 10.1006/jmrb.1994.1038.

[98] J. E. Tanner. "Self diffusion of water in frog muscle". *Biophysical Journal* 28.1 (Oct. 1979), pp. 107–116. DOI: 10.1016/S0006-3495(79)85162-0.

[99] E. O. Stejskal. "Use of Spin Echoes in a Pulsed Magnetic-Field Gradient to Study Anisotropic, Restricted Diffusion and Flow". *The Journal of Chemical Physics* 43.10 (1965), pp. 3597–3603. DOI: 10.1063/1.1696526.

[100] O. Dietrich, A. Biffar, A. Baur-Melnyk, and M. F. Reiser. "Technical aspects of MR diffusion imaging of the body". *European Journal of Radiology* 76.3 (Dec. 2010). Publisher: Elsevier, pp. 314–322. DOI: 10.1016/j.ejrad.2010.02.018.

[101] P. Mansfield. "Multi-planar image formation using NMR spin echoes". *Journal of Physics C: Solid State Physics* 10.3 (Feb. 1977), pp. L55–L58. DOI: 10.1088/0022-3719/10/3/004.

[102] D. Le Bihan. "Magnetic Resonance Diffusion Imaging: Introduction and Concepts". *Diffusion MRI: Theory, Methods, and Applications*. Ed. by P. Jones Derek K. Oxford University Press, Nov. 2010, p. 0. ISBN: 978-0-19-536977-9. DOI: 10.1093/med/9780195369779.003.0005.

[103] P. Jezzard and R. S. Balaban. "Correction for geometric distortion in echo planar images from B0 field variations". *Magnetic Resonance in Medicine* 34.1 (1995), pp. 65–73. DOI: 10.1002/mrm.1910340111.

[104] C. Eichner, S. F. Cauley, J. Cohen-Adad, H. E. Möller, R. Turner, K. Setsompop, and L. L. Wald. "Real diffusion-weighted MRI enabling true signal averaging and increased diffusion contrast". *NeuroImage* 122 (Nov. 2015), pp. 373–384. DOI: 10.1016/j.neuroimage.2015.07.074.

[105] Q. Fan, A. Nummenmaa, T. Witzel, N. Ohringer, Q. Tian, K. Setsompop, E. C. Klawiter, B. R. Rosen, L. L. Wald, and S. Y. Huang. "Axon diameter index estimation independent of fiber orientation distribution using high-gradient diffusion MRI". *NeuroImage* 222 (Nov. 2020), p. 117197. DOI: 10.1016/j.neuroimage.2020.117197.

[106] J. P. Manzano Patron, S. Moeller, J. L. Andersson, K. Ugurbil, E. Yacoub, and S. N. Sotiropoulos. "Denoising diffusion MRI: Considerations and implications for analysis". *Imaging Neuroscience* 2 (Jan. 2024), pp. 1–29. DOI: "10.1162/imag_a_00060".

[107] D. C. Alexander, C. Pierpaoli, P. J. Basser, and J. C. Gee. "Spatial transformations of diffusion tensor magnetic resonance images". *IEEE transactions on medical imaging* 20.11 (Nov. 2001), pp. 1131–1139. DOI: 10.1109/42.963816.

[108] H. Zhang, T. Schneider, C. A. Wheeler-Kingshott, and D. C. Alexander. "NODDI: Practical in vivo neurite orientation dispersion and density imaging of the human brain". *NeuroImage* 61.4 (July 2012), pp. 1000–1016. DOI: 10.1016/j.neuroimage.2012.03.072.

[109] J. W. Gibbs. "Fourier's Series". *Nature* 59 (Apr. 1899), p. 606. DOI: 10.1038/059606a0.

[110] L. Czervionke, J. Czervionke, D. Daniels, and V. Haughton. "Characteristic features of MR truncation artifacts". *American Journal of Roentgenology* 151.6 (Dec. 1988), pp. 1219–1228. DOI: 10.2214/ajr.151.6.1219.

[111] T. Lei. "Gibbs ringing artifact, spatial correlation, and spatial resolution in MRI". *Medical Imaging 2004: Physics of Medical Imaging*. Vol. 5368. SPIE, May 2004, pp. 837–847. DOI: 10.1117/12.536558.

[112] E. Kellner, B. Dhital, V. G. Kiselev, and M. Reisert. "Gibbs-ringing artifact removal based on local subvoxel-shifts". *Magnetic Resonance in Medicine* 76.5 (Nov. 2016), pp. 1574–1581. DOI: 10.1002/mrm.26054.

[113] J. L. R. Andersson, S. Skare, and J. Ashburner. "How to correct susceptibility distortions in spin-echo echo-planar images: application to diffusion tensor imaging". *NeuroImage* 20.2 (Oct. 2003), pp. 870–888. DOI: 10.1016/S1053-8119(03)00336-7.

[114] C. B. Ahn and Z. H. Cho. "Analysis of the eddy-current induced artifacts and the temporal compensation in nuclear magnetic resonance imaging". *IEEE transactions on medical imaging* 10.1 (1991), pp. 47–52. DOI: 10.1109/42.75610.

[115] J. L. R. Andersson, M. S. Graham, E. Zsoldos, and S. N. Sotiropoulos. "Incorporating outlier detection and replacement into a non-parametric framework for movement and distortion correction of diffusion MR images". *NeuroImage* 141 (Nov. 2016), pp. 556–572. DOI: 10.1016/j.neuroimage.2016.06.058.

[116] G. David, B. Fricke, J. M. Oeschger, L. Ruthotto, F. J. Fritz, O. Ohana, L. Mordhorst, T. Sauvigny, P. Freund, K. Tabelow, and S. Mohammadi. "ACID: A comprehensive toolbox for image processing and modeling of brain, spinal cord, and ex vivo diffusion MRI data". *Imaging Neuroscience* 2 (Sept. 2024), pp. 1–34. DOI: 10.1162/imag_a_00288.

[117] J. L. R. Andersson, M. S. Graham, I. Drobnjak, H. Zhang, N. Filippini, and M. Bastiani. "Towards a comprehensive framework for movement and distortion correction of diffusion MR images: Within volume movement". *NeuroImage* 152 (May 2017), pp. 450–466. DOI: 10.1016/j.neuroimage.2017.02.085.

[118] A. Janke, H. Zhao, G. J. Cowin, G. J. Galloway, and D. M. Doddrell. "Use of spherical harmonic deconvolution methods to compensate for nonlinear gradient effects on MRI images". *Magnetic Resonance in Medicine* 52.1 (2004), pp. 115–122. DOI: 10.1002/mrm.20122.

[119] J. Jovicich, S. Czanner, D. Greve, E. Haley, A. van der Kouwe, R. Gollub, D. Kennedy, F. Schmitt, G. Brown, J. MacFall, B. Fischl, and A. Dale. "Reliability in multi-site structural MRI studies: Effects of gradient non-linearity correction on phantom and human data". *NeuroImage* 30.2 (Apr. 2006), pp. 436–443. DOI: 10.1016/j.neuroimage.2005.09.046.

[120] R. Bammer, M. Markl, A. Barnett, B. Acar, M. Alley, N. Pelc, G. Glover, and M. Moseley. "Analysis and generalized correction of the effect of spatial gradient field distortions in diffusion-weighted imaging". *Magnetic Resonance in Medicine* 50.3 (2003), pp. 560–569. DOI: 10.1002/mrm.10545.

[121] D. S. Novikov, V. G. Kiselev, and S. N. Jespersen. "On modeling". *Magnetic resonance in medicine* 79.6 (June 2018), pp. 3172–3193. DOI: 10.1002/mrm.27101.

[122] P. J. Basser, J. Mattiello, and D. LeBihan. "MR diffusion tensor spectroscopy and imaging". *Biophysical Journal* 66.1 (Jan. 1994), pp. 259–267. DOI: 10.1016/S0006-3495(94)80775-1.

[123] D. K. Jones and P. J. Basser. ""Squashing peanuts and smashing pumpkins": How noise distorts diffusion-weighted MR data". *Magnetic Resonance in Medicine* 52.5 (2004), pp. 979–993. DOI: 10.1002/mrm.20283.

[124] S. Mori and P. B. Barker. "Diffusion magnetic resonance imaging: Its principle and applications". *The Anatomical Record* 257.3 (1999), pp. 102–109. DOI: 10.1002/(SICI)1097-0185(19990615)257:3<102::AID-AR7>3.0.CO;2-6.

[125] J. H. Jensen, J. A. Helpern, A. Ramani, H. Lu, and K. Kaczynski. "Diffusional kurtosis imaging: the quantification of non-gaussian water diffusion by means of magnetic resonance imaging". *Magnetic Resonance in Medicine* 53.6 (June 2005), pp. 1432–1440. DOI: 10.1002/mrm.20508.

[126] E. S. Hui, E. Fieremans, J. H. Jensen, A. Tabesh, W. Feng, L. Bonilha, M. V. Spampinato, R. Adams, and J. A. Helpern. "Stroke assessment with diffusional kurtosis imaging". *Stroke* 43.11 (Nov. 2012), pp. 2968–2973. DOI: 10.1161/STROKEAHA.112.657742.

[127] D. S. Novikov, E. Fieremans, S. N. Jespersen, and V. G. Kiselev. "Quantifying brain microstructure with diffusion MRI: Theory and parameter estimation". *NMR in Biomedicine* 32.4 (2019), e3998. DOI: 10.1002/nbm.3998.

[128] J. Veraart, D. S. Novikov, and E. Fieremans. "TE dependent Diffusion Imaging (TEdDI) distinguishes between compartmental T2 relaxation times". *NeuroImage* 182 (Nov. 2018), pp. 360–369. DOI: 10.1016/j.neuroimage.2017.09.030.

[129] C. D. Kroenke, J. J. H. Ackerman, and D. A. Yablonskiy. "On the nature of the NAA diffusion attenuated MR signal in the central nervous system". *Magnetic Resonance in Medicine* 52.5 (Nov. 2004), pp. 1052–1059. DOI: 10.1002/mrm.20260.

[130] S. N. Jespersen, C. D. Kroenke, L. Østergaard, J. J. H. Ackerman, and D. A. Yablonskiy. "Modeling dendrite density from magnetic resonance diffusion measurements". *NeuroImage* 34.4 (Feb. 2007), pp. 1473–1486. DOI: 10.1016/j.neuroimage.2006.10.037.

[131] M. Reisert, E. Kellner, B. Dhital, J. Hennig, and V. G. Kiselev. "Disentangling micro from mesostructure by diffusion MRI: A Bayesian approach". *NeuroImage* 147 (Feb. 2017), pp. 964–975. DOI: 10.1016/j.neuroimage.2016.09.058.

[132] K. J. Packer and C. Rees. "Pulsed NMR studies of restricted diffusion. I. Droplet size distributions in emulsions". *Journal of Colloid and Interface Science* 40.2 (Aug. 1972), pp. 206–218. DOI: 10.1016/0021-9797(72)90010-0.

[133] J. Veraart and D. S. Novikov. *AxonRadiusMapping*. 2019. URL: https://github.com/NYU-DiffusionMRI/AxonRadiusMapping (visited on 02/11/2024).

[134] K. G. Schilling, V. Janve, Y. Gao, I. Stepniewska, B. A. Landman, and A. W. Anderson. "Histological Validation of Diffusion MRI Fiber Orientation Distributions and Dispersion". *NeuroImage* 165 (Jan. 2018), pp. 200–221. DOI: 10.1016/j.neuroimage.2017.10.046.

[135] K. Sato, A. Kerever, K. Kamagata, K. Tsuruta, R. Irie, K. Tagawa, H. Okazawa, E. Arikawa-Hirasawa, N. Nitta, I. Aoki, and S. Aoki. "Understanding microstructure of the brain by comparison of neurite orientation dispersion and density imaging (NODDI) with transparent mouse brain". *Acta Radiologica Open* 6.4 (Apr. 2017), p. 2058460117703816. DOI: 10.1177/2058460117703816.

[136] F. Grussu, T. Schneider, C. Tur, R. L. Yates, M. Tachrount, A. Ianuş, M. C. Yiannakas, J. Newcombe, H. Zhang, D. C. Alexander, G. C. DeLuca, and C. A. M. Gandini Wheeler-Kingshott. "Neurite dispersion: a new marker of multiple sclerosis spinal cord pathology?" *Annals of Clinical and Translational Neurology* 4.9 (Sept. 2017), pp. 663–679. DOI: 10.1002/acn3.445.

[137] A. Seehaus, A. Roebroeck, M. Bastiani, L. Fonseca, H. Bratzke, N. Lori, A. Vilanova, R. Goebel, and R. Galuske. "Histological validation of high-resolution DTI in human post mortem tissue". *Frontiers in Neuroanatomy* 9 (July 2015), p. 98. DOI: 10.3389/fnana.2015.00098.

[138] T. B. Leergaard, N. S. White, A. d. Crespigny, I. Bolstad, H. D'Arceuil, J. G. Bjaalie, and A. M. Dale. "Quantitative Histological Validation of Diffusion MRI Fiber Orientation Distributions in the Rat Brain". *PLOS ONE* 5.1 (Jan. 2010). Publisher: Public Library of Science, e8595. DOI: 10.1371/journal.pone.0008595.

[139] A. S. Choe, I. Stepniewska, D. C. Colvin, Z. Ding, and A. W. Anderson. "Validation of diffusion tensor MRI in the central nervous system using light microscopy: quantitative comparison of fiber properties". *NMR in biomedicine* 25.7 (July 2012), pp. 900–908. DOI: 10.1002/nbm.1810.

[140] I. O. Jelescu and M. D. Budde. "Design and validation of diffusion MRI models of white matter". *Frontiers in physics* 28 (Nov. 2017), p. 61. DOI: 10.3389/fphy.2017.00061.

[141] W. Alyami, A. Kyme, and R. Bourne. "Histological Validation of MRI: A Review of Challenges in Registration of Imaging and Whole-Mount Histopathology". *Journal of Magnetic Resonance Imaging* 55.1 (2022), pp. 11–22. DOI: 10.1002/jmri.27409.

[142] H. H. Ong, A. C. Wright, S. L. Wehrli, A. Souza, E. D. Schwartz, S. N. Hwang, and F. W. Wehrli. "Indirect measurement of regional axon diameter in excised mouse spinal cord with q-space imaging: Simulation and experimental studies". *NeuroImage* 40.4 (May 2008), pp. 1619–1632. DOI: 10.1016/j.neuroimage.2008.01.017.

[143] H. H. Ong and F. W. Wehrli. "Quantifying axon diameter and intra-cellular volume fraction in excised mouse spinal cord with q-space imaging". *NeuroImage* 51.4 (July 2010), pp. 1360–1366. DOI: 10.1016/j.neuroimage.2010.03.063.

[144] T. B. Dyrby, L. V. S gaard, M. G. Hall, M. Ptito, and D. C. Alexander. "Contrast and stability of the axon diameter index from microstructure imaging with diffusion MRI". *Magnetic Resonance in Medicine* 70.3 (2013), pp. 711–721. DOI: 10.1002/mrm.24501.

[145] J. Xu, H. Li, K. D. Harkins, X. Jiang, J. Xie, H. Kang, M. D. Does, and J. C. Gore. "Mapping mean axon diameter and axonal volume fraction by MRI using temporal diffusion spectroscopy". *NeuroImage* 103 (Dec. 2014), pp. 10–19. DOI: 10.1016/j.neuroimage.2014.09.006.

[146] Q. Fan, Q. Tian, N. A. Ohringer, A. Nummenmaa, T. Witzel, S. M. Tobyne, E. C. Klawiter, C. Mekkaoui, B. R. Rosen, L. L. Wald, D. H. Salat, and S. Y. Huang. "Age-related alterations in axonal microstructure in the corpus callosum measured by high-gradient diffusion MRI". *NeuroImage* 191 (May 2019), pp. 325–336. DOI: 10.1016/j.neuroimage.2019.02.036.

[147] A.-S. Lamantia and P. Rakic. "Cytological and quantitative characteristics of four cerebral commissures in the rhesus monkey". *Journal of Comparative Neurology* 291.4 (1990), pp. 520–537. DOI: 10.1002/cne.902910404.

[148] A. Shapson-Coe, M. Januszewski, D. R. Berger, A. Pope, Y. Wu, T. Blakely, R. L. Schalek, P. H. Li, S. Wang, J. Maitin-Shepard, N. Karlupia, S. Dorkenwald, E. Sjostedt, L. Leavitt, D. Lee, J. Troidl, F. Collman, L. Bailey, A. Fitzmaurice, R. Kar, B. Field, H. Wu, J. Wagner-Carena, D. Aley, J. Lau, Z. Lin, D. Wei, H. Pfister, A. Peleg, V. Jain, and J. W. Lichtman. "A petavoxel fragment of human cerebral cortex reconstructed at nanoscale resolution". *Science* 384.6696 (May 2024). Publisher: American Association for the Advancement of Science, eadk4858. DOI: 10.1126/science.adk4858.

[149] Q. Tian, C. Ngamsombat, H.-H. Lee, D. R. Berger, Y. Wu, Q. Fan, B. Bilgic, Z. Li, D. S. Novikov, E. Fieremans, B. R. Rosen, J. W. Lichtman, and S. Y. Huang. "Quantifying axonal features of human superficial white matter from three-dimensional multibeam serial electron microscopy data assisted by deep learning". *NeuroImage* 313 (June 2025), p. 121212. DOI: 10.1016/j.neuroimage.2025.121212.

[150] H.-H. Lee, S. N. Jespersen, E. Fieremans, and D. S. Novikov. "The impact of realistic axonal shape on axon diameter estimation using diffusion MRI". *NeuroImage* 223 (Dec. 2020), p. 117228. DOI: 10.1016/j.neuroimage.2020.117228.

[151] A. Zaimi, M. Wabartha, V. Herman, P.-L. Antonsanti, C. S. Perone, and J. Cohen-Adad. "AxonDeepSeg: automatic axon and myelin segmentation from microscopy data using convolutional neural networks". *Scientific Reports* 8.1 (Dec. 2018), p. 3816. DOI: 10.1038/s41598-018-22181-4.

[152] M. Weigert, U. Schmidt, R. Haase, K. Sugawara, and G. Myers. "Star-convex Polyhedra for 3D Object Detection and Segmentation in Microscopy". *2020 IEEE Winter Conference on Applications of Computer Vision (WACV)*. ISSN: 2642-9381. Mar. 2020, pp. 3655–3662. DOI: 10.1109/WACV45572.2020.9093435.

[153] M. Weigert and U. Schmidt. "Nuclei Instance Segmentation and Classification in Histopathology Images with Stardist". *2022 IEEE International Symposium on Biomedical Imaging Challenges (ISBIC)*. Mar. 2022, pp. 1–4. DOI: 10.1109/ISBIC56247.2022.9854534.

[154] U. Schmidt, M. Weigert, C. Broaddus, and G. Myers. “Cell Detection with Star-Convex Polygons”. *Medical Image Computing and Computer Assisted Intervention – MICCAI 2018*. Ed. by A. F. Frangi, J. A. Schnabel, C. Davatzikos, C. Alberola-López, and G. Fichtinger. Cham: Springer International Publishing, 2018, pp. 265–273. ISBN: 978-3-030-00934-2. DOI: 10.1007/978-3-030-00934-2_30.

[155] C.-W. Wang, W.-T. Lee, and T.-S. Su. “A survey of deep learning methods on cell instance segmentation”. *Neural Computing and Applications* (Apr. 2025). DOI: 10.1007/s00521-025-11119-3.

[156] F. Krikid, H. Rositi, and A. Vacavant. “State-of-the-Art Deep Learning Methods for Microscopic Image Segmentation: Applications to Cells, Nuclei, and Tissues”. *Journal of Imaging* 10.12 (Dec. 2024). Number: 12 Publisher: Multidisciplinary Digital Publishing Institute, p. 311. DOI: 10.3390/jimaging10120311.

[157] M. Nilsson, S. Lasič, I. Drobnjak, D. Topgaard, and C.-F. Westin. “Resolution limit of cylinder diameter estimation by diffusion MRI: The impact of gradient waveform and orientation dispersion”. *NMR in Biomedicine* 30.7 (2017), e3711. DOI: 10.1002/nbm.3711.

[158] A. Abdollahzadeh, I. Belevich, E. Jokitalo, J. Tohka, and A. Sierra. “Automated 3D Axonal Morphometry of White Matter”. *Scientific Reports* 9.1 (Apr. 2019). Publisher: Nature Publishing Group, p. 6084. DOI: 10.1038/s41598-019-42648-2.

[159] S. Pajevic and P. J. Basser. “An Optimum Principle Predicts the Distribution of Axon Diameters in Normal White Matter”. *PLOS ONE* 8.1 (Jan. 2013). Publisher: Public Library of Science, e54095. DOI: 10.1371/journal.pone.0054095.

[160] N. S. Gov. “Physical model for the width distribution of axons”. *The European Physical Journal E* 29.3 (July 2009), pp. 337–344. DOI: 10.1140/epje/i2009-10476-8.

[161] H. Zhang, P. L. Hubbard, G. J. M. Parker, and D. C. Alexander. “Axon diameter mapping in the presence of orientation dispersion with diffusion MRI”. *NeuroImage* 56.3 (June 2011), pp. 1301–1315. DOI: 10.1016/j.neuroimage.2011.01.084.

[162] H. Gast, A. Horowitz, R. Krupnik, D. Barazany, S. Lifshits, S. Ben-Amitay, and Y. Assaf. “A Method for In-Vivo Mapping of Axonal Diameter Distributions in the Human Brain Using Diffusion-Based Axonal Spectrum Imaging (AxSI)”. *Neuroinformatics* 21.3 (July 2023), pp. 469–482. DOI: 10.1007/s12021-023-09630-w.

[163] M. Veldmann, L. J. Edwards, K. J. Pine, P. Ehses, M. Ferreira, N. Weiskopf, and T. Stoecker. "Improving MR axon radius estimation in human white matter using spiral acquisition and field monitoring". *Magnetic Resonance in Medicine* n/a.n/a (May 2024). Publisher: John Wiley & Sons, Ltd. DOI: 10.1002/mrm.30180.

[164] J. Kärger. "NMR self-diffusion studies in heterogeneous systems". *Advances in Colloid and Interface Science* 23 (Aug. 1985), pp. 129–148. DOI: 10.1016/0001-8686(85)80018-X.

[165] J. H. Jensen, G. Russell Glenn, and J. A. Helpern. "Fiber ball imaging". *NeuroImage* 124.Pt A (Jan. 2016), pp. 824–833. DOI: 10.1016/j.neuroimage.2015.09.049.

[166] J. C. Mazziotta, A. W. Toga, A. Evans, P. Fox, and J. Lancaster. "A probabilistic atlas of the human brain: theory and rationale for its development. The International Consortium for Brain Mapping (ICBM)". *NeuroImage* 2.2 (June 1995), pp. 89–101. DOI: 10.1006/nimg.1995.1012.

[167] Y. Tang, J. R. Nyengaard, B. Pakkenberg, and H. J. G. Gundersen. "Age-Induced White Matter Changes in the Human Brain: A Stereological Investigation". *Neurobiology of Aging* 18.6 (Nov. 1997), pp. 609–615. DOI: 10.1016/S0197-4580(97)00155-3.

[168] S. B. Vos, D. K. Jones, M. A. Viergever, and A. Leemans. "Partial volume effect as a hidden covariate in DTI analyses". *NeuroImage* 55.4 (Apr. 2011), pp. 1566–1576. DOI: 10.1016/j.neuroimage.2011.01.048.

[169] T. B. Dyrby, G. M. Innocenti, M. Bech, and H. Lundell. "Validation strategies for the interpretation of microstructure imaging using diffusion MRI". *NeuroImage*. Microstructural Imaging 182 (Nov. 2018), pp. 62–79. DOI: 10.1016/j.neuroimage.2018.06.049.

[170] A. Yendiki, M. Aggarwal, M. Axer, A. F. D. Howard, A.-M. v. C. van Walsum, and S. N. Haber. "Post mortem mapping of connectional anatomy for the validation of diffusion MRI". *NeuroImage* 256 (Aug. 2022), p. 119146. DOI: 10.1016/j.neuroimage.2022.119146.

[171] A. Horowitz, D. Barazany, I. Tavor, G. Yovel, and Y. Assaf. "Response to the comments on the paper by Horowitz et al. (2014)". *Brain Structure and Function* 220.3 (May 2015), pp. 1791–1792. DOI: 10.1007/s00429-015-1031-x.

[172] C. M. W. Tax, F. Szczepankiewicz, M. Nilsson, and D. K. Jones. "The dot-compartment revealed? Diffusion MRI with ultra-strong gradients and spherical tensor encoding in the living human brain". *NeuroImage* 210 (Apr. 2020), p. 116534. DOI: 10.1016/j.neuroimage.2020.116534.

[173] L. Leenen, J. Meek, and R. Nieuwenhuys. "Unmyelinated fibers in the pyramidal tract of the rat: a new view". *Brain Research* 246.2 (Aug. 1982), pp. 297–301. DOI: 10.1016/0006-8993(82)91179-9.

[174] T. M. Shepherd, P. E. Thelwall, G. J. Stanisz, and S. J. Blackband. "Aldehyde fixative solutions alter the water relaxation and diffusion properties of nervous tissue". *Magnetic Resonance in Medicine* 62.1 (2009), pp. 26–34. DOI: 10.1002/mrm.21977.

[175] A. C. Seifert, M. Umphlett, M. Hefti, M. Fowkes, and J. Xu. "Formalin tissue fixation biases myelin-sensitive MRI". *Magnetic Resonance in Medicine* 82.4 (2019), pp. 1504–1517. DOI: 10.1002/mrm.27821.

[176] Veraart, Jelle, Raven, Erika P., Jones, Derek K., and Palombo, Marco. "Axon diameter mapping is confounded by glial cells". *Proceedings of the Annual Meeting of the International Society for Magnetic Resonance in Medicine.* June 2023.

[177] S. Y. Huang, S. M. Tobyne, A. Nummenmaa, T. Witzel, L. L. Wald, J. A. McNab, and E. C. Klawiter. "Characterization of Axonal Disease in Patients with Multiple Sclerosis Using High-Gradient-Diffusion MR Imaging". *Radiology* 280.1 (July 2016), pp. 244–251. DOI: 10.1148/radiol.2016151582.

[178] S. Y. Huang, Q. Fan, N. Machado, A. Eloyan, J. D. Bireley, A. W. Russo, S. M. Tobyne, K. R. Patel, K. Brewer, S. F. Rapaport, A. Nummenmaa, T. Witzel, J. C. Sherman, L. L. Wald, and E. C. Klawiter. "Corpus callosum axon diameter relates to cognitive impairment in multiple sclerosis". *Annals of Clinical and Translational Neurology* 6.5 (May 2019), pp. 882–892. DOI: 10.1002/acn3.760.

[179] R. M. Stassart, W. Möbius, K.-A. Nave, and J. M. Edgar. "The Axon-Myelin Unit in Development and Degenerative Disease". *Frontiers in Neuroscience* 12 (2018), p. 467. DOI: 10.3389/fnins.2018.00467.

[180] G. Bartzokis. "Alzheimer's disease as homeostatic responses to age-related myelin breakdown". *Neurobiology of Aging* 32.8 (Aug. 2011), pp. 1341–1371. DOI: 10.1016/j.neurobiolaging.2009.08.007.

[181] I. Drobnjak, B. Siow, and D. C. Alexander. "Optimizing gradient waveforms for microstructure sensitivity in diffusion-weighted MR". *Journal of Magnetic Resonance* 206.1 (Sept. 2010), pp. 41–51. DOI: 10.1016/j.jmr.2010.05.017.

[182] D. C. Alexander. "A general framework for experiment design in diffusion MRI and its application in measuring direct tissue-microstructure features". *Magnetic Resonance in Medicine* 60.2 (2008), pp. 439–448. DOI: 10.1002/mrm.21646.

[183] L. S. Kakkar, O. F. Bennett, B. Siow, S. Richardson, A. Ianuş, T. Quick, D. Atkinson, J. B. Phillips, and I. Drobnjak. "Low frequency oscillating gradient spin-echo sequences improve sensitivity to axon diameter: An experimental study in viable nerve tissue". *NeuroImage* 182 (Nov. 2018), pp. 314–328. DOI: 10.1016/j.neuroimage.2017.07.060.

[184] T. Niendorf, A. Pohlmann, H. M. Reimann, H. Waiczies, E. Peper, T. Huelnhagen, E. Seeliger, A. Schreiber, R. Kettritz, K. Strobel, M.-C. Ku, and S. Waiczies. "Advancing Cardiovascular, Neurovascular, and Renal Magnetic Resonance Imaging in Small Rodents Using Cryogenic Radiofrequency Coil Technology". *Frontiers in Pharmacology* 6 (2015), p. 255. DOI: 10.3389/fphar.2015.00255.

[185] D. A. Feinberg, A. J. S. Beckett, A. T. Vu, J. Stockmann, L. Huber, S. Ma, S. Ahn, K. Setsompop, X. Cao, S. Park, C. Liu, L. L. Wald, J. R. Polimeni, A. Mareyam, B. Gruber, R. Stirnberg, C. Liao, E. Yacoub, M. Davids, P. Bell, E. Rummert, M. Koehler, A. Potthast, I. Gonzalez-Insua, S. Stocker, S. Gunamony, and P. Dietz. "Next-generation MRI scanner designed for ultra-high-resolution human brain imaging at 7 Tesla". *Nature Methods* 20.12 (Dec. 2023), pp. 2048–2057. DOI: 10.1038/s41592-023-02068-7.

[186] J. Veraart, D. S. Novikov, D. Christiaens, B. Ades-Aron, J. Sijbers, and E. Fieremans. "Denoising of diffusion MRI using random matrix theory". *NeuroImage* 142 (Nov. 2016), pp. 394–406. DOI: 10.1016/j.neuroimage.2016.08.016.

[187] L. Cordero-Grande, D. Christiaens, J. Hutter, A. N. Price, and J. V. Hajnal. "Complex diffusion-weighted image estimation via matrix recovery under general noise models". *NeuroImage* 200 (Oct. 2019), pp. 391–404. DOI: 10.1016/j.neuroimage.2019.06.039.

[188] The GNU Development Team. *GNU Image Manipulation Program (GIMP)*. 2021. URL: https://gimp.org/ (visited on 08/25/2021).

[189] P. A. Yushkevich, J. Piven, H. C. Hazlett, R. G. Smith, S. Ho, J. C. Gee, and G. Gerig. "User-guided 3D active contour segmentation of anatomical structures: Significantly improved efficiency and reliability". *NeuroImage* 31.3 (July 2006), pp. 1116–1128. DOI: 10.1016/j.neuroimage.2006.01.015.

[190] P. Iakubovskii. *Segmentation Models Pytorch*. 2019. URL: https://github.com/qubvel/segmentation_models.pytorch (visited on 05/10/2021).

[191] M. Tan and Q. Le. "EfficientNet: Rethinking Model Scaling for Convolutional Neural Networks". *Proceedings of the 36th International Conference on Machine Learning*. ISSN: 2640-3498. PMLR, May 2019, pp. 6105–6114.

[192] J. Deng, W. Dong, R. Socher, L. Li, Kai Li, and Li Fei-Fei. "ImageNet: A large-scale hierarchical image database". *2009 IEEE Conference on Computer Vision and Pattern Recognition*. ISSN: 1063-6919. June 2009, pp. 248–255. DOI: 10.1109/CVPR.2009.5206848.

[193] A. G. Roy, N. Navab, and C. Wachinger. "Concurrent Spatial and Channel 'Squeeze & Excitation' in Fully Convolutional Networks". *Medical Image Computing and Computer Assisted Intervention – MICCAI 2018*. Ed. by A. F. Frangi, J. A. Schnabel, C. Davatzikos, C. Alberola-López, and G. Fichtinger. Lecture Notes in Computer Science. Cham: Springer International Publishing,

2018, pp. 421–429. ISBN: 978-3-030-00928-1. DOI: 10.1007/978-3-030-00928-1_48.

[194] A. B. Jung, K. Wada, J. Crall, S. Tanaka, J. Graving, C. Reinders, S. Yadav, J. Banerjee, G. Vecsei, A. Kraft, Z. Rui, J. Borovec, C. Vallentin, S. Zhydenko, K. Pfeiffer, B. Cook, I. Fernández, F.-M. De Rainville, C.-H. Weng, A. Ayala-Acevedo, R. Meudec, M. Laporte, et al. *imgaug*. 2020. URL: https://github.com/aleju/imgaug (visited on 08/25/2021).

[195] M. Macenko, M. Niethammer, J. S. Marron, D. Borland, J. T. Woosley, Xiaojun Guan, C. Schmitt, and N. E. Thomas. "A method for normalizing histology slides for quantitative analysis". *2009 IEEE International Symposium on Biomedical Imaging: From Nano to Macro*. Boston, MA, USA: IEEE, June 2009, pp. 1107–1110. ISBN: 978-1-4244-3931-7. DOI: 10.1109/ISBI.2009.5193250.

[196] P. Byfield. *StainTools*. 2018. URL: https://github.com/Peter554/StainTools (visited on 06/18/2020).

[197] T. Akiba, S. Sano, T. Yanase, T. Ohta, and M. Koyama. "Optuna: A Next-generation Hyperparameter Optimization Framework". *Proceedings of the 25th ACM SIGKDD International Conference on Knowledge Discovery & Data Mining*. KDD '19. New York, NY, USA: Association for Computing Machinery, July 2019, pp. 2623–2631. ISBN: 978-1-4503-6201-6. DOI: 10.1145/3292500.3330701.

[198] M. Berman, A. R. Triki, and M. B. Blaschko. "The Lovasz-Softmax Loss: A Tractable Surrogate for the Optimization of the Intersection-Over-Union Measure in Neural Networks". *2018 IEEE/CVF Conference on Computer Vision and Pattern Recognition*. ISSN: 2575-7075. June 2018, pp. 4413–4421. DOI: 10.1109/CVPR.2018.00464.

[199] W. A. e. a. Falcon and et al. *PyTorch Lightning*. original-date: 2019-03-31T00:45:57Z. 2019. URL: https://github.com/PyTorchLightning/pytorch-lightning (visited on 05/10/2021).

[200] A. Paszke, S. Gross, F. Massa, A. Lerer, J. Bradbury, G. Chanan, T. Killeen, Z. Lin, N. Gimelshein, L. Antiga, A. Desmaison, A. Köpf, E. Yang, Z. DeVito, M. Raison, A. Tejani, S. Chilamkurthy, B. Steiner, L. Fang, J. Bai, and S. Chintala. "PyTorch: an imperative style, high-performance deep learning library". *Proceedings of the 33rd International Conference on Neural Information Processing Systems*. 721. Red Hook, NY, USA: Curran Associates Inc., Dec. 2019, pp. 8026–8037.

[201] F. A. Breuer, M. Blaimer, R. M. Heidemann, M. F. Mueller, M. A. Griswold, and P. M. Jakob. "Controlled aliasing in parallel imaging results in higher acceleration (CAIPIRINHA) for multi-slice imaging". *Magnetic Resonance in Medicine* 53.3 (Mar. 2005), pp. 684–691. DOI: 10.1002/mrm.20401.

[202] M. A. Griswold, P. M. Jakob, R. M. Heidemann, M. Nittka, V. Jellus, J. Wang, B. Kiefer, and A. Haase. "Generalized autocalibrating partially parallel acquisitions (GRAPPA)". *Magnetic Resonance in Medicine* 47.6 (June 2002), pp. 1202–1210. DOI: 10.1002/mrm.10171.

[203] K. Setsompop, J. Cohen-Adad, B. A. Gagoski, T. Raij, A. Yendiki, B. Keil, V. J. Wedeen, and L. L. Wald. "Improving diffusion MRI using simultaneous multi-slice echo planar imaging". *NeuroImage* 63.1 (Oct. 2012), pp. 569–580. DOI: 10.1016/j.neuroimage.2012.06.033.

[204] D. K. Jones, M. A. Horsfield, and A. Simmons. "Optimal strategies for measuring diffusion in anisotropic systems by magnetic resonance imaging". *Magnetic Resonance in Medicine* 42.3 (Sept. 1999), pp. 515–525.

[205] M. Brant-Zawadzki, G. D. Gillan, and W. R. Nitz. "MP RAGE: a three-dimensional, T1-weighted, gradient-echo sequence–initial experience in the brain." *Radiology* 182.3 (Mar. 1992). Publisher: Radiological Society of North America, pp. 769–775. DOI: 10.1148/radiology.182.3.1535892.

[206] J.-D. Tournier, R. Smith, D. Raffelt, R. Tabbara, T. Dhollander, M. Pietsch, D. Christiaens, B. Jeurissen, C.-H. Yeh, and A. Connelly. "MRtrix3: A fast, flexible and open software framework for medical image processing and visualisation". *NeuroImage* 202 (Nov. 2019), p. 116137. DOI: 10.1016/j.neuroimage.2019.116137.

[207] J. L. R. Andersson and S. N. Sotiropoulos. "An integrated approach to correction for off-resonance effects and subject movement in diffusion MR imaging". *NeuroImage* 125 (Jan. 2016), pp. 1063–1078. DOI: 10.1016/j.neuroimage.2015.10.019.

[208] P. J. Basser, J. Mattiello, and D. LeBihan. "Estimation of the effective self-diffusion tensor from the NMR spin echo". *Journal of Magnetic Resonance. Series B* 103.3 (Mar. 1994), pp. 247–254. DOI: 10.1006/jmrb.1994.1037.

[209] S. Coelho, S. H. Baete, G. Lemberskiy, B. Ades-Aron, G. Barrol, J. Veraart, D. S. Novikov, and E. Fieremans. "Reproducibility of the Standard Model of diffusion in white matter on clinical MRI systems". *NeuroImage* 257 (Aug. 2022), p. 119290. DOI: 10.1016/j.neuroimage.2022.119290.

[210] S. Coelho, J. Veraart, E. Fieremans, and D. S. Novikov. *NYU-DiffusionMRI/SMI*. original-date: 2020-02-26T19:15:26Z. Dec. 2023. URL: https://github.com/NYU-DiffusionMRI/SMI (visited on 02/11/2024).

[211] H. Zhang, T. Schneider, Wheeler-Kingshott, and D. C. Alexander. *NODDI Matlab Toolbox*. 2012. URL: http://mig.cs.ucl.ac.uk/index.php?n=Tutorial.NODDImatlab (visited on 02/11/2024).

[212] K. L. West, N. D. Kelm, R. P. Carson, D. C. Alexander, D. F. Gochberg, and M. D. Does. "Experimental studies of g-ratio MRI in ex vivo mouse brain". *NeuroImage* 167 (Feb. 2018), pp. 366–371. DOI: 10.1016/j.neuroimage.2017.11.064.

[213] Y. Assaf, R. Z. Freidlin, G. K. Rohde, and P. J. Basser. "New modeling and experimental framework to characterize hindered and restricted water diffusion in brain white matter". *Magnetic Resonance in Medicine* 52.5 (2004), pp. 965–978. DOI: 10.1002/mrm.20274.

[214] I. Drobnjak, H. Zhang, M. G. Hall, and D. C. Alexander. "The matrix formalism for generalised gradients with time-varying orientation in diffusion NMR". *Journal of Magnetic Resonance* 210.1 (May 2011), pp. 151–157. DOI: 10.1016/j.jmr.2011.02.022.

[215] A. Ianuş, D. C. Alexander, and I. Drobnjak. "Microstructure Imaging Sequence Simulation Toolbox". *Simulation and Synthesis in Medical Imaging*. Ed. by S. A. Tsaftaris, A. Gooya, A. F. Frangi, and J. L. Prince. Cham: Springer International Publishing, 2016, pp. 34–44. ISBN: 978-3-319-46630-9. DOI: 10.1007/978-3-319-46630-9_4.

[216] P. T. Callaghan. "A Simple Matrix Formalism for Spin Echo Analysis of Restricted Diffusion under Generalized Gradient Waveforms". *Journal of Magnetic Resonance* 129.1 (Nov. 1997), pp. 74–84. DOI: 10.1006/jmre.1997.1233.

[217] G. Watson. "Equatorial distributions on a sphere". *Biometrika* 52.1-2 (June 1965), pp. 193–202. DOI: 10.1093/biomet/52.1-2.193.

[218] V. I. Lebedev and D. N. Laikov. "A quadrature formula for the sphere of the 131st algebraic order of accuracy". *Doklady Mathematics* 59.3 (1999), pp. 477–481.

[219] R. Parrish. *getLebedevSphere*. Feb. 2024. URL: https://de.mathworks.com/matlabcentral/fileexchange/27097-getlebedevsphere (visited on 02/11/2024).

[220] C. Birkl, C. Langkammer, J. Haybaeck, C. Ernst, R. Stollberger, F. Fazekas, and S. Ropele. "Temperature-induced changes of magnetic resonance relaxation times in the human brain: A postmortem study". *Magnetic Resonance in Medicine* 71.4 (2014), pp. 1575–1580. DOI: 10.1002/mrm.24799.

[221] S. Murali-Manohar, T. Borbath, A. M. Wright, B. Soher, R. Mekle, and A. Henning. "T2 relaxation times of macromolecules and metabolites in the human brain at 9.4 T". *Magnetic Resonance in Medicine* 84.2 (2020), pp. 542–558. DOI: 10.1002/mrm.28174.

[222] S. M. Smith, M. Jenkinson, M. W. Woolrich, C. F. Beckmann, T. E. J. Behrens, H. Johansen-Berg, P. R. Bannister, M. De Luca, I. Drobnjak, D. E. Flitney, R. K. Niazy, J. Saunders, J. Vickers, Y. Zhang, N. De Stefano, J. M. Brady, and P. M. Matthews. "Advances in functional and structural MR image analysis and implementation as FSL". *NeuroImage* 23 Suppl 1 (2004), S208–219. DOI: 10.1016/j.neuroimage.2004.07.051.

[223] S. Mori, K. Oishi, H. Jiang, L. Jiang, X. Li, K. Akhter, K. Hua, A. V. Faria, A. Mahmood, R. Woods, A. W. Toga, G. B. Pike, P. R. Neto, A. Evans, J. Zhang, H. Huang, M. I. Miller, P. van Zijl, and J. Mazziotta. "Stereotaxic white matter atlas based on diffusion tensor imaging in an ICBM template". *NeuroImage* 40.2 (Apr. 2008), pp. 570–582. DOI: 10.1016/j.neuroimage.2007.12.035.

[224] J. E. Lee, M. K. Chung, M. Lazar, M. B. DuBray, J. Kim, E. D. Bigler, J. E. Lainhart, and A. L. Alexander. "A Study of Diffusion Tensor Imaging by Tissue-Specific, Smoothing-Compensated Voxel-Based Analysis". *NeuroImage* 44.3 (Feb. 2009), pp. 870–883. DOI: 10.1016/j.neuroimage.2008.09.041.

[225] A. H. Andersen. "On the Rician distribution of noisy MRI data". *Magnetic Resonance in Medicine* 36.2 (1996), pp. 331–332. DOI: 10.1002/mrm.1910360222.

List of figures

List of tables

List of symbols

$\mathbf{B}$	total magnetic field 24
B_0	static magnetic field strength 24
$\mathbf{B}_0$	static magnetic field 23
$\mathbf{B}_1$	oscillating magnetic field 24
b	diffusion weighting 28
D	diffusion coefficient 26
$\mathbf{D}$	diffusion tensor 32
D_0	axoplasmic diffusivity 36
$D_\mathrm{a}^\parallel$	intra-axonal parallel diffusivity 34
$D_\mathrm{a}^\perp$	intra-axonal perpendicular diffusivity 34
$D_\mathrm{e}^\parallel$	extra-axonal parallel diffusivity 34
$D_\mathrm{e}^\perp$	extra-axonal perpendicular diffusivity 34
Δ	diffusion gradient separation 28
δ	diffusion gradient duration 28
f_0	intra-axonal water fraction 99
f_a	T_2-weighted intra-axonal signal fraction 34
f_e	T_2-weighted extra-axonal signal fraction 34
f_im	immobile water fraction 38
ϕ	spin phase 27
$\mathbf{G}$	diffusion gradient 27
g	diffusion gradient amplitude 28
$\mathbf{g}$	diffusion gradient direction (normalized) 32
g_max	maximum diffusion gradient amplitude 29
γ	gyromagnetic ratio 24
H	axon radius distribution 36
$\mathbf{M}$	net magnetization 25
M_0	static magnetization magnitude 24
$\mathbf{M}_0$	static magnetization 24

$\mathbf{n}$	fiber orientation 34
$\bar{\mathbf{n}}$	main fiber orientation 95
ω_0	Larmor frequency 24
P	diffusion propagator 26
p	statistical significance 106
Ψ	fiber orientation distribution function 34, 98
R	Pearson's correlation coefficient 106
r	axon radius 22
r_{arith}	arithmetic mean axon radius 37
r_{eff}	effective axon radius 37
S	diffusion-weighted signal 27
S_0	non-diffusion-weighted signal 27
S_{a}	intra-axonal signal 34
S_{e}	extra-axonal signal 34
σ	noise level 30
T_1	longitudinal relaxation time 25
T_2	transverse relaxation time 25
TE	echo time 28
TR	repetition time 29

List of acronyms

2D two-dimensional 12

3D three-dimensional 17

ADC apparent diffusion coefficient 32

ASD autism spectrum disorder 7

CNN convolutional neural network 17

CoV coefficient of variation 101

CSF cerebrospinal fluid 11

DKI diffusion kurtosis imaging 33

dMRI diffusion-weighted magnetic resonance imaging 26

DTI diffusion tensor imaging 32

EM electron microscopy 13

EPI echo planar imaging 30

FA fractional anisotropy 32

FNN feedforward neural network 15

FSR fitting success rate 105

GPA Gaussian phase approximation 27

LM light microscopy 13

MD mean diffusivity 32

ML maximum likelihood 68

MRI magnetic resonance imaging 23

NMBE normalized mean bias error 101

NMR nuclear magnetic resonance 23

NRMSE normalized root-mean-square error 105

ODF orientation distribution function 34

PGSE pulsed gradient spin echo 28

ReLU rectified linear unit 16

RF radiofrequency 24

ROI region of interest 8

scSE spatial channel squeeze-and-excitation 92

SGD stochastic gradient descent 21

SNR signal-to-noise ratio 29

TEM transmission electron microscopy 13

WPA wide pulse approximation 36